Unione Europea

Ministero dell'Istruzione, dell'Università e della Ricerca

UNIVERSITÀ DEGLI STUDI DI SALERNO

FONDO SOCIALE EUROPEO

Programma Operativo Nazionale 2000/2006
"Ricerca Scientifica, Sviluppo Tecnologico, Alta Formazione"
Regioni dell'Obiettivo 1 – Misura III.4
"Formazione superiore ed universitaria"

Department of Industrial Engineering

Ph.D. Course in Chemical Engineering
(XVI Cycle-New Series, XXX Cycle)

Growth and characterization of epitaxial oxide-based electron and hole-doped thin films and their heterostructures

Supervisor
Prof. Luigi Maritato

Ph.D. student
Chiara Sacco

Ph.D. Course Coordinator
Prof. Ernesto Reverchon

Acknowledgements

There are several people that I am grateful for contributing to the realization of this work.

Firstly, I would like to express my sincere gratitude to my supervisor Prof. Luigi Maritato for the continuous support during my Ph.D. experience, for trusting me, for his patience, motivation, knowledge and competence. His guidance has been fundamental for giving me always the right advices and tips.

I am grateful to Prof. Darrell G. Schlom for hosting me in his lab at Cornell University for a year. He has been willing to help me when I had some trouble and doubt during my experiments. Without his precious support it would not be possible to conduct this research.

My sincere thanks also goes to Dr. Alice Galdi, who taught me firstly "how to put my hands" on the lab facilities. She constantly has followed my experience with patience and competence.

There have been many people that have contributed to this work: I would to thank Dr. Pasquale Orgiani for being always present from Trieste and for the frequent discussions about the data; Miss Nunzia Coppola for being always available to help me when I needed it; Dr. Francesco Romeo for his theoretical support; Mr. Luigi Falco for intervening when technical problems occurred not only on the MBE; Mr. Haofei Wei for the shared lab time at Cornell University to grow better samples; all the Cornell lab-mates that gave me the technical and scientific support in order to "communicate" properly with the MBE at Cornell University.

I have to thank my family and Alessandro that always believed in me and always encouraged me step-by-step, in particular when I went "on the other side of the Ocean" for the first time and for a whole year.

Finally, I thank myself for never giving up neither in the hardest moments.

List of publications

- "X-ray Absorption Spectroscopy study of annealing process on $Sr_{1-x}La_xCuO_2$ electron doped cuprate thin films", A. Galdi, P. Orgiani, C. Sacco, B. Gobaut, P. Torelli, C. Aruta, N. B. Brookes, M. Minola, J. W. Harter, K. M. Shen, D. G. Schlom, L. Maritato, *Journal of Applied Physics*, vol. 123, issue 12 (2018)
  DOI: https://doi.org/10.1063/1.5021559

- "Growth and characterization of charge carrier spatially confined SrMnO3/La0.7Sr0.3MnO3/SrMnO3 trilayers", A. Galdi, C. Sacco, P. Orgiani, F. Romeo, L. Maritato, *Journal of Crystal Growth*, vol. 459, pp 56-60 (2017)
  DOI: https://doi.org/10.1016/j.jcrysgro.2016.11.024

- "Structural and electronic properties of Bi2Se3 topological insulator thin films grown by pulsed laser deposition", P. Orgiani, C. Bigi, P. Kumar Das, J. Fujii, R. Ciancio, B. Gobaut, A. Galdi, C. Sacco, L. Maritato, P. Torelli, G. Panaccione, I. Vobornik, G. Rossi, *Applied Physics Letters*, vol. 110, issue 17 (2017)
  DOI: https://doi.org/10.1063/1.4982207

- "Noise Spectroscopy Investigation of Interplay Between Quantum Interference Effects and Superconductivity in Infinite Layer Cuprates", C. Barone, A. Galdi, C. Sacco, P. Orgiani, D. G. Schlom, S. Pagano, L. Maritato, *IEEE Transactions on Applied Superconductivity*, vol. 26, issue 3 (2016)
  DOI: 10.1109/TASC.2016.2540243

- "The Role of Quantum Interference Effects in Normal-State Transport Properties of Electron-Doped Cuprates", P. Orgiani, A. Galdi, C. Sacco, S. Charpentier, F. Lombardi, C. Barone, S. Pagano,

D. G. Schlom, L. Maritato, *Journal of Superconductivity and Novel Magnetism*, vol. 28, issue 12, pp 3481-3486 (2015)
DOI: https://doi.org/10.1007/s10948-015-3209-0

Publication list submitted/to be submitted:

- "Layering induced dimensional effects on the normal and superconductive state of electron-doped cuprates", C. Sacco, A. Galdi, F. Romeo, N. Coppola, P. Orgiani, H. I. Wei, K. Shen, D. G. Schlom, L. Maritato, *submitted*

- "Charge ordering with 8 unit cell periodicity in the electron-doped infnite-layer cuprate $Sr_{1-x}La_xCuO_2$", H. I. Wei, C. Sacco, C. McMahon, A. Galdi, J. P. Ruf, T. Shi, C. Suen, C. Adamo, J. W. Harter, R. Sutaro, F. He, L. Maritato, D. G. Schlom, D. G. Hawthorn, K. M. Shen, *to be submitted*

- "Low temperature hidden Fermi-liquid charge transport in $Sr_{1-x}La_xCuO_2$ infinite layer electron-doped thin films", C. Sacco, A. Galdi, P. Orgiani, R. Arpaia, S. Charpentier, F. Lombardi, H. Wei, K. M. Shen, D. G. Schlom, L. Maritato, *to be submitted*

Contents

List of figures

List of tables

Abstract

The main goal of this dissertation is the study of the effects induced by quantum confinement in transition-metal oxides quantum wells (QWs). The field of possible applications of oxide-based heterostructures (oxide-based nanoelectronics, spintronics, quantum computation, excitonic devices, energy conversion in solar cells, etc.) is very ample and growing, thanks to the many fascinating and exotic properties of transition-metal oxides and their versatility as well.

p-type $SrMnO_3/La_{0.7}Sr_{0.3}MnO_3/SrMnO_3$ QWs and *n*-type $SrCuO_2/Sr_{0.9}La_{0.1}CuO_2/SrCuO_2$ QWs have been studied.

The first part of my work has been devoted to the investigation of quantum confinement achievement using a Mott insulator with a small band gap. The observed results suggest that this type of material can be successfully used in QWs.

As a final result of my work, the achievement of dimensional effects induced by the layering on the normal state of both investigated systems (*n* and *p*-doped) has been assessed. In addition, the layering has been shown to influence the superconducting state of the investigated *n*-doped QWs and on the metal-to-insulator transition of the *p*-doped QWs.

The investigation of the behavior of each layer constituent the QW (both *n* and *p*-doped) is relevant in view of future growth of proximate *p*-*n* doped systems. Part of my work, therefore, has been devoted to the study of the properties of $(Sr,La)CuO_2$ thin films.

The study of electrical transport properties of SLCO thin films as a function of the doping has allowed to relate the presence of the low temperature upturn in the $(Sr,La)CuO_2$ resistivity versus temperature curves the quantum interference effects produced by weak localization effects. Furthermore, the presence of low temperature Fermi liquid behaviors in SLCO thin films has also been observed.

The last part of my work has dealt with the effects of the *in-situ* annealing step on the final superconductivity properties of the (Sr,La)CuO_2 films, helping to optimize the growth step, crucial for the quality of this thin film and, consequently, of the *n*-doped QWs based on this compound. The effect of annealing, i.e. of the O content, has been studied, by using X-ray Absorption Spectroscopy (XAS) measurements performed at the Elettra Synchrotron in Trieste, Italy, and has allowed to reveal clear signature of apical Oxygen removal.

Introduction

During this Ph.D. work, I have investigated the effects induced by quantum confinement in transition-metal oxides (TMO) low-dimensional systems and hetero-structures, such as quantum wells (QWs). An oxide-based QW is the simplest system in which a quantum confinement can be obtained, consisting in a thin layer of one oxide material, sandwiched between two layers of another oxide insulating material (this creates a well in which the carriers can move in two directions but are confined in the third). In these systems it is possible to create and manipulate quantum states of matter, including novel superconductors, high Curie-temperature magnets, controllable metal-insulator transition.

The oxide-based QWs recently raised interest compared to the well-known semiconductors based ones thanks to the possibility to obtain lower dimensional heterostructures (a few nm), higher sheet carrier density (10^{14} cm^{-2}), one order of magnitude more than the highest density achievable in conventional semiconductors III-nitrides, and many fascinating and exotic behaviors related to the spectacular versatility of the complex oxide interfaces (Stemmer and Millis, (2013)).

The field of possible applications of oxide-based heterostructures (oxide-based nanoelectronics, spintronics, quantum computation, excitonic devices, energy conversion in solar cells, etc.) is very ample and growing, as it will be described in Section I.3, thanks to the many fascinating and exotic properties of TMO and their versatility as well.

The study of oxide-based QWs, and of TMO thin films in general, is possible thanks to the important developments in oxide thin films depositions techniques and in particular in oxide-molecular beam epitaxy (O-MBE) techniques, where atomic-scale thickness control, abrupt interfaces and the possibility to change the chemical composition over a distance of a

single unit cell, are now achievable (Biegalski et al., (2008); Jalan et al., (2009); Petrov et al., (2004); Schlom et al., (2001)).

Many TMO are Mott insulators (Mott insulators are a class of materials that should conduct electricity under conventional band theories, but experimentally they are insulators. This effect is due to electron–electron interactions, which are not considered in conventional band theory), with small energy band gaps, and the question arises on the ability to obtain quantum confinement by using them as insulating materials in QWs.

The first part of my work has been dedicated to answer this question: *p*-type $SrMnO_3/La_{0.7}Sr_{0.3}MnO_3/SrMnO_3$ (SMO/LSMO/SMO) QWs have been grown at University of Salerno by O-MBE deposition techniques and their electrical transport properties have been characterized as a function of the temperature and of the relative thicknesses (Galdi et al., (2017)). The observed results have indicated the presence of spatial charge carrier confinement in the investigated trilayers pointing out the ability of a small gap Mott insulator material, such as SMO, with an energy gap of 0.35 eV (Søndenå et al., (2006)), to be successfully used in QWs.

The following part of my work has been devoted to the study of both the *p* and *n*-type oxide-based QWs, which is important because it could open the way to investigate carrier symmetries in such systems and to obtain hybrid *p*-*n* proximate structures with the presence of long life-time excitons (hole-electron couples). The availability of both *p* and *n* doped oxide QWs to be grown by the same deposition technique in similar deposition processes, involving a minimum number of materials, is central to obtain *p*-*n* TMO based proximate structures (Kim et al., (2016); Millis and Schlom, (2010)).

The electron-doped structures I focused my attention are the *n*-type $SrCuO_2/Sr_{0.9}La_{0.1}CuO_2/SrCuO_2$ (SCO/SLCO/SCO) QWs, which I have grown during my abroad experience at Cornell University, Ithaca, NY-USA.

The fabrication of low dimensional systems with high superconductive critical temperature (T_C), such as electron-doped infinite-layers SLCO, confined to nanometer-sized interfaces, is an intriguing issue by itself, due to the possibility to study a paradigmatic quantum phenomenon, such as superconductivity in reduced dimensionality, and to exploit its potential application (Ahn et al., (2003), (1999); Gozar et al., (2008); Mannhart and Schlom, (2010)).

As a final result of my work, the achievement of dimensional effects induced by the layering on the normal state of both investigated systems (*n* and *p*-doped) has been assessed. In addition, the layering has been shown to

influence the superconducting state of the investigated *n*-doped QWs and on the metal-to-insulator transition of the *p*-doped QWs.

The growth and characterization of QWs implies the preventive study of the behavior of the metallic single layers (LSMO for the *p*-doped QWs and SLCO for the *n*-doped QWs).

Such investigations are relevant especially in view of the future growth of proximate *p*-*n* doped DQWs. In fact, one of the advantages to use TMO-based QWs rely on the possible tuning of the density of carriers changing the doping level of the central layer. This will offer two controlled knots (i.e. the central layer thickness and its doping) to tune the interaction among electrons and holes improving the final versatility of the applicative device.

This part of my work, with the further investigation of the normal state transport properties of SLCO thin films, has pointed out new interesting behaviors. In particular, despite the considerable efforts of the scientific community, a conclusive understanding of the normal-state transport properties of electron-doped cuprates is still missing and the results obtained in this work on SLCO thin films having the simplest crystal structures with CuO_2 planes that hosts high-T_C superconductivity, have clarified some aspects of this existing puzzling scenario.

In particular, the study of electrical transport properties of SLCO thin films as a function of the doping has allowed to relate the presence of the low temperature upturn in the SLCO resistivity versus temperature curves the quantum interference effects produced by weak localization effects (Barone et al., (2016); P Orgiani et al., (2015)). Furthermore, the presence of low temperature Fermi liquid behaviors in SLCO thin films have also been observed.

The last part of my work has dealt with the effects of the *in-situ* annealing step on the final superconductivity properties of the SLCO films. These are strongly affected by sample preparation conditions and a reduction process is needed for all electron doped cuprates thin films in order to get superconductivity.

The optimization of this step is, therefore, crucial for the quality of SLCO thin films and, consequently, of the *n*-doped QWs based on this compound. The effect of annealing, i.e. of the O content, has been studied, by using X-ray Absorption Spectroscopy (XAS) measurements performed at the Elettra Synchrotron in Trieste, Italy, and has allowed to reveal clear signature of apical Oxygen removal.

This dissertation is organized as following: in the Chapter I, I describe the quantum confinement in QWs and the importance of innovative material for

QWs (Section I.1). The most important results on oxide-based heterostructures already present in scientific literature are also highlighted (Section I.2). Section I.3 is dedicated to the potential application of oxide-based heterostructures. In Section I.4 the main properties of Mn and Cu oxide-based compounds are described in details, focusing on their crystal and electronic structure and on their respective phase diagrams as well.

In Chapter II, the experimental techniques are described: deposition techniques (Sections II.1), standard thin film characterization methods (i.e. XRD measurements for structural characterization and electrical transport measurements) (Section II.2) and advanced electron spectroscopic techniques (i.e. X-rays absorption spectroscopy both in presence and absence of magnetic field) (Section II.3).

Chapter III deals with the experimental results. In the first part I describe the results about the growth and characterization of *p*-type QWs (Section III.1). In particular, I describe the structural and electrical transport measurements as a function of the layer thicknesses, discussing the evidences of the quantum confinement (Sections III.1.1 and III.1.2). Furthermore, preliminary results about advanced spectroscopy measurements performed on *p*-type QWs are provided (Section III.1.3).

The deposition and characterization of *n*-type QWs is described in Section III.2. In particular, the structural and electrical transport characterizations done on these samples are described in Sections III.2.1 and III.2.2.

In the last Section, the doping effects on the normal and superconductive state of single layers SLCO thin films are analyzed (Section III.3), along with X-ray absorption spectroscopy measurements performed to study the effects of the annealing process (Section III.3.3).

Chapter I
Quantum confinement in Quantum Wells

I.1 Innovative materials for Quantum Wells

With the need of reducing dimensionality and, at the same time, of increasing the speed of conventional semiconductor-based micro and opto-electronic devices, scientific limitations are beginning to affect the newer device demands of modern times. Novel approaches involving new materials such as functional oxides are being explored for new concept of electronic devices. These innovative materials are interesting for new physics and novel functionalities arising from ultrathin oxide films and at oxide interfaces in their heterostructures, such as Quantum Wells (QWs). A QW is the simplest system in which a quantum confinement can be obtained and these systems are generally based on semiconductor science and technology. Quantum confinement involves the use of spatial modulation of chemical composition and electric fields to localize electrons to regions that are sufficiently small that their quantum mechanical properties are affected. An illustration of a semiconductor-based QW is shown in Figure I-1, where a thin semiconductor layer of lower band gap material (e.g. InGaN) is sandwiched between two thick semiconductor layers of larger band gap (e.g. GaN). This creates a potential well in which the carriers can move in two

directions but are confined in the third. These devices have replaced the conventional electronic components in QW lasers, QW detectors, QW modulators and so on (Odoh and Njapba, (2015)).

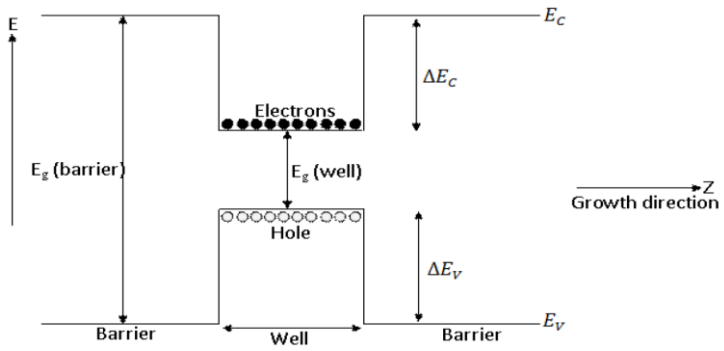

Figure I-1 *Schematic of a semiconductor-based QW as function of distance in the growth direction Z (Odoh and Njapba, (2015))*

The basic idea of a QW, as shown in Figure I-1, can be also realized with the transition metal oxides (TMOs) which offer a very rich physics: electrons in the narrow *d*-band of TMOs are subject to strong electron-electron interaction (correlated electrons) and this leads to a rich variety of physical phenomena that can be controlled, modified and tuned in an oxide-based QW (e.g. magnetism with high Curie temperature, metal-to-insulator transitions, high critical temperature superconductivity).

TMOs can be doped with electrons (*n*) or holes (*p*) as well as semiconductors, but these materials are good candidate to improve the performance of semiconductor-based devices. In fact, compared with semiconductor-based devices, it is possible to achieve very small devices (with dimensions of few nm), high electron densities required to obtain the Mott insulators are very high (on the order of 10^{22} cm^{-3}) and sheet carrier densities on the order of 10^{14} cm^{-2} in a single atomic plane are observable (Ahn et al., (2006)). Such sheet carrier densities are an order of magnitude higher than the highest density of two-dimensional gases (2DEGs) based on conventional semiconductors (III-nitrides) (Stemmer and Millis, (2013)).

The study of proximate *n-p* doped oxide-based structures to create and control electron-hole bound states, i.e. excitons, is a very intriguing topics in the physics of condensed matter. Excitons are relevant in many process and their possible manipulation can have important consequences in many

applications (for example, the energy conversion in solar cells) and even in the opening of completely new applicative field such as the excitonics (i.e. the electronics based on excitons).

Over the years, considerable effort has been invested in optically generated electron-hole liquids (Butov et al., (2002); Ideguchi et al., (2008)), but creating and manipulating sufficiently high-density while preventing the electron-hole recombination has proven challenging. In order to prevent fast recombination and to increase the exciton mean life as well, Zhu *et al.* proposed to construct a double quantum well (DQW) system in which one QW contains holes and the other contains electrons, as described in Section I.3.3. The spatial separation prevents recombination and it is possible to tune the interaction between electrons and holes by adjusting the distance between the two QWs (Littlewood and Zhu, (1996); Zhu et al., (1995)). The bound states in this way generated are known as indirect excitons.

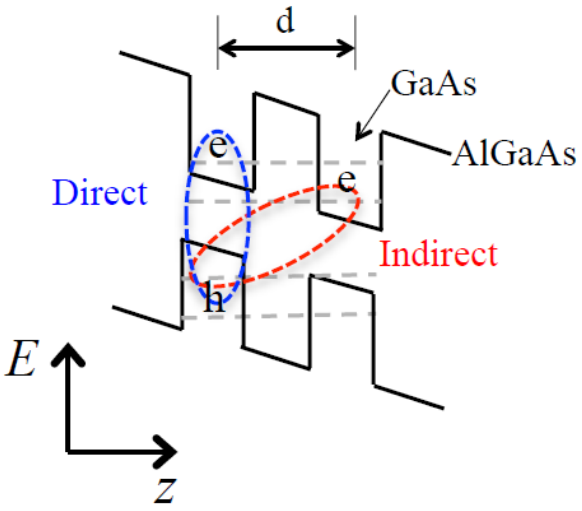

Figure I-2 *Direct and indirect excitons in semiconductor-based QW and DQW*

DQWs can be fabricated in semiconductor systems such as (Al,Ga)As, as shown in Figure I-2, but the large band gap of these materials requires a too large bias to effectively produce acceptable equilibrium in electron and hole populations (Millis and Schlom, (2010)). A.J. Millis and D. G. Schlom in 2010 proposed an interesting route to the formation of proximal electron and hole liquids, regarding an oxide heterostructure involving a thin layer of narrow gap correlated insulator, such as a Mott insulator (B in Figure I-3) ,

sandwiched between two different wide-band-gap insulator (A e C in Figure I-3). If AB and AC interfaces are polar and if charge reconstruction is absent (Okamoto and Millis, (2004)), an internal electric field can be generated, leading to a potential drop which scales linearly with the thickness of the correlated material (top panel in Figure I-3). The potential drop causes band bending which, if large enough, shifts the conduction band below the Fermi level on one side of the structure and the valence band above the Fermi level on the other side (bottom panel in Figure I-3), creating electron and hole accumulation respectively.

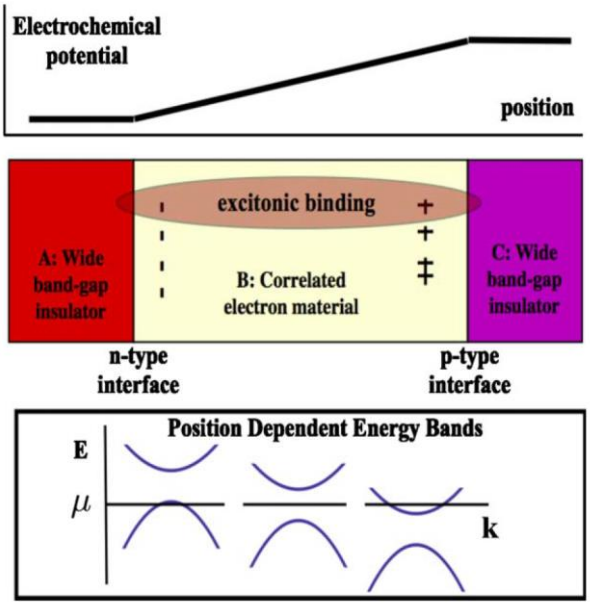

Figure I-3 *Sketch of heterostructure configuration in which a narrow- gap correlated insulator (B) is embedded in two wide band-gap insulators (A and C). The potential drop across the heterostructure is shown in top panel. The band bending presented ad energy E vs momentum k is shown in the bottom panel. μ is the chemical potential (Millis and Schlom, (2010))*

Mott insulators are particularly attractive candidates because of their properties. Indeed, they often have relatively small gaps 2Δ~0.3-2 eV (Imada et al., (1998)), so the electric field required to produce the needed band bending doesn't need to be prohibitively large. In addition, the physics of correlated materials is local, that is the relevant length scales for charge

phenomena are of the order of a unit cell while interlayer coupling are intrinsically weak (such as the parent compound of high superconductive critical temperature) or can be made weak inducing appropriately orbital ordering.

Several research groups have investigated the possibility of creating oxide-based QWs and DQWs. In the following Section, I will describe some of the most important results on this issue already present in scientific literature, where, in some systems, evidence of quantum confinement is observed. Nevertheless, a control of the properties related to the quantum confinement, as well as a control on the density of states, and consequently of the carriers, is not realized yet.

The QWs investigated in this work consist in a metallic layer known to be electron ($Sr_{0.9}La_{0.1}CuO_2$) or hole-doped ($La_{0.7}Sr_{0.3}MnO_3$) embedded in insulating materials, respectively $SrCuO_2$ and $SrMnO_3$. The peculiarities of these compounds will be described in detail in Section I.4.

The relevance of these systems is not only related to the study of their properties as a function of the relative thickness of each layer or to a future development of growing proximate *n-p* doped DQWs, but also to the possibility to tune the density of carrier changing the doping level of the central layer. In view of future devices development, the possibility to tune the interaction between the carriers thanks to the simple modulation of the layer thickness and of the carrier concentration (i.e. through the doping) is a key issues for the versatility of applications, as it will described in Section I.3.

I.2 Materials and examples of oxide-based QWs in literature

Experimentally, the scientific community has been concentrated largely on perovskite-structured TMO with the chemical formula ABO_3, where the B site ion is a transition metal with partially filled *d*-shell (or empty in case of $SrTiO_3$) and is octahedrally coordinated with six oxygen ions, while the A site ion is typically an alkali earth (e.g. Ca, Sr, Ba) or a trivalent rare-earth ion (e.g. La, Ce, Nd). The A site ion fills the *d*-shell donating two (for alkali earth) or three electrons (for lanthanides).

QWs studied until now have been created by spatial variation of electrochemical potential in several ways. One is by varying the A-site ion for example sandwiching a few layers of $LaMnO_3$ (LMO) between layers of

$SrMnO_3$ (SMO). In this way, the difference in charge between La^{3+} and Sr^{2+} ions create a spatially varying electrical potential causing a spatially varying electron density. Another choice is to vary the B-site ion, for example sandwiching a few layers of $SrVO_3$ between layers of $SrTiO_3$. In this example, the different electronegativities of V and Ti define the QW.

I.2.1 $SrTiO_3$/$SrVO_3$/$SrTiO_3$ QWs

QW consisting in *n* layers of $SrVO_3$, that is a conductive oxide and moderated correlated material with cubic perovskite structure, embedded in $SrTiO_3$, that is a cubic perovskite band insulator, have been studied by Yoshimatsu et al. using photoemission spectroscopy (Yoshimatsu et al., (2013), (2011), (2010)). Using this technique, it is possible to measure the occupied portion of electronic density of states. Yoshimatsu et al. observed that the photoemission spectra remain quite similar to that of bulk material down to approximately six unit cells of $SrVO_3$. Below this thickness, changes become apparent. Indeed, a suppression of the density of states peak at Fermi level is observable in Figure I-4 b). This behavior has been associated to quantum confinement effect. In particular, it has been observed that the quantum confinement can qualitatively alter the electronic properties but confinement effects become detectable only at very short length scale that, in this case, is less than six unit cell thickness.

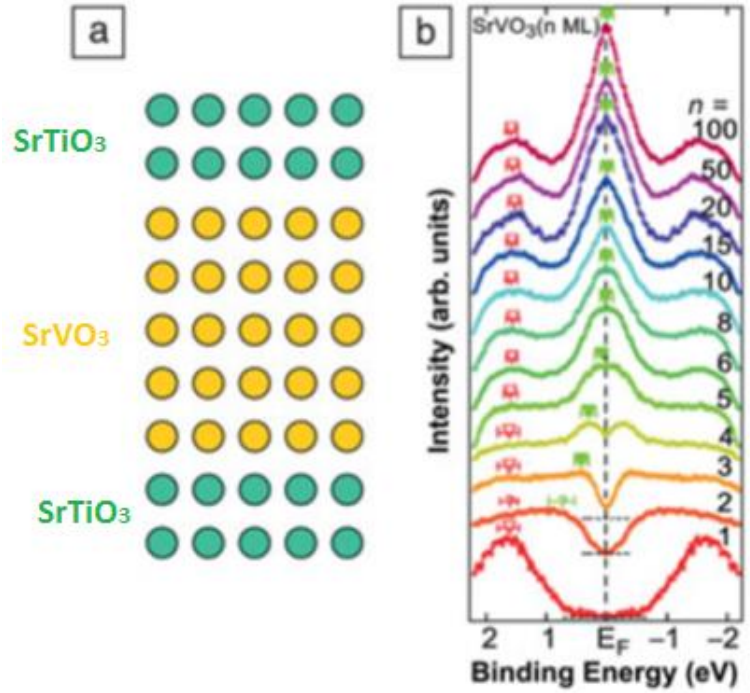

Figure I-4 *a) schematic of a QW with 5 SrVO3 layers embedded in SrTiO3; b) angle-integrated photoemission spectrum, symmetrized with respect to the Fermi energy in function of the number of the central layers (Yoshimatsu et al., (2013), (2010))*

I.2.2 $LaMnO_3$ / $SrMnO_3$ superlattices

In this structure LMO and SMO layers are alternated defining set of QW. The different ionic charge of La^{3+} and Sr^{2+} mean that in bulk LMO, the nominal Mn configuration is d^4, while in bulk SMO is d^3. SMO is an antiferromagnetic Mott insulator, while LMO exhibits a strong Jahn-Teller distortion. This lead to a layered antiferromagnetic structure consisting of ferromagnetic planes with alternating spin orientations.

Adamo et al. studied $(SMO)_n/(LMO)_{2n}$ and they found that, although the single layers SMO and LMO are both antiferromagnetic insulators, for $n \leq 2$ the superlattice behaves like the ferromagnetic conductor $La_{0.7}Sr_{0.3}MnO_3$ (LSMO). As n increase, the magnetic properties become dominated by LMO

layers, but the electronic properties continue to be controlled by interfaces (Adamo et al., (2009b), (2008); Aruta et al., (2009a); Galdi et al., (2012); Monkman et al., (2012)).

Santos et al. fabricated similar superlattice and studied the magnetization profile in these systems. They observed that the length scale over which the magnetization changes from an high to low value is about two unit cells (Santos et al., (2011)). This means that electronic properties can be controlled in QWs.

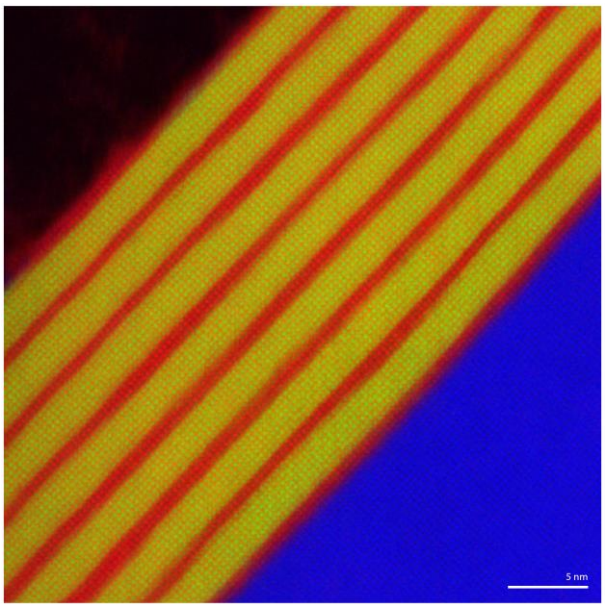

Figure I-5 *Electron Energy Loss Spectroscopy (EELS) in Transmission Electron Microscopy (TEM) map over a wide field of view (the scale bare is 5 nm) for an n = 3 $(SMO)_n$ / $(LMO)_{2n}$ grown on $SrTiO_3$ substrate showing La in green, Mn in red and Ti in blue (Monkman et al., (2012))*

I.2.3 $SrTiO_3$ based QWs

Two-dimensional electron gases at interfaces between $SrTiO_3$ and $RETiO_3$, where RE is a rare-earth, exhibit an extremely high electron densities (~10^{14} cm^{-2}) that are introduced into the *d*-bands of $SrTiO_3$.

Moetakef et al. and Zhang et al. investigated the correlation physics via *dc*-resistivity measurements of two-dimensional electron liquids that reside in narrow $SrTiO_3$ QWs. They studied the behavior of $SrTiO_3$ sandwiched between the Mott insulator $GdTiO_3$ ($GdTiO_3/SrTiO_3/GdTiO_3$) (Moetakef et al., (2012a); Zhang et al., (2014), (2013)).

The $SrTiO_3/GdTiO_3$ interfaces have strong polar discontinuity producing a sheet density of ~$3.3 \cdot 10^{14}$ cm^{-2} per interfaces (Moetakef et al., (2011)). This kind of QWs show a metal-to-insulator transition when their thickness is reduced to 3 $SrTiO_3$ layers (Figure I-6 top), while $SmTiO_3/SrTiO_3/SmTiO_3$ QWs, where $SmTiO_3$ is a Mott insulator as well, keep to be metallic also for 1 $SrTiO_3$ layer (Figure I-6 bottom) (Jackson et al., (2014); Zhang et al., (2014)).

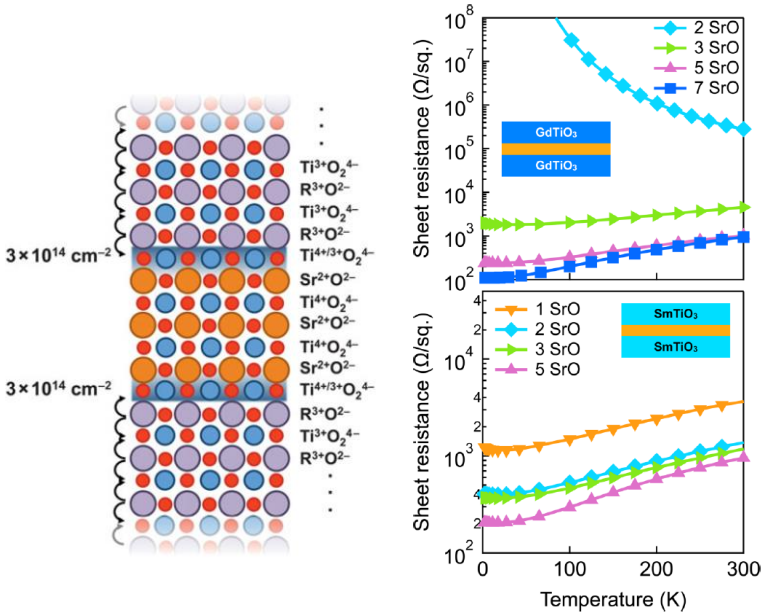

Figure I-6 *(Left) schematic showing an extreme-electron density QW where $SrTiO_3$ is embedded between two layers RETiO3 (RE=Gd,Sm); (Right) Temperature dependent sheet resistance for $GdTiO_3/SrTiO_3/GdTiO_3$ (top panel) and $SmTiO_3/SrTiO_3/SmTiO_3$ (bottom panel) as a function of $SrTiO_3$ layer thickness (Zhang et al., (2014))*

The metallic behavior of both QWs shown in Figure I-6 is due to the high electron gas density that is confined in $SrTiO_3$ by the band offset.

In particular, the different behavior shown in Figure I-6 for low $SrTiO_3$ thickness (less than 3 layers) in $GdTiO_3/SrTiO_3/GdTiO_3$ QWs compared with $SmTiO_3/SrTiO_3/SmTiO_3$ QWs has been associated by the authors to structural octahedral distortion at the $GdTiO_3/SrTiO_3$ interface, where the electron system abruptly localizes showing an insulating behavior.

This means that metal-to-insulator transition can be induced by structural distortion.

Moreover, in $GdTiO_3/SrTiO_3/GdTiO_3$ QWs Moetakef et al. observed that $GdTiO_3/SrTiO_3$ interface not only give rise to distortion in the insulation $SrTiO_3$ but also to ferromagnetism below a critical thickness absent in bulk (Moetakef et al., (2012b)).

I.2.4 $LaVO_3/SrVO_3/LaVO_3$ heterostructures

The structure and resistive properties of $SrVO_3$ sandwiched between two insulating $LaVO_3$ as a function of the thickness of the central layer (between 3 and 35 monolayers) have been investigated by Li et al. $SrVO_3$ is a correlated $3d^1$ metal oxide with a cubic symmetry and a T^2-dependent resistivity of a Fermi liquid; $LaVO_3$ was used as insulating materials because of the small lattice mismatch and the absence of interdiffusion down to the limit of some monolayers.

The sample with the thickest $SrVO_3$ layer shows a bulk-like metallic behavior, while the thinnest one show a weak localization regime observed below 100 K with a logarithmic temperature dependence. Angular-dependent magnetoresistance measurements showed a two-dimensional transport in the thinnest sample. The modification of the charge properties by the reduced thickness of $SrVO_3$ were underlined by the appearance of a relatively strong positive magnetoresistance under a magnetic field perpendicular to the sample surfaces.

As shown in Figure I-7, all the samples, therefore, present a metallic behavior above 100 K. Furthermore, the resistivity value of the sample with 3 monolayers at room temperature is only a factor of 2 higher than the reference sample, so the reduction of thickness doesn't influence essentially the conducting properties at room temperature.

Even the thinnest buried layer shows a metallic behavior, entering a weakly localized regime only at low temperature (Li et al., (2015)).

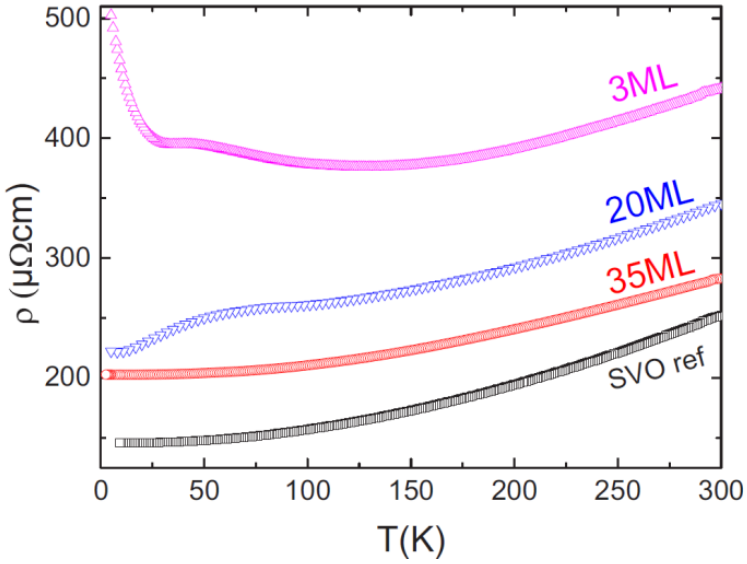

Figure I-7 *Resistivity versus the temperature for $LaVO_3/SrVO_3/LaVO_3$ trilayers as a function of the central layer thickness, that is 35, 20, 3 monolayers (ML in figure); $SrVO_3$ single layer (black curve) is shown as a reference* (Li et al., (2015))

I.3 Potential application of oxide-based heterostructures

In this Section, the potential application of oxide-based heterostructures are described paying attention, in particular, to the current state-of-art about theoretical modeling and new oxide-based devices.

I.3.1 Oxide nanoelectronics

Electronic confinement at nanoscale dimensions is increasingly challenging as the dimensionality and size scale are reduced. The interface between polar and nonpolar semiconducting oxides displays remarkable properties ascribable at modulation-doped semiconductors (Mannhart and Schlom, (2010); Ohtomo et al., (2002); Ohtomo and Hwang, (2004); Thiel et al., (2006)).

Cen et al. used $LaAlO_3$-$SrTiO_3$ heterostructures to create tunnel junctions and field-effect transistors with characteristic dimensions as small as 2 nm. These electronic devices can be successfully modified or erased, as shown in their work (Cen et al., (2009)), controlling the confinement using an atomic force microscope lithography technique. These nanoelectronic devices operates at the interfaces between a non-magnetic polar ($LaAlO_3$) and a nonpolar ($SrTiO_3$) oxide band insulators. Indeed, the discovery of a quasi two-dimensional electron gas (q2DEG) at the interface between these two materials, i.e. $LaAlO_3$ and $SrTiO_3$, has raised expectations in oxide electronics, thanks to the extraordinary properties observed. For example, a metal-to-insulator transition can be achieved at room temperature by electric field gating (Thiel et al., (2006)). In these systems, when the thickness of the polar insulator exceeds a critical value, because of polarization discontinuity at the interface, the potential difference across $LaAlO_3$ generates a "polarization catastrophe" and induce the formation of q2DEG at the interface joining the two insulators (Salluzzo, (2015); Thiel et al., (2006)).

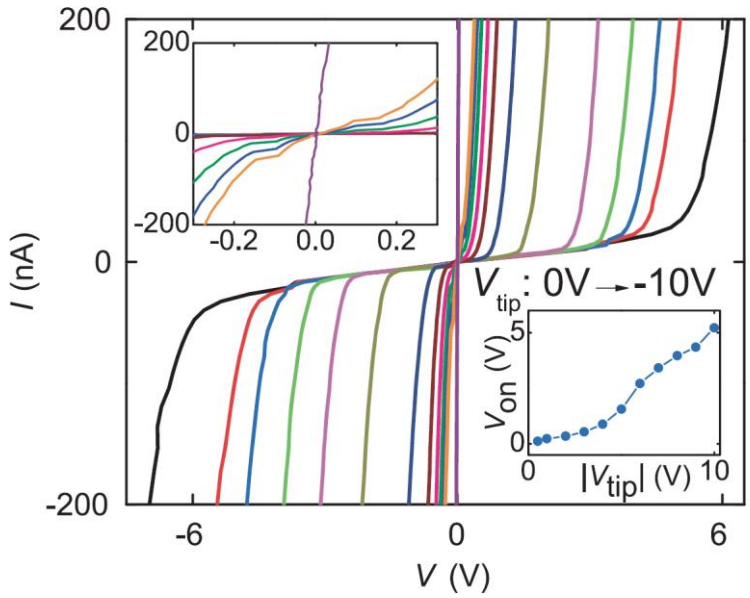

Figure I-8 *I-V characteristic of a $LaAlO_3$-$SrTiO_3$ device in function of the tip bias applied (V_{tip}=0,-0.5,-1,-2,..,-10 V). The top inset is a zoom for lower voltage. The bottom inset show the turn-on voltage of the nanowire section with a potential barrier as a function of V_{tip} that is used to create the barrier (Cen et al., (2009))*

Furthermore, an electric-field-tunable spin polarized and superconducting quasi-2D electron system can be created in $LaAlO_3/SrTiO_3$ heterostrucutures by introducing a few atomic layers of $EuTiO_3$, that is an antiferromagnetic insulator with the same structure of $SrTiO_3$. Signature of unconventional superconductivity has also been observed in $LaAlO_3/SrTiO_3$ heterostrucutures, using nanoscale Josephson junction devices. The advantages and the possibility to create and study unconventional superconducting states is another support to the fascinating possibilities offered by engineered oxides for realizing novel quantum electronics (Stornaiuolo et al., (2017), (2016))

Boucherit et al. proposed to exploit the high carrier density at $SrTiO_3/GdTiO_3$ interface. Such interfacial electron gases can be used to design innovative oxide electronic devices, such as heterostructure field-effect transistors (HFETs), shown in Figure I-9.

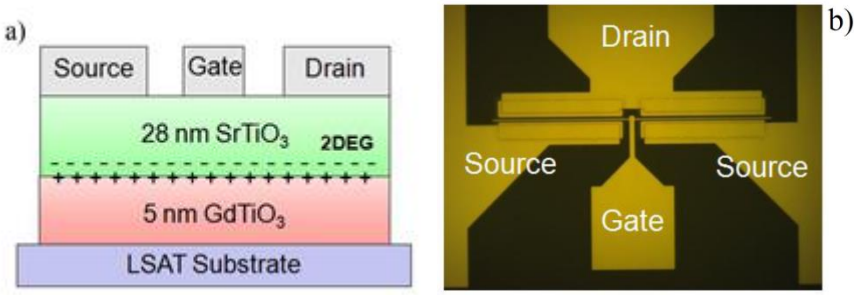

Figure I-9 *a) structure of SrTiO3/GdTiO3 HFET; b) optical micrograph of the transistor (Boucherit et al., (2013))*

Three terminal measurements were carried out on the $SrTiO_3/GdTiO_3$ HFET. The measured output characteristic of the device are shown in Figure I-10 and, for the available gate voltage range (V_G was swept from 0V to -12 V), there is a total current modulation of 20.3%. The field effect mobility of 5 $cm^2\ V^{-1}\ s^{-1}$ was extracted. The gate leakage was much lower than the drain current (Boucherit et al., (2013))

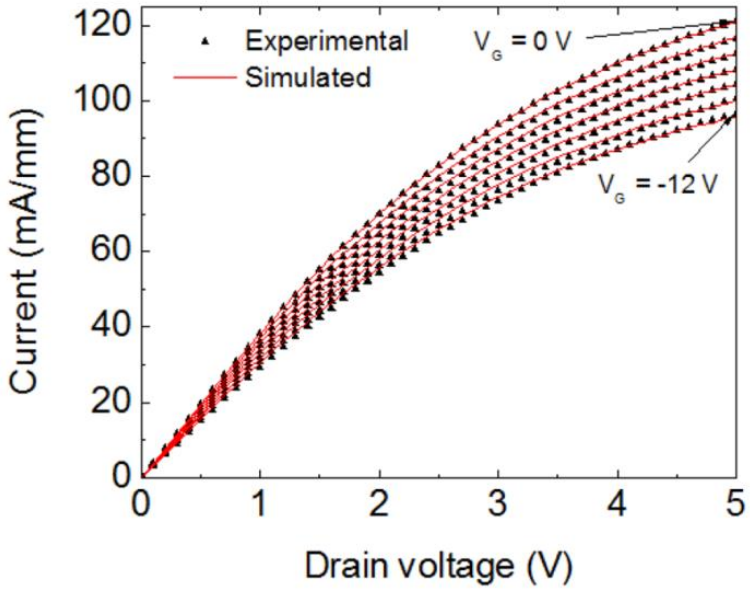

Figure I-10 *Measured and calculated output characteristic for $SrTiO_3/GdTiO_3$ HFET where the gate voltage V_G was swept from 0V to -12 V (Boucherit et al., (2013))*

I.3.2 Spintronics

In conventional electronics, information is related to the electron charge, while, in spintronics, the electron spin is used as an additional degree of freedom to perform logic operation, store information, etc., exploiting the spin-dependent electronic properties of magnetic materials and semiconductors (Bibes and Barthelemy, (2007); Žutić et al., (2004)).

Spintronic systems are of particular interest for quantum computing, in which electron spins in quantum confined structures play the role of the quantum bits (qubits). Indeed, every spin 1/2 encodes exactly one qubit (Awschalom et al., (2002)).

Experiments have supported the idea to use spin as an additional degree of freedom in electronics, showing, e.g., long spin dephasing times in semiconductors QWs and phase-coherent spin transport over distances of up to 100µm (Kikkawa et al., (1997); Kikkawa and Awschalom, (1998)). New mechanisms for information processing can be found in conventional devices (Wolf et al., (2001)) as well as in quantum confined structures used

for quantum computing (Loss and DiVincenzo, (1998)). In conventional devices, in fact, the electron spins can improve the performance, e.g. in spin-transistors, non-volatile memories, etc. (Awschalom et al., (2002)).

Oxide-based heterostructures can be used in spintronics. The main interest in this field is the possibility to obtain ferromagnetic insulator ultrathin films usable as tunnel barriers that can filter electrons selectively according to their spins, known as spin filters (Bibes et al., (2011)).

Another spintronics effect that gives rise to a large number of experimental and theoretical studies is tunnel magnetoresistance (TMR). TMR is a magnetoresistive effect that occurs in a magnetic tunnel junction, which consists in two ferromagnets separated by a thin (typically a few nm) insulator. This effect is also the basis of non-volatile magnetic random access memories (MRAMs). The large variety and tenability of the physical properties exhibited by TMOs such as perovskites (e.g. ferroelectricity, ferro- and antiferromagnetism, superconductivity, metallicity, optical properties, etc.) can be exploited in spintronics. Large TMR can be obtained using special magnetic materials (the so-called half-metals), which have a finite density of states at the Fermi level for one spin direction and a gap for the other spin direction (Bibes and Barthelemy, (2007)).

The first pioneering results about the TMR were obtained by Lu et al. on tunnel junctions based on manganese perovskite oxides ($La_{0.67}Sr_{0.33}MnO_3/SrTiO_3/La_{0.67}Sr_{0.33}MnO_3$ trilayers) (Lu et al., (1996)), and then the interest for oxides in spintronics has increased. Indeed, new families of magnetic oxides, namely, diluted magnetic oxides and multiferroics, have emerged and started to reveal their potential for spintronics.

The relevance of oxides to spintronics is not restricted to generating highly spin-polarized currents. Approaches to exploit their multifunctional character are promising and reveal new physical phenomena. Other promising approaches for oxide-based electronics and spintronics rely on engineering interfaces between two oxides to design 2D phases with novel electronic properties (Bibes and Barthelemy, (2007)). For example, $LaAlO_3/SrTiO_3$ systems, presented in the previous section, besides their potential for electronics, the high electronic mobility and 2D character make this quasi-2D electron system an interesting platform to explore lateral spin transport (spintronics) in oxide heterostructures. Measurements performed by Rayren et al. on a $LaAlO_3/SrTiO_3$ device showed efficient spin injection at the interface, using a back-gate voltage that modulates the density of states at the interface. In particular, the efficiency of spin injection into the quasi-2D electron system at the $LaAlO_3/SrTiO_3$ interface is discussed in terms of

coupling tunnel resistance with localized electronic states controlled by the application of a back-gate voltage (Reyren et al., (2012)).

I.3.3 Excitonic devices and excitonic quantum computation

Already in 1968, Kaldysh and Kozlov showed that in semiconductors with low excitonic density, i.e. $n_{ex}a_{Bohr}^{D} \ll 1$ where n_{ex} is the excitonic density, a_{Bohr} is the effective Bohr radius and *D* is the system dimensionality, the fermionic nature of excitons can be ignored. Indeed, they behave as a weakly non-ideal Bose gas and at a critical temperature T_C the can form a Bose-Einstein condensate (BEC). In particular, for a three-dimensional system the T_C is given by:

$$k_B T_C^{3D} = \frac{3.31\hbar^2 n_{ex}^{2/3}}{m_{ex}}$$

where m_{ex} is the exciton mass. If the m_{ex} is small, the expected transition temperature can be relatively higher than those typical of atomic BEC. T_C is also dependent on the exciton density and increases with increasing n_{ex} values (Keldysh and Kozlov, (1968)). In a semiconductor, the electron (hole) density can be controlled in certain ranges by suitably doping with donors (acceptors). Unfortunately, because of increased role played by the Pauli exclusion principle art educe electron-electron (hole-hole) distances, increased values of the electron (hole) density, and therefore n_{ex}, also imply that the fermionic nature of the electron-hole pairs cannot be any longer ignored. In the high density limit, i.e. $n_{ex}a_{Bohr}^{D} \gg 1$, excitons start to be similar to Cooper pairs and their condensation is analogous to a Bardeen-Cooper-Schrieffer (BCS) superconducting state (Conduit et al., (2008); Keldysh and Kopaev, (1965); Pieri et al., (2007)). The electron (hole) density, and the related role of the Pauli exclusion principle, is also crucial for the value of the ratio between the Coulomb interaction and the kinetic energy r_S, which determines the character of the system. In fact, it is known that in a system of 2D electrons or hole, low r_S values (i.e. $r_S \approx 1$) characterize a gas-like system, while intermediate values (i.e. $r_S \approx 10$) are associated to a liquid-like behavior and high values (i.e. $r_S \approx 40$) described the so called "Wigner crystal" solid. The electron (hole) density *n* and r_S are related via the formula:

$$r_S \approx \frac{1}{a^*_{Bohr}\sqrt{n\pi}}$$

where a^*_{Bohr} is the effective Bohr radius.

In the case of a 2D system with an electron (hole) density of about 10^{11} cm^{-2}, the average electron-electron (hole-hole) distance is around 30 nm. To bring this distance to 10 nm a nine-fold increase in density and kinetic energy is required. This constraint can be bypassed separating adjacent 2D electron (hole) layers with an insulating barrier 10 nm thick: an electron can "see" another electron (or hole) only 10 nm away without paying the kinetic energy cost, because the two layers continue to be separate Fermi systems (Croxall, (2010)).

The electron-hole excitonic pair spatially separated is known, as introduced in Section I.1, *indirect exciton* and due to its intrinsic separation has a lower binding energy than the direct exciton and a much longer lifetime thanks to the reduced wavefunction overlap. Moreover, the indirect exciton also carries an electric dipole allowing for further practical manipulation by external electric fields.

The crux of matter lies, therefore, in obtaining an exciton fluid at sufficiently high densities at low temperature to realize a condensed phase, where, to succeed also the disorder plays an important role. Indeed, low disorder levels may hold the exciton population required for condensation; but at large disorder level, the electrons and holes can localize in separate minima (Timofeev et al., (1998)). In other words, it would be desirable to be able to produce exciton fluids at controlled and higher densities, in system with low disorder. In this way, the energy scale of the condensate would be larger and the variation of the key properties with density could be examined. Therefore, Zhu et al. proposed a theoretical model based on semiconductor QW structures in which the excitons can be formed and condensate, and they proposed a DQW in which electron and holes are spatially separated. Thanks to this structure, following their theoretical prediction, it can be possible to control the formation of exciton condensate (Littlewood and Zhu, (1996); Zhu et al., (1995)).

Furthermore, as introduced in Section I.1, DQWs structures can be used as a mean to obtain indirect excitons, that are more stable than direct ones. Semiconductor-based DQWs have been widely studied, theoretically and experimentally, in order to obtain stable electron-hole bound state, as described by (Croxall, (2010)).

In past years, semiconductor-based quantum dots have been studied as a possible route for quantum computation (Ladd et al., (2010)) . One of the earliest proposal for quantum computation in semiconductors regarded arrays of quantum dots each containing a single electron whose two spin states provide a qubit (Loss and DiVincenzo, (1998)). Kamada and Gotoh discussed the potential application of the discrete nature of electron-hole states (i.e. excitons) to the implementation of a logic gate. The basic idea is that the electron-hole pair localized in a quantum dot can be used as elementary excitation representing logical binary; i.e. the existence (nonexistence) of exciton in the quantum dot correspond to logical one (zero) (Kamada and Gotoh, (2004)).

Excitonic devices semiconductor-based DQWs have been studied by (Grosso et al., (2009)). The principle of operation of excitonic devices is based on the control of excitonic fluxed by electrode voltages and such devices can have photonic or excitonic input and output. In the former case, photons transform into excitons at the input and exciton transform into photons at the output (High et al., (2007)). In the latter case, excitons arrive at the input from another excitonic device (High et al., (2008)).

The advantage of excitonic device is high interconnection speed, in fact efficient signal communication uses photons, while the conventional signal processing uses electrons, that are an optically inactive medium. An interconnection between electronic signal processing and optical communication causes delay and consequentially the operation speed slows down. This delay is eliminated in excitonic devices, because the excitons form a medium that can be used for signal processing and linked to optical communication.

Another advantage is the compactness and scalability. Excitonic transistors have an architecture and operation principle similar to the electronic field-effect transistors (FET). Therefore, the excitonic circuits have the potential to be similarly compact and can include as many elements as electronic circuits.

The limitation of excitonic devices are finite excitonic lifetime and finite exciton binding energy. In a direct band-gap semiconductor, the exciton lifetime is less than a nanosecond, so the excitons can travel very short distance before recombining. This problem, as anticipated, can be solved by using indirect excitons (High et al., (2008), (2007)). The lifetime of indirect excitons exceeds by orders of magnitude the lifetime of regular excitons and increased exponentially with the separation between the layers. Thanks to

their longer lifetime, the indirect excitons can travel longer distances (Grosso et al., (2009)).

Andreakou et al. obtained optical control of excitonic fluxes for indirect excitons in a semiconductor-based DQW device. This device demonstrates experimental proof of principle for optical excitonic transistors with optical input, output, control gate, using indirect excitons as operation medium. Photons transform into excitons at the optical input (source) and travel to the optical output (drain) due to the ramp potential. The output signal of the exciton emission in the drain region is controlled by a gate beam (Andreakou et al., (2014)).

I.4 Mn and Cu oxide based compounds

In this Section, the properties of Mn and Cu oxide based compounds, object of study in this work, are described in details.

The properties of TMOs are driven by *d*-orbitals and the particular occupation of a specific orbital tunes the properties of these materials. The orbital occupation is mainly determined by the interaction of the transition metal with the crystalline environment.

In this work, the attention has been focalized on two TMO based compound that show fascinating properties, i.e. the Mn oxide of the form $RE_{1-x}AE_xMnO_3$ and Cu oxide with the "infinite-layer" structure $AE_{1-x}RE_xCuO_2$, where RE is a rare earth and AE is alkaline earth.

Both classes of materials analyzed in this work show a rich phase diagram as a function of respective doping, as described in details in the following. In particular, in the Section I.4.1 the properties of manganites and in Section I.4.2 the properties of cuprates are described.

I.4.1 Properties of manganites: from the crystalline structure to the phase diagram

These materials have a rich phase diagram as a function of AE doping, showing a magnetic ordering such as antiferromagnetism and ferromagnetism.

The study of the properties of manganites started by Jonker and Van Santen, that showed a correlation between the Curie temperature, the saturation magnetization and the electrical resistivity in several $La_{1-x}AE_xMnO_3$ compound in polycrystalline form, with AE=Ca, Sr, Ba (Jonker and Van Santen, (1950)).

In these compounds, the resistivity behavior shows a transition from insulating to metallic state at metal-to-insulator transition temperature (T_{MI}) close to Curie temperature. In addition, when a magnetic field is applied at temperature around the Curie temperature of the compound, the phenomenon of colossal magnetoresistance (CMR) is observable. In Figure I-11 the correlation between the magnetization curve and resistivity one is showed for $La_{0.75}Ca_{0.25}MnO_3$ in function of the temperature and of the field applied (Ramirez, (1997)).

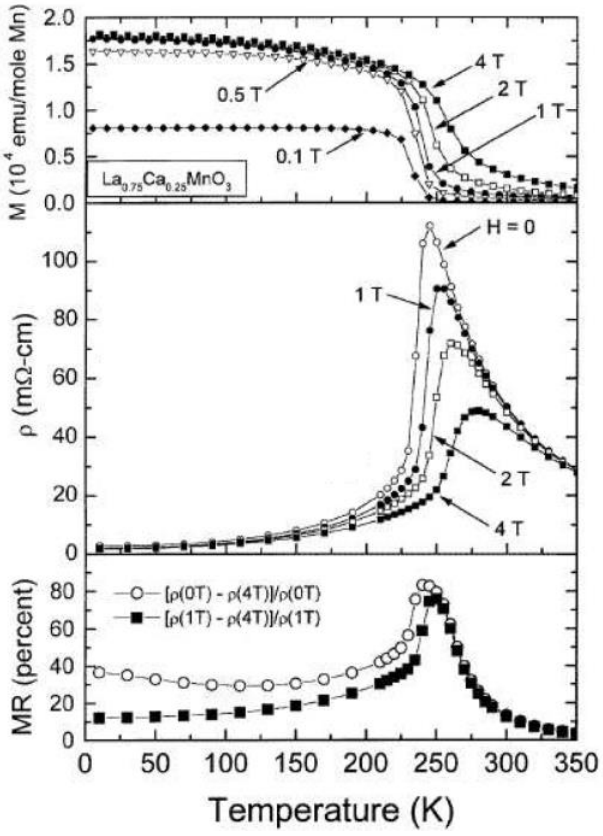

Figure I-11 *Top panel: magnetization versus the temperature and field applied for $La_{0.75}Ca_{0.25}MnO_3$; middle panel: resistivity versus the*

temperature and field applied; bottom panel: magnetoresistance versus the temperature (Ramirez, (1997))

In the top and the middle panels shown in Figure I-11, it can be observed that the onset of magnetization and the T_{MI} is pushed to higher temperature by the application of a magnetic field. The magnetoresistance is defined as

$$MR = \frac{\rho(T,0) - \rho(T,H)}{\rho(T,H)}$$

where ρ is the resistivity with and without the applied magnetic field. The magnetoresistance shown in the bottom panel in Figure I-11, is maximum in correspondence of Curie temperature and in this case it reaches the value of 80% (Ramirez, (1997)).

The rich physics of manganites is due to the intrinsic relation among the crystal structure and the magnetic and electric properties.

I.4.1.1 Crystallographic structure of (RE,AE)MnO_3

The crystallographic structure of (RE,AE)MnO_3 compounds is related to the size of RE and AE ions and in this work the attention has been focalized on cubic manganites, that are similar to cubic perovskite ABO_3. The large sized RE and AE ions occupy the A-site with 12-fold coordination, while the B-site is occupied by Mn ion with mixed valence state Mn^{3+}-Mn^{4+} and it is located at the center of oxygen octahedra with 6-fold oxygen coordination (Figure I-12 a)).

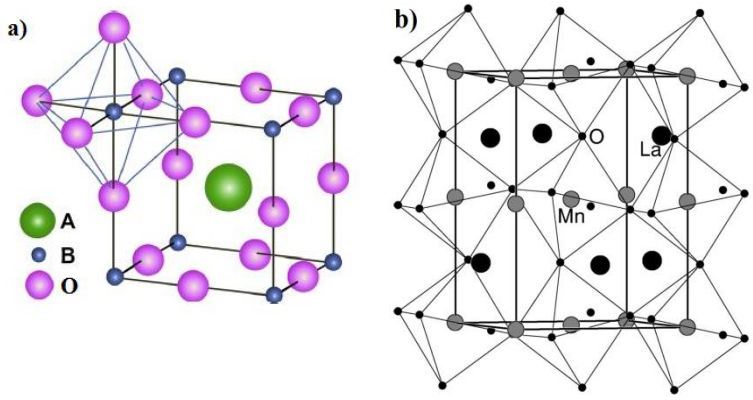

Figure I-12 *a) Schematic view of a cubic perovskite structure ABO_3; b) orthorhombically distorted perovskite-type structure*

Goldschmidt introduced a tolerance factor *t* to describe the eventual distortions of the perovskite cell and *t* is related to the dimension of the ionic radii (Goldschmidt, (1958)):

$$t = \frac{r_A + r_O}{\sqrt{2}(r_B + r_O)}$$

where r_O is the oxygen ionic radius and $r_{A,B}$ are respectively the ionic radius of A-site and B-site ions. When the A-site is occupied by two species, as happens in mixed valence manganites, an average ionic radius is considered.

The perovskite structure is stable when $0.89 < t < 1.02$ and, in particular, when $t = 1$ the structure is the perfect closely packed one. However, *t* is generally different from 1 which means that the manganites have, typically, a rhombohedrical or orthorhombic symmetry.

For example $LaMnO_3$ presents a highly distorted perovskite structure which has a quadrupled unit cell $\left(a_p\sqrt{2}, 2a_p, a_p\sqrt{2}\right)$, where a_p is the lattice parameter of the cubic perovskite structure, as shown in Figure I-12 b) (Ravindran et al., (2002)). The structural distortion observed in $LaMnO_3$ is a tilting of the MnO_6 octahedra around a cubic (110) axis, so that the Mn-O-Mn bond angle is reduced from 180° to about 160°. This phenomenon is described by the structure factor that is different from 1 and it has been proven to improve the space filling. In $LaMnO_3$ the crystal distortion is also due to the MnO_6 octahedra deformation caused by the Jahn-Teller effect originating from the orbital degeneracy. This can be view as a cooperative

shifting of the oxygen ions within the *ab* plane away from one of its two nearest-neighboring Mn atoms toward the others (Pickett and Singh, (1996)).

When the ion La^{3+} in $LaMnO_3$ is progressively substituted by a divalent AE cation, the amount of Mn^{4+} increases and the orthorhombic distortion decreases. Furthermore, $La_{1-x}AE_xMnO_3$ compounds are antiferromagnetic insulators when $x = 0$ or $x = 1$, while they show ferromagnetic behavior with a low-temperature conductivity similar to metals when $0.2 < x < 0.5$.

I.4.1.2 Electronic properties: Jahn-Teller effect and double-exchange mechanism

The structural, magnetic and electrical transport properties of Mn oxides are interrelated and are induced by the mixed valence on Mn ions (Mn^{3+}-Mn^{4+}).

For an isolated 3*d* ion, five degenerated orbital states are available. This degeneracy is partially lifted by the crystal field. The five *d*-orbitals are split by a cubic crystal field into three orbitals, called t_{2g}, (d_{xy} , d_{yz} , d_{zx}) and two orbitals, known e_g, (d_x^2-d_y^2 , d_z^2-d_y^2). The Hund's rules ensure the alignment of the electron spins in t_{2g} orbitals. The e_g orbitals are empty for Mn^{4+} ion, while for Mn^{3+} there is an electron. In a crystal field with symmetry different from cubic one, the further degeneracy of the t_{2g} and e_g levels is avoided for the axial elongation of oxygen octahedron. This distortion is known as Jahn-Teller distortion (Figure I-13).

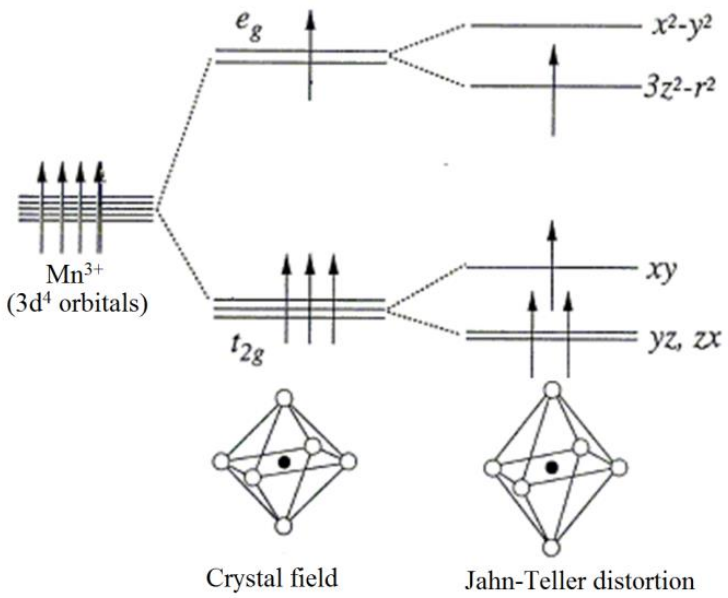

Figure I-13 *Jahn-Teller distortion. On the left: 3d-orbitals degeneracy of Mn^{3+} single ion; in the center: degeneracy partially removed thanks to crystal field (interaction with oxygen octahedrals); on the left: degeneracy further removed thanks to octahedral elongation (Jahn-Teller distortion).*

The magnetic properties of manganites are governed by exchange interaction between Mn ion spins. These interactions are relatively strong between the Mn ion interacting with Oxygen atoms and are controlled by the overlap between the Mn *d*-orbitals and the O *p*-orbitals.

In particular, the interaction Mn^{4+} - O^{2-} - Mn^{4+} is antiferromagnetic, while the interaction Mn^{3+} - O^{2-} - Mn^{3+} can be ferromagnetic or antiferromagnetic (Goodenough, (1955)).

When the interaction in mixed valence manganites occurs, it is typically between Mn^{3+} - O^{2-} - Mn^{4+} ions where Mn ions can exchange their valence by simultaneously jump of the e_g electron of Mn^{3+} on the O *p*-orbital and from the O *p*-orbital to the empty e_g orbital of Mn^{4+}. This mechanism is known as “double exchange” (Zener, (1951)), as schematized in Figure I-14.

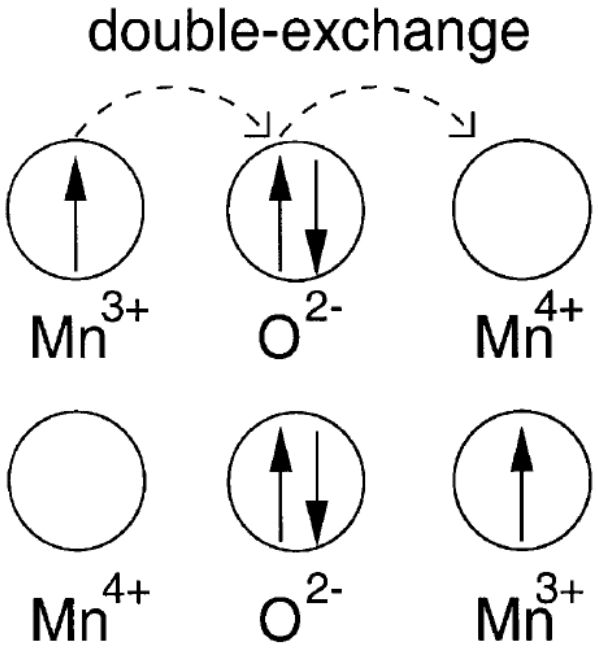

Figure I-14 *A schematic representation of double exchange mechanism in mixed valence manganites (Dagotto et al., (2001))*

I.4.1.3 Doped compounds: $La_{1-x}Sr_xMnO_3$ phase diagram

When AE^{2+} is substituted to RE^{3+} in (RE,AE)MnO_3 compounds, Mn^{3+} partially change its valence in Mn^{4+} in order to keep the charge neutrality. This can be seen as holes introduced in e_g band and, consequentially, some charge carriers become available for real hopping processes.

$La_{1-x}Sr_xMnO_3$ (LSMO) offers a very rich physics as a function of doping, as it can be observed from its phase diagram (Figure I-15).

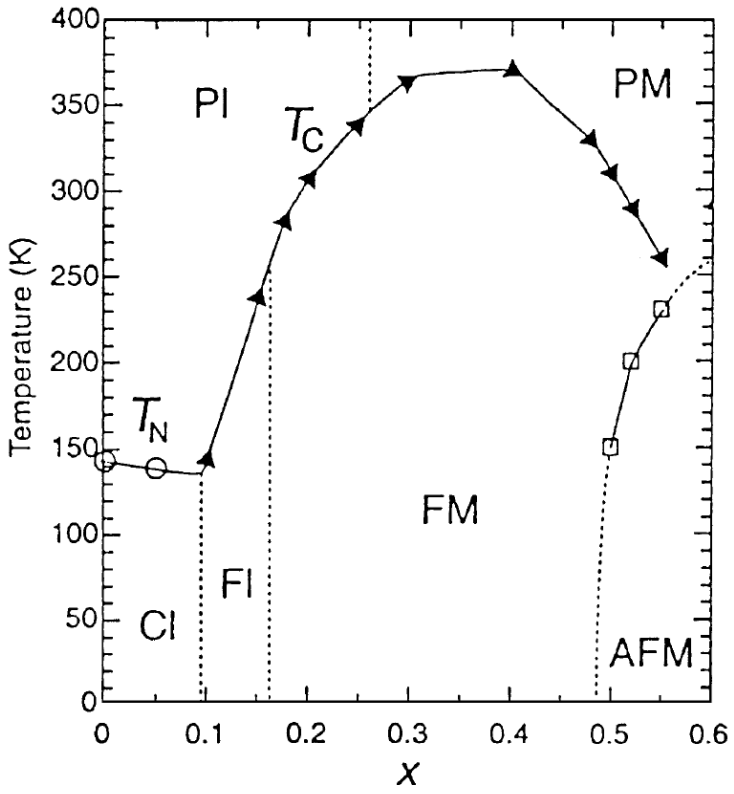

Figure I-15 *Phase diagram of $La_{1-x}Sr_xMnO_3$ as a function of Sr content x (Dagotto et al., (2001))*

$LaMnO_3$ is obtained at $x = 0$ that is an antiferromagnetic insulator with Néel temperature $T_N \approx 140K$.

At very low doping ($x \lesssim 0.1$) is in spin-canted insulator (CI) state. The ferromagnetic phase can be already obtained at $x \approx 0.1$, where at low temperature, the LSMO is a ferromagnetic insulator (FI) up to $x \approx 0.15$; then it becomes ferromagnetic metallic (FM) for $0.15 \lesssim x \lesssim 0.5$ when the double exchange mechanism takes place. At higher doping ($x \gtrsim 0.5$) LSMO becomes antiferromagnetic with uniform orbital ordering (AFM). In addition, PI and PM in Figure I-15 denotes, respectively, paramagnetic insulator and paramagnetic metallic states and T_C is the Curie temperature.

In this work, the attention has been focalized on LSMO with $x = 0.3$ doped in the central layer of *p*-type QWs studied, where the highest Curie temperature is present.

Finally, for $x = 1$ $SrMnO_3$ (SMO) is obtained, that has been used in *p*-type QWs studied in this work as top and bottom insulating layers. SMO is an antiferromagnetic Mott insulator with a gap value of about 0.35 eV and a Néel temperature of 230 K (Maurel et al., (2015); Søndenå et al., (2006)).

I.4.2 Properties of cuprates: from the crystallographic structure to the phase diagram

Cu based compounds present a lot of interesting physical properties, but the most investigated is the high temperature superconductivity. Since its discovery in a ceramic La-Ba-Cu-O compound in 1986, a lot of progress have been done. Nevertheless a theoretical and predictive microscopic model doesn't exist yet, but a number of general conclusion have been drawn by comparing properties across the entire cuprate family (Leggett, (2006)).

It has been observed that the parent compounds of cuprates are antiferromagnetic insulators and, doping them, the antiferromagnetism is reduced and superconductivity appears. Furthermore, all superconducting cuprates are layered materials with CuO_2 planes.

The mechanism behind high temperature superconductivity is different from the conventional superconductivity, that is well described by the J. Bardeen, L. N. Cooper, J. R. Schrieffer (BCS) theory (Bardeen et al., (1957)). Indeed, the properties of cuprates are highly anisotropic due to the layered nature of cuprates. Then, the superconducting coherence lengths are much smaller than the conventional superconductor ones, suggesting a different pairing mechanism than the phonon exchange happening in conventional superconductors. Furthermore, the conventional superconductors are characterized by *s*-wave symmetry, while the cuprates are characterized by *d*-wave symmetry.

I.4.2.1 Crystallographic structure of infinite-layer cuprates

The infinite-layer (IL) cuprates have the simplest crystal structure among the known cuprate families. The parent compound is $ACuO_2$, where perfectly square and flat CuO_2 planes are separated by layers of alkaline earth atoms, such as Sr, Ca, as shown in Figure I-16.

The superconducting compound is achieved via heterovalent substitution at the alkaline earth site. For example, in $Sr_{1-x}La_xCuO_2$, each atom donates one electron to the CuO_2 plane, resulting in *x* extra electron per copper atom.

The structure of ILs is unique among the cuprates because the *c*-axis between Cu planes is less than in-plane value. In addition, the electron hopping along the *c*-axis is inhibited by the lack of apical oxygen ligands.

Also the crystal structure of the other known electron doped family (for example $RE_{1-x}Ce_xCuO_4$) lacks apical oxygen, but, at the present, it is not clear why such absence plays an important role in the superconducting properties of electron-doped cuprates and systematic studies are therefore important (Fournier, (2015)).

In spite of its structural simplicity, the IL cuprate is quite sensitive to growth conditions, indeed an oxygen-reduction step after growth is required in order to induce superconductivity. It is believed that the reduction step removes a small amount of excess oxygen atoms present in the as-grown materials at apical sites (Feenstra et al., (1994); Jiang et al., (1993); Li et al., (2009); Richard et al., (2007)), but at the same time there are many alternative theories involving oxygen deficiency within the CuO_2 planes (Kang et al., (2007); Richard et al., (2004); Wang et al., (2009)).

The mechanism behind the suppression of superconductivity induced by a relatively small amount of excess oxygen is not known yet, so, again, a systematic study as a function of the after growth annealing is crucial and it has been performed in this work also by using advanced synchrotron radiation based electronic spectroscopies.

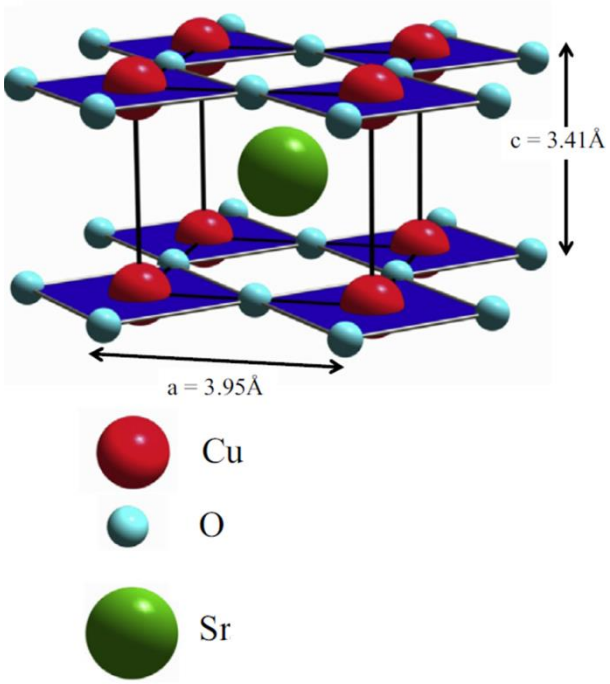

Figure I-16 *IL crystal structure of $SrCuO_2$. The typical values for the lattice parameters are shown as a reference (Fournier, (2015))*

The choice of the substrate is important when growing IL thin films because the strain plays an important role in the right phase formation. Films under tensile strain are in general of better quality than films under compressive stain, exhibiting lower resistivity and higher critical superconductive temperature. This is due to the tensile strain that allows easier removal of interstitial oxygen atoms, but excess tensile strain leads to lattice defects and substrate interdiffusion (Karimoto and Naito, (2004)). The best substrates for the growth of superconducting $Sr_{1-x}La_xCuO_2$ are (110) $DyScO_3$, $TbScO_3$, $GdScO_3$.

I.4.2.2 Properties of (Sr,La)CuO_2

Because of the unavailability of large single crystals, the IL cuprates have not been deeply investigated as the more studied hole-doped cuprates. The

existing studied have brought conflicting conclusion regarding the nature of superconductivity and ferromagnetism in ILs.

Recent advantages in the oxide deposition by molecular beam epitaxy (MBE), described in Section II.1, has made available IL $Sr_{1-x}La_xCuO_2$ epitaxial thin films with structural quality comparable to those of single crystals.

Harter et al. shed light on the electronic structure of IL $Sr_{1-x}La_xCuO_2$ epitaxial thin films thanks to *in-situ* Angle Resolved Photoemission Spectroscopy (ARPES) measurements. Their observations demonstrated a clear coexistence of superconductivity with robust antiferromagnetism order, both intrinsic features of electron-doped cuprates and not material specific (Harter et al., (2012)).

In Figure I-17 a **k**-resolved map of spectral weight near the Fermi energy is shown. A large circular Fermi surface centered at (π,π), generic to all doped cuprates, is reported. Yellow and grey arcs are extracted by theoretical calculations. More details can be find in Ref. (Harter et al., (2012)).

Furthermore, they studied the doping evolution of IL $Sr_{1-x}La_xCuO_2$ thin films. In particular, it was observed that the upper Hubbard band in this material evolves into a metallic Fermi surface increasing the La content, while a remnant low Hubbard band, characteristic of cuprate parent compounds, coexists with coherent low-energy states even at optimally doping (Harter et al., (2015)). A description of the Hubbard model, that is the simplest model of interacting particles, can be find in Appendix A.

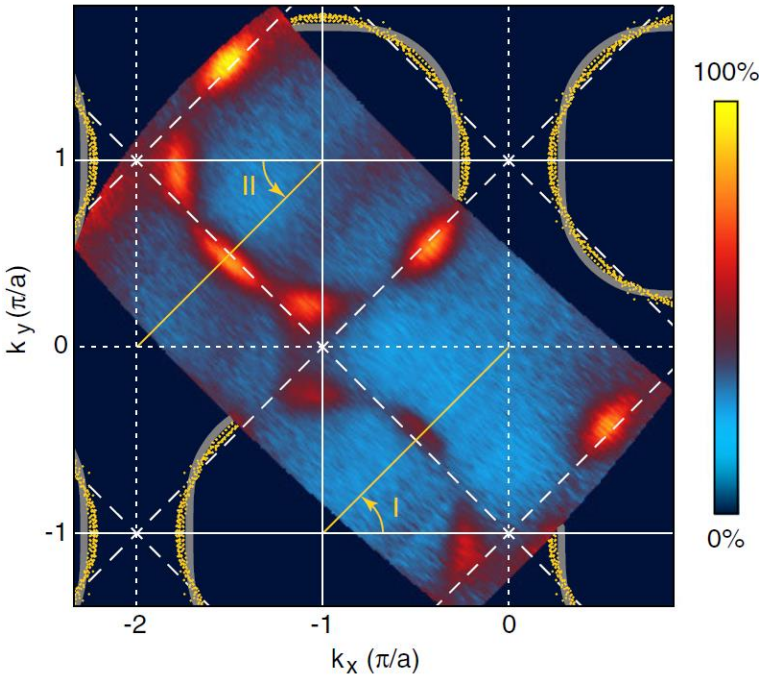

Figure I-17 *Unsymmetrized Fermi surface mapping of optimally doped* $Sr_{0.9}La_{0.1}CuO_2$ *taken at 10K. The gray and yellows arcs are obtained from theoretical calculations (Harter et al., (2012))*

I.4.2.3 Phase diagram of cuprates

The actual doping-temperature phase diagram of cuprate superconductors is asymmetric. Both the electron (*n*) and hole-doped (*h*) cuprates present, in the lower doping part of their phase diagram, antiferromagnetic behaviors with parent undoped compounds being antiferromagnetic insulators and, below a compound specific doping level, they show a sudden upturn in the low temperature planar *dc*-resistivity (Armitage et al., (2010); Rybicki et al., (2016)). In particular, the low doping antiferromagnetic phase appears much more robust, extends to much higher doping on the electron-doped side and sometimes coexists with superconductivity. On the other hand, for hole-doped cuprates, the antiferromagnetic phase is rapidly suppressed with the doping and far below the onset of superconductivity.

For both the *n* and *p* doped superconducting cuprates, a linear temperature dependence of the resistivity is observed at $T > T^*$, with doping-dependent T^* values, persisting up to high-temperature values around 1000 K (Gurvitch and Fiory, (1987)). The temperature T^* separates the so-called strange-metal regime ($T > T^*$) from the region with the opening of a pseudo-gap (Li et al., (2008); Shekhter et al., (2013)).

The opening of the pseudo-gap below T^* has been attributed to non-Fermi liquid behavior in proximity of a quantum critical point, generally identified as the quantum transition to the antiferromagnetic phase (Keimer et al., (2015); Li et al., (2008); Shekhter et al., (2013)).

Nevertheless, recent developments have suggested that a FL behavior is present below T^{**} in a large part of the normal state phase diagram. In particular, *p*-doped cuprates have shown, below $T^{**} < T^*$, a quadratic temperature dependence of the resistivity per CuO_2 planes (Barišić et al., (2013)), a single relation scattering rate $1/\tau \cong T^2$ in agreement with the Kohler's rule for the magnetoresistivity (Chan et al., (2014)) and a quadratic frequency dependence of the optical scattering rate with the temperature-frequency scaling expected in the case of Fermi liquid (Mirzaei et al., (2013)).

Probably due to the *n*-type material scarcity and to the difficulty in growing high quality samples, the data on the *n*-side of the cuprate phase diagram are not as ample as those on the *p*-side. This obviously renders more difficult to reach a comprehensive understanding of the high-temperature superconductivity which requires an explanation of the very complex phase diagram of cuprates.

In Figure I-18 a schematic phase diagrams of hole-doped (Barišić et al., (2017)) and electron-doped cuprates (Harter, (2013)) are shown.

In this work, a systematic study of IL electron-doped properties has been done in order to increase the available data on the *n*-side cuprate phase diagram, including the IL cuprate family with its interesting peculiarities.

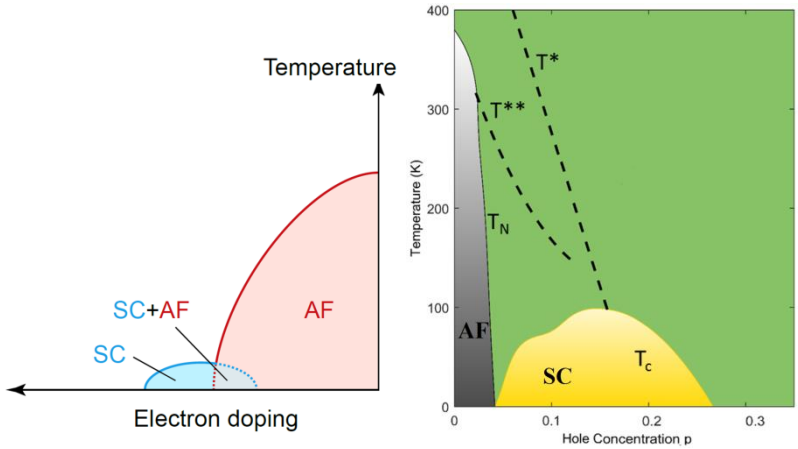

Figure I-18 *Doping – temperature phase diagram of cuprate superconductors where the antiferromagnetic (AF) and superconductive (SC) phases are shown both for electron-doping (left) and hole-doping (right). Néel temperature (T_N), temperature where the resistivity shows a linear behavior in temperature (T*) and a quadratic behavior in temperature (T**) are indicated for the hole-doped cuprates (right)*

In particular, as shown in the right panel in Figure I-18, the dashed lines separate two regions in the normal state of the *p*-doped cuprates, as already mentioned, at temperature above *T**, the *p*-doped cuprates present planar resistivity with an approximately linear temperature dependence ($\rho \propto T$); while below the characteristic temperature *T***, a Fermi-liquid behavior is observed where the resistivity shows a quadratic dependence in temperature ($\rho \propto T^2$) (Barišić et al., (2017), (2013)).

More recently, similar behaviors, previously probability masked by the large nonmetallic contribution, have also been observed in several *n*-doped cuprates (Li et al., (2016)). In particular, values of the planar resistivity coefficients very close to those measured for *p*-doped compounds with the same doping level have been observed along with transport scattering rates similar to the ones obtained in the case of *p*-doped materials, strongly suggesting a universal description of the normal state in cuprates, independently of doping, compound and carrier type.

In this work, the presence of these low temperature Fermi liquid behaviors IL $Sr_{1-x}La_xCuO_2$ thin films have also been analyzed. The obtained results seem to confirm a robust and universal Fermi liquid charge transport

behavior in the low temperature properties of IL *n*-doped cuprate superconductors.

Chapter II
Experimental techniques

II.1 Deposition technique: Molecular Beam Epitaxy (MBE)

It is extremely important to be able to grow high quality single-crystal stoichiometry-controlled epitaxial films in order to be used for industrial applications. The word “epitaxy” derives from Greek root *epi*, meaning “above”, and *taxis*, meaning “an ordered manner: the epitaxial growth means that the deposited material form a crystalline overlayer that has one well-defined orientation with respect the substrate crystal structure.

The techniques usually employed to grow thin films under high vacuum conditions can be physical or chemical vapor deposition (PVD or CVD): in PVD techniques, the compounds are vaporized from material sources and transported through the vacuum reactor towards the substrate without producing any chemical reaction; in CVD techniques, precursor species containing the elements of the desired compound chemically react in order to grow the film on the surface of the substrate crystal.

The samples reported in this work have been mainly grown using a PVD technique: the MBE deposition mode.

The MBE was developed in the late 1960’s in order to grow semiconductor compounds and it has been adapted to grow different materials from metals and oxides to complicated heterostructures. This technique distinguishes from other epitaxial growth methods for the high precision control over the beam fluxes and growth parameters. Indeed, the

MBE has the advantage to be *in situ* controlled by surface diagnostic method such as Reflection High-Energy Diffraction (RHEED), described in the following section. This "real time" diagnostic methodology is possible because of the ultra-high vacuum (UHV) conditions and it enables the fabrication of sophisticated structures.

The molecular beams are generated under UHV conditions from sources of the Knudsen-effusion-cell type (Herman, (1982)), represented in Figure II-1, and travel across the system in ballistic regime reaching the substrate region where the beams interact with the gases (e.g. oxygen or ozone for oxide based thin films) that can be introduced in this chamber region. Finally, the beams condensate on the heated crystalline substrate.

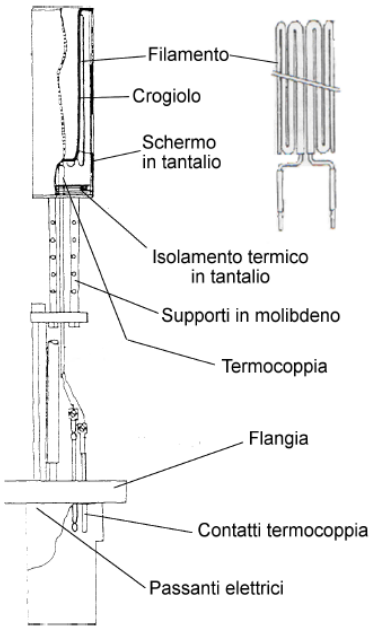

Figure II-1 *Effusive cell used in the University of Salerno MBE deposition system. The effusive cells are closed by shutters that can be manually or computer controlled by pneumatic actuators.*

The temperatures of the substrate and of the cells needs to be properly chosen in order to obtain the growth of the desired phase. Indeed, the evaporation rate for the effusive cells is determined by the crucible

temperature, by the external pressure and by geometrical factors (e.g. cells aperture area, the position respect to the substrate). Most of these parameters can be fixed and the rate can be very precisely controlled by the cell temperature (Herman, (1982)). The deposition rate (deposition flux as well) is measured by a Quartz Crystal Monitor (QCM), described in the following section.

II.1.1.1 Flux measurements: Quartz Crystal Monitor (QCM)

To measure the deposition rate of an element evaporated by an effusive cell, a quartz crystal is located on the same horizontal plane of the substrate holder. The mass of a material deposited on the crystal quartz changes producing a measurable shift in the resonant frequency. The crystal quartz is connected to a thickness monitor that shows the deposition rate.

II.1.1.2 Reflection High Energy Electron Diffraction (RHEED) in-situ diagnostic

RHEED observation allows the monitoring of the sample growth and it can be used in MBE systems thanks to UHV conditions characteristic of the growth environment. RHEED uses electron, whose energy is in the 5-50 keV range, that are produced by an electron gun. The electron beam is focused and collimated to impinge on the substrate (or the sample) with a grazing angle usually less than 5°. The RHEED diffraction pattern generated by the sample surface is displayed on a phosphor screen located in the opposite position, as shown in Figure II-2.

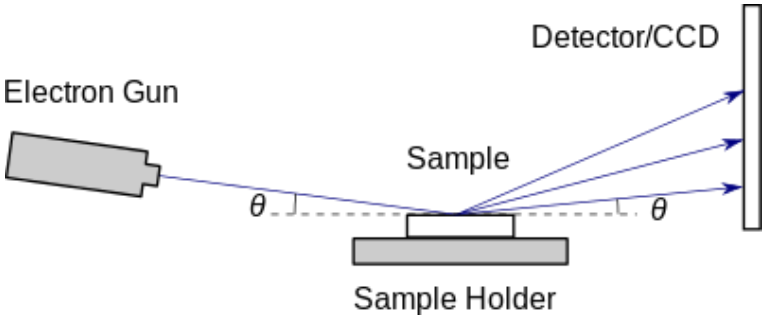

Figure II-2 *Schematic diagram of RHEED geometry showing the incident beam to the surface sample with angle θ.*

The diffraction of the incident primary beam on the 2D lattice of the sample surface shows streaks (or rods) on the fluorescent screen used as detector.

The streaks position on the screen is related to the screen in-plane lattice parameters and the lattice can be considered 2D because of the electrons low incidence angle. The distance between two adjacent streaks is given by:

$$d = \frac{Lg_{//}}{k}$$

where L is the distance between the substrate and the phosphor screen, $k = (2h/k)\sqrt{2mE}$ is the wave vector of the primary beam with energy E and $g_{//} = 2\pi/a_0$ where a_0 is the lattice constant.

If during the growth 3D island are formed, additional spots appears on the pattern, so the film growth mode can be identified by the qualitative pattern change.

The central rod in the streak pattern is the specular one and it is the mirror like reflection of the electron beam. The specular streak gives information about the flatness and the quality of the surface. Its width is generally limited by the instrument resolution.

The specular streak and the higher order ones are due to the elastic scattering of the electron beam. The intensity of the RHEED pattern shows an oscillatory behavior in time which is directly related to the growth rate (Van Hove et al., (1983)), so it can be used to calibrate beam fluxes more accurately in order to control the film stoichiometry and the thickness as well.

In this work, the film constituents are sequentially deposited (layer-by-layer) on an appropriate substrate and the opening of pneumatic shutters of the sources are calibrated by monitoring RHEED intensity oscillations. The variation in the intensity of oscillations is related to the stoichiometry of the deposited compound and to the exact completion of unit cells. This technique allows the use of RHEED not only for morphology but also for stoichiometry control.

As described before, the QCM calibration is used to calibrate the flux (and equivalently the temperature) of each single element and then the layer-by-layer RHEED calibration gives a better control on the stoichiometry.

A typical example of layer-by-layer RHEED calibration of $SrTiO_3$ is show in Figure II-3. Sr and Ti are sequentially deposited while the heated substrate is immersed in a continuous molecular O_2 flux (the deposition pressure is kept constant) (Haeni et al., (2000)).

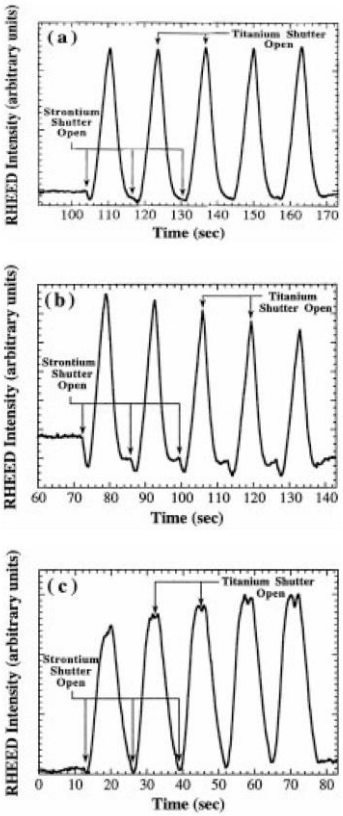

Figure II-3 *$SrTiO_3$ layer-by layer RHEED intensity oscillations acquired on the central streak. The opening of Sr shutter and Ti shutter is indicated. (a) Stoichiometric full monolayer of Sr and Ti deposited; (b) Sr dose is held constant while Ti dose increased by 3% from a full monolayer; (c) Sr dose is held constant while Ti dose decreased by 3% from a full monolayer (Haeni et al., (2000))*

II.1.2 The MBE deposition system present at UNISA

(La,Sr)MnO_3 single layer thin films and $SrMnO_3/La_{0.7}Sr_{0.3}MnO_3/SrMnO_3$ QWs have been grown with the MBE deposition system present at University of Salerno. It is schematically shown in Figure II-4.

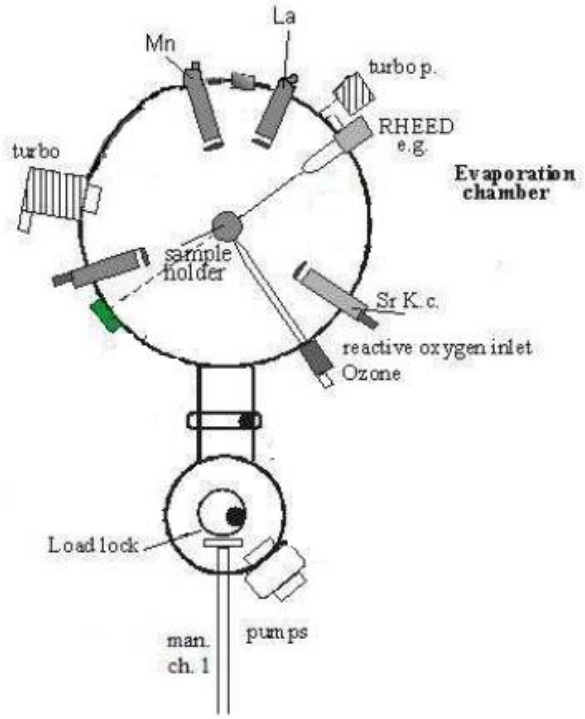

Figure II-4 A schematic representation of MBE system located at UNISA

The MBE present at UNISA laboratory (model ISA-RIBER EVA32) is composed by a main deposition chambers constantly kept in UHV ($<10^{-8}$ Torr) and an intro chamber (load-lock) that allows to load samples without breaking the vacuum in the growth chamber.

The materials are evaporated through three effusive (Knudsen) cells in the growth chamber (it is possible to allocate a fourth source); in particular, La is evaporated by high temperature effusive cell and the others are the effusive cells for Sr and Mn. Regular effusive cells have a pyrolytic PBN crucible and can reach temperature up to 1000°C; high temperature effusive cell used for La has Ta crucible and can reach temperature up to 2000°C. These temperatures can be in principle reached because all the sources have a water cooled shield.

O_2 molecular gas or a mixture of Oxygen and 10% Ozone can be introduced in the chamber for the oxide formation.

The sample holder can be rotated during the growth and can be heated up to 750°C.

II.1.3 The MBE deposition system present at Cornell Univesity

The samples (Sr,La)CuO_2 and the $SrCuO_2/Sr_{0.9}La_{0.1}/SrCuO_2$ QWs have been grown using the MBE present at Cornell (model VEECO GEN10) is shown in Figure II-5. It is composed by two twin deposition chambers (GM1 and GM2) connected by a distribution chamber kept in UHV ($<10^{-10}$ Torr). The load-lock is in the clean room and it is connected to the distribution chamber. An Angle-Resolved Photoemission Spectroscopy (ARPES) system is also connected to the distribution chamber, so the samples can be immediately measured without breaking the vacuum.

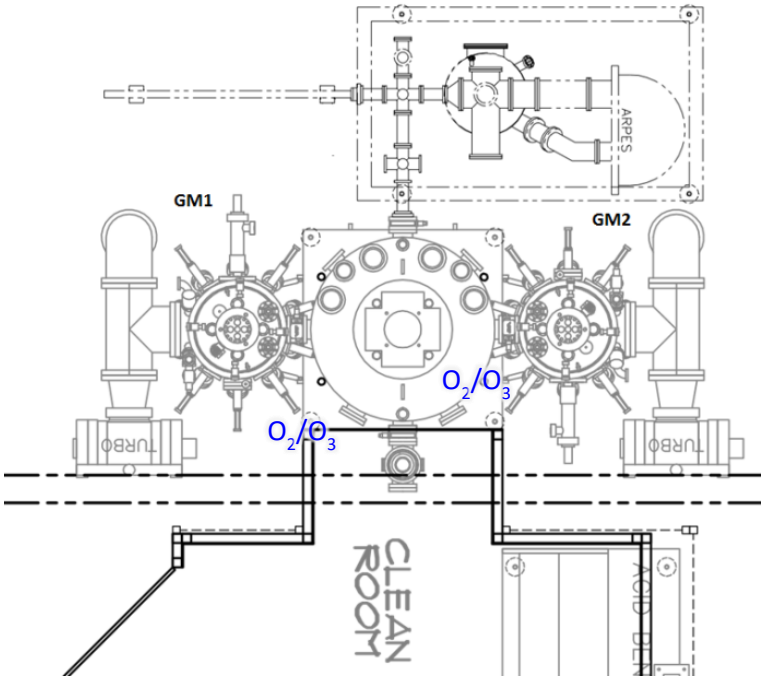

Figure II-5 *Schematic representation of the MBE system at Cornell University*

In each growth chamber it is possible to allocate 9 different effusive sources and an electron beam (it is used to evaporate materials using an electron beam and whose temperature is too high for the effusive cells). The effusive sources have the same operating principle of the MBE at UNISA.

Thanks to an Ozone distiller, it is possible to introduce pure Ozone in the chamber for the oxide formation as well as O_2 molecular gas or a mixture of Oxygen and Ozone.

II.2 Standard thin films characterization technique

II.2.1 X-Ray Diffraction (XRD) technique for thin films structural characterization

Thanks to X-ray wavelength with the same order of magnitude of interatomic distance in crystals, the XRD measurements are very important to investigate the crystalline structure of materials.

II.2.1.1 XRD theory: Bragg reflection

Where The X-Ray, incident on a crystal, interacts with its atoms through electron-photon scattering. In an ideal crystal of dimension N_1a, N_2b and N_3c in the direction of the primitive lattice vectors **a**, **b** and **c** and a radiation with incident wave vector $\mathbf{k_0}$ and scattered wave vector **k**, the diffracted intensity is:

$$I \propto |F(\mathbf{Q},\lambda)|^2 \frac{\sin^2\left(N_1\mathbf{Q}\cdot\frac{\mathbf{a}}{2}\right)}{\sin^2\left(\mathbf{Q}\cdot\frac{\mathbf{a}}{2}\right)} \cdot \frac{\sin^2\left(N_2\mathbf{Q}\cdot\frac{\mathbf{b}}{2}\right)}{\sin^2\left(\mathbf{Q}\cdot\frac{\mathbf{b}}{2}\right)} \cdot \frac{\sin^2\left(N_3\mathbf{Q}\cdot\frac{\mathbf{c}}{2}\right)}{\sin^2\left(\mathbf{Q}\cdot\frac{\mathbf{c}}{2}\right)}$$

where $\boldsymbol{Q} = \boldsymbol{k} - \boldsymbol{k_0}$ and $F(\boldsymbol{Q},\lambda)$ is the structure factor depending from the wavelength λ and that is related to the atomic form factors (such as scattering from the electrons of each atom in an unit cell) and from the position of any atom in the unit cell. The scattered intensity, in this approximation, is a Fraunhofer pattern modulated by the structure factor.

Intensity maxima are obtained when $\boldsymbol{Q} \cdot \boldsymbol{a} = 2h\pi$; $\boldsymbol{Q} \cdot \boldsymbol{b} = 2k\pi$; $\boldsymbol{Q} \cdot \boldsymbol{c} = 2l\pi$ with *h, k, l* integers. This is the Laue condition for constructive interference given when the difference among the scattered and the incident wave vectors $\boldsymbol{Q} = \boldsymbol{k} - \boldsymbol{k_0}$ equals a reciprocal lattice vector $\boldsymbol{K}$ (defined by the condition $\boldsymbol{K} \cdot \boldsymbol{R} = 2n\pi$ where $\boldsymbol{R}$ is any crystal lattice vector $\boldsymbol{R} = n_1\boldsymbol{a} + n_2\boldsymbol{b} + n_3\boldsymbol{c}$). Laue condition is equivalent to Bragg formula, where the crystal is considered composed by parallel plans of ions distant *d*. The constructive interference of the beam reflected by successive planes is given when the optical path difference is a multiple integer of the wavelength λ:

$$n\lambda = 2d\ sin\theta$$

where *n* is the order of the reflection and θ is the radiation incidence angle on the family planes.

A schematic Bragg's law configuration is shown in Figure II-6.

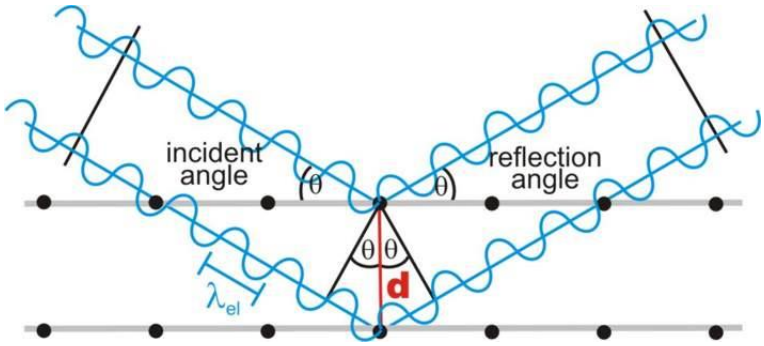

Figure II-6 *Schematic Bragg's law depicting the constructive inference of reflected waves*

II.2.1.2 Thin film measurements configuration: θ-2θ scan and X-Ray Reflectivity (XRR) measurements

The Bragg configuration is used for studying the structure of thin films. A monochromatic radiation is used and the incident beam is collimated by narrow slits to hit the sample surface with angle ω. A detector measures the reflected intensity from the surface of the sample at angle 2θ respect the incident beam direction. In the simplest case of two circle diffractometer

these are the only degree of freedom. In a three circle diffractometer the sample can be rotated with angle φ along an axis perpendicular to its surface. In a four circle diffractometer the sample can tilt by an angle ψ around the axis in the sample plane belonging to the incidence plane of radiation. Five and six circle diffractometer also exist that are used for grazing angle and surface diffraction.

The diffractometers used to characterize the samples for this work are a three circle at University of Salerno and a four circle at Cornell University.

θ-2θ scan

The incident angle ω is set to θ and the scattering vector ***Q*** is perpendicular to the sample surface. This is analogue to look for specular reflection of the crystalline planes parallel to the sample surface. If the film is single oriented, it is only possible to measure the lattice parameter perpendicular to the surface (out-of-plane). If the crystal planes are well aligned along all the sample thickness, interference fringes are detectable. From the maxima position of the fringes it is possible to estimate the sample thickness:

$$t = \frac{(i - j)\lambda}{2(\sin\theta_i - \sin\theta_j)}$$

where *i* and *j* are the order of maxima and θi and θj are the maxima positions.

X-Rays Reflectivity (XRR) measurements

The same equipment and configuration of θ-2θ scans can also be used for XRR analysis of thin films. This analysis can be used to determine the density, thickness and roughness of each layer of a multilayered film. A single layer can be seen as a bilayer with the substrate (that is very thick).

In a multilayered structure the X-rays reflects from each surface and the multiple reflected waves interfere with each other producing reflectivity curve. The interference fringes are created by phase differences between X-rays reflected from different layers and the distance between fringes is inversely proportional to the thickness of the layer:

$$t = \frac{(i - j)\lambda}{(2\theta_i - 2\theta_j)}$$

XRR measurements are performed at low angle so $\sin\theta_i \approx \theta_i$ (in rad).

The film roughness causes X-rays to be scattered rather than reflected producing the loss of beam intensity increasing theta. In other words, the roughness determines how quickly the reflected signal decays.

The film density and its composition is related to the critical angle below which the X-rays are completed reflected. This critical angle is a function of the layer electron density (if the film density increases, also the critical angle increases).

The samples measured have been fitted using the Rigaku GXRR and IMD software with the layer thickness, density and roughness as free fitting parameters.

II.2.2 Electrical transport measurements

The electrical transport measurements as a function of the temperature were carried out by the four probe dc technique in a Van der Pauw contacts configuration (Van der Pauw, (1958)) without patterning the samples, as schematically shown in Figure II-7.

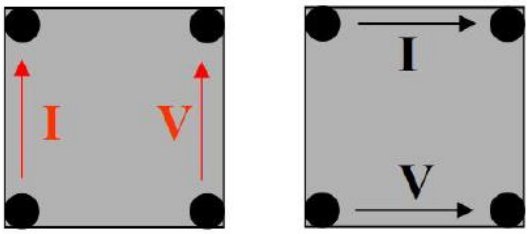

Figure II-7 *Schematic representation of Van der Pauw contacts configuration*

The samples resistivity has been estimated as:

$$\rho(T) = R_{sh} \cdot t \qquad \text{II-1}$$

Where R_{sh} is the sheet resistance and t is the sample thickness obtained by XRR measurements.

The manganites based QWs have been measured at UNISA in a temperature range from 320K to 10K using a cryocooler cold finger type. This system is a refrigeration closed cycle based on the Gifford-McMahon thermodynamic cycle. Thanks to this cycle, the heat is removed from the cold finger by two phases of Helium gas expansion. The cold finger consists in two cooling stages and the temperature stabilization is regulated by a feedback system composed by a thermometer and a heater. All the system is kept in vacuum (~10^{-4} Torr).

The cuprate based QWs have been measured at Cornell University using a dipper in liquid Helium, so the measurements have been performed in the temperature range from 300 K to 3.9 K.

II.3 Advanced electron spectroscopy

II.3.1 X-ray Absorption Spectroscopy (XAS)

The X-ray Absorption Spectroscopy (XAS) is a widely used technique for determining the local geometric and/or electronic structure of matter. XAS is a type of absorption spectroscopy from a core initial state with a well-defined symmetry therefore the quantum mechanical selection rules select the symmetry of the final states in the continuum which usually are mixture of multiple components.

A schematic representation of XAS mechanism is shown Figure II-8, where a core electron is excited to an unoccupied state above the Fermi level by the incident radiation to the conduction band. The required (absorbed) energy E_{abs} is

$$E_{abs} = h\nu = E_{fin} - E_{in}$$

where E_{fin} is the energy of the final state (the core electron excited into the conduction band) and E_{in} is the energy of the initial state (the not excited electron).

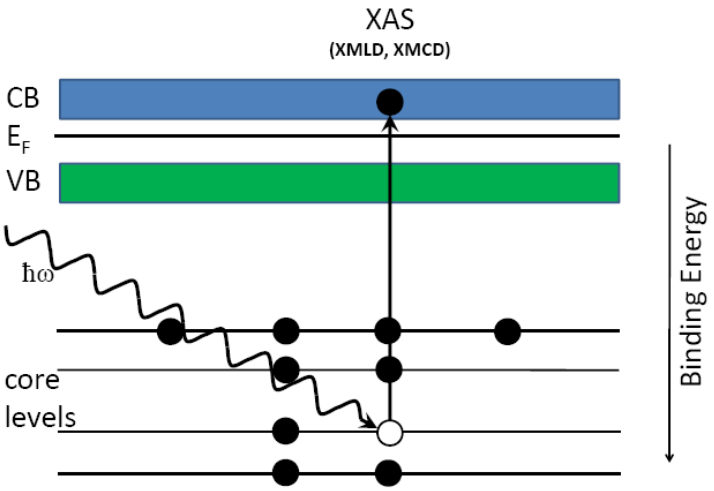

Figure II-8 *Schematic representation of XAS mechanism. CB and VB are the conduction and the valence band respectively and E_F is the Fermi energy*

The transitions that occur in the process are due to the dipole selection rules that change the angular momentum quantum number l by one ($\Delta l = \pm 1$). While the spin s is conserved ($\Delta s = 0$), the z-component of the orbital momentum m has to change by zero or one ($\Delta m = \pm 1; 0$). In particular, the left and right hand circular polarized light change $\Delta m = \pm 1$ and linear polarized light doesn't change m ($\Delta m = 0$). There are also quadrupole transitions, that allows $\Delta l = \pm 2; 0$, but they are hundred times weaker than the dipole ones.

The transitions that contribute to XAS edges are shown in Figure II-9. The edges depend upon which core electron is excited, in fact the principal quantum numbers $n = 1; 2; 3$ correspond to the *K*-, *L*- and *M*-edges respectively. For example, the excitation of a *1s* electron occurs at the *K*-edge, or excitation of *2s* or *2p* electron occurs at an *L*-edge.

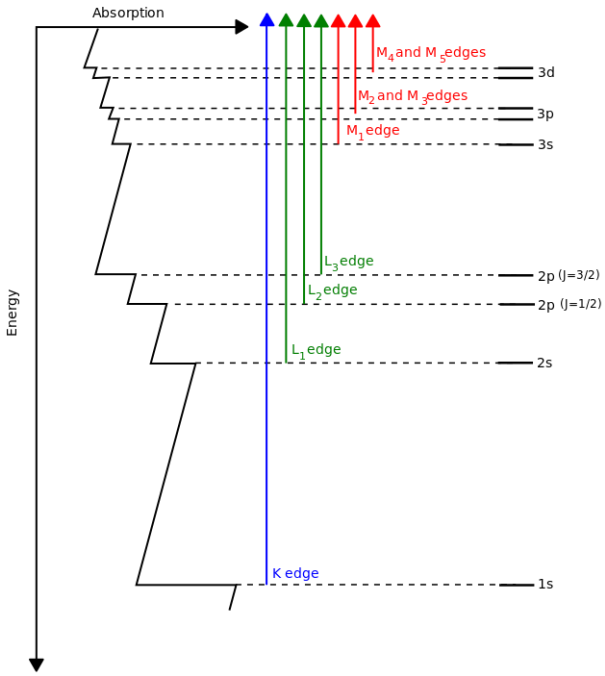

Figure II-9 *Transitions that contribute to XAS edges*

The unoccupied density of states is probed with XAS, indeed the electrons are excited from a specific core level to the unoccupied states and, because of each element has individual excitation energies for its level, only one atom is excited.

A tunable source, such as the radiation of synchrotron, is needed to determine different states in the conduction band, as shown in Figure II-10, for example, to probe the Cu states. Indeed, the synchrotron radiation can be tuned to the characteristic Cu energy and changing the light polarization it is possible to select transitions to in-plane and nearly out-of-plane Cu 3*d* states.

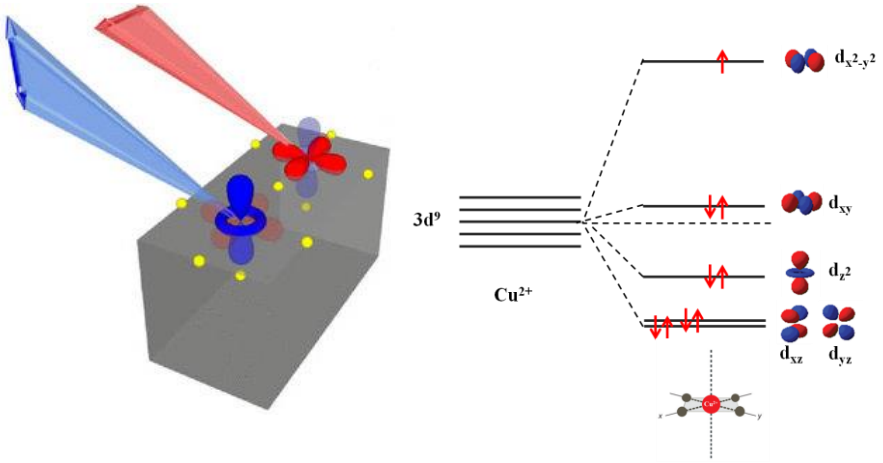

Figure II-10 *Cu 3d states probed by XAS radiation. Left: schematic representation of horizontal (red) and vertical (blue) light polarization used to probe in-plane and ou-of-plane states; right: electronic configuration of 3d states of ion* Cu^{2+}

The absorption can be calculated measuring the remaining intensity in transmission or reflection experiments. For the metals, the drain current from the sample, that is proportional to the XAS signal, can be measured and this is called total electron yield (TEY). Conversely, if the sample is an insulator, the intensity of radiant recombination can be measured and this is called partial or total fluorescence yield (PFY or TFY) mode.

An example of XAS spectra for Mn with different oxidation state, and thus the different number of valence electrons, is shown in Figure II-11 (Gilbert et al., (2003)).

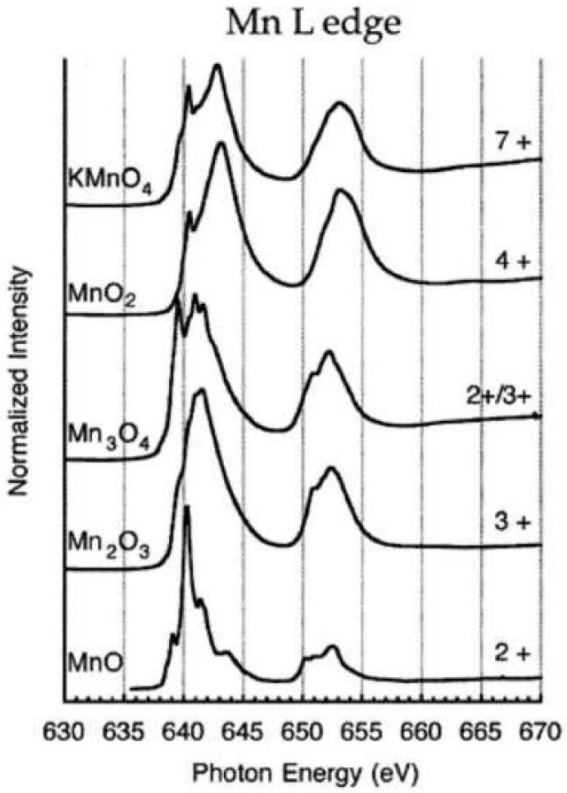

Figure II-11 *Multiplet structure for different oxidation state of Mn (Gilbert et al., (2003))*

II.3.2 X-ray Magnetic Circular Dichroism (XMCD)

X-ray Magnetic Circular Dichroism (XMCD) is a difference spectrum of two XAS spectra taken in a magnetic field, one taken with left circularly polarized light, and one with right circularly polarized light. By closely analyzing the difference in the XMCD spectrum, information can be obtained on the magnetic properties of the atom, such as its spin and orbital magnetic moment. Indeed, using XMCD it can be possible to analyze the magnetic moments element specifically and moreover separated into their spin and orbital moments. XMCD is used for the characterization of magnetic materials.

The spin dependent dichroism in the absorption process, that gives the XMCD effect, corresponds to the difference between the number of spin up and spin down holes of the conduction band, which gives the magnetic moment.

The maximum XMCD signal is obtained when the photon angular momentum is collinear to the magnetization direction *M*. The dichroism is than given by the difference spectra measured with the right-hand and left-hand polarized light.

The absorption of circularly polarized x-ray photons leads to a spin polarization of the photoelectrons due to spin-orbit coupling ($j = l \pm s$). In particular, at the L_3 edge ($j = l + s$), left-hand circular polarized light mainly probe the unoccupied spin up *d* states with respect to the direction of magnetization. The opposite sign of spin-orbit coupling ($j = l - s$) inverts the effect at L_2 edge.

Thole et al. and then Chen et al. found the so called XMCD sum rules to calculate the magnetic moments for $2p \rightarrow 3d$ transitions (Carra et al., (1993); Chen et al., (1995); Thole et al., (1992)).

II.3.3 X-ray Linear Dichroism (XLD) and X-ray Magnetic Linear Dichroism (XMLD)

The X-ray absorption of linear polarized light changes with the geometry of the experiment that gives a dichroic signal for different orientations of the light polarization. In the case of natural X-ray Linear Dichroism (XLD), the polarization plane is either perpendicular or parallel to the crystal axis of a not magnetized single crystal; while in the case of the X-ray Magnetic Linear Dichroism (XMLD), the geometry is similar to XLD, but polarization plane is perpendicular or parallel to the magnetization of the sample.

With XLD technique, the orbital ordering can be observed. Indeed, the transition intensity of the absorption process is proportional to the number of empty valence stats in the direction of the electric field vector ***E***, so the orbitals lying perpendicular to the electric field vector are not excited and for spherical orbitals, no natural XLD appears. For example, the splitted *3d* states (e_g and t_{2g}) of an octahedral crystal field are spherical, but if the *d* orbitals are differently occupied, a natural dichroism appears.

Typically, the XLD measurements are performed using linearly polarized photons with the electrical vector $\boldsymbol{E}$ either parallel (H polarization) or perpendicular (V polarization) to the synchrotron orbit. At normal incidence $\boldsymbol{E}$ lies in the sample plane for both polarizations, whereas the grazing incidence and H polarization (i.e. 30° from the surface) $\boldsymbol{E}$ is nearly parallel to out-of-plane (c) axis of the samples. In this way, the absorption spectra with $\boldsymbol{E} \perp c$ and $\boldsymbol{E} \parallel c$ and the corresponding XLD can be measured. Usually XLD is defined:

$$XLD = XAS(\boldsymbol{E} \perp c) - XAS(\boldsymbol{E} \parallel c) \propto XAS(V, 30°) - XAS(H, 30°)$$

or equivalently by using *XAS(H,90°)* in place of *XAS(V,30°)*. XLD is sensitive to the axial anisotropy of the electron density of states.
For the XMLD, the sample is magnetized by an external magnetic field and, consequently, the charge density is distorted and elongated along the spin axis.

Chapter III
Results

III.1 Growth and characterization of p-type QWs

During this work, manganites have been grown at UNISA in order to investigate the properties of *p*-type QWs (Galdi et al., (2017)). In the past years many experimental and theoretical studies have been dedicate to manganites (Jin et al., (1994); von Helmolt et al., (1993)) because of the interest raised by the variety of magnetic and electric phenomena, such as ferromagnetism, antiferromagnetism, charge ordering, and so on. LSMO single layers have been widely investigated in the past years (Adamo et al., (2009a); Barone et al., (2007a); Maritato et al., (2006); Mercone et al., (2005); Orgiani et al., (2007a), (2006); Petrov et al., (2004)), and in this work the attention is paid to LSMO based heterostructures.

Many perovskite oxides are Mott insulators, with small energy band gap, and the first question to answer in view of the fabrication of oxide-based QWs is about the ability to obtain quantum confinement by using them as the insulating material. To answer this question, we have grown SMO/LSMO/SMO QWs using the RHEED calibrated shuttered layer-by-layer MBE deposition process, as described in Section II.1, and studied the structural and electrical transport properties of the QWs with different SMO and LSMO relative thicknesses.

As introduced in Section I.4.1, the SMO is an antiferromagnetic Mott insulator with a gap value of about 0.35 eV (Søndenå et al., (2006)) and

LSMO is a well-known ferromagnetic metallic *p*-type compound, with Curie temperature values around 350 K, associated to a Metal-Insulator transition responsible of the Colossal Magneto-Resistance (CMR) behavior (Coey et al., (1999)). The Curie temperature along with the Metal-Insulator transition temperature T_{MI}, are strongly dependent of many parameters (disorder, strain, composition, etc.) and can be used as an additional check for evaluating the quality of the produced samples.

The obtained results show that at low temperatures, quantum confinement is observed when the LSMO thickness is smaller than about 5 unit cells (u.c.), even for SMO thickness as small as 15 u.c.

These observations, following those already presented by Li et al. in $LaVO_3/SrVO_3/LaVO_3$ heterostructures described in Section I.2.4 (Li et al., (2015)), open the way to the fabrication and study of oxide based quantum wells in which the insulating material can be a "Mott" insulator, implementing the already ample range of possible oxide heterostructures where to investigate for new quantum effects.

The SMO/LSMO/SMO QWs growth has been performed both in O_2 and O_2+10%O_3 mixture pressure of 1×10^{-6} Torr. The films were deposited on NdGaO3 (110) (NGO) substrates, which have distorted perovskite structure with an orthorhombic symmetry and a pseudo-cubic lattice constant of 0.3854 nm, and on $SrTiO_3$ (100) (STO) with lattice parameter 0.391 nm. In the first case the SMO layer is subject to tensile stain on NGO, while the LSMO is subject to compressive stain; in the latter case, both the LSMO layer and the SMO layer are subject to tensile strain on STO.

During the growth the substrate temperature, measured by a thermocouple, was 720°C. This temperature was chosen as the best compromise to obtain good quality SMO and LSMO single films on the chosen substrates. At the end of the growth, the samples were cooled to room temperature in deposition atmosphere: this is crucial to avoid sample deoxygenation. The La, Sr and Mn shutter opening times were calibrated by monitoring intensity oscillations of the RHEED pattern (as explained in Section II.1) during the growth of $LaMnO_3$ (LMO) and SMO films. The RHEED patterns were observed setting the electron beam parallel to one of the in-plane [110] azimuths of the substrate. In order to check the thickness of these calibration-check films (LMO and SMO), the values of the SMO and LMO *c*-axis lattice (out-of-plane lattice parameter) constant and that of the total film thickness, respectively measured by XRD and XRR analysis (as explained Section II.2.1), was used to compare the number of shuttering periods to that of the actual number of unit cells present along the growth

direction in our calibration samples. The equality between these two values is indicative of perfectly alternating complete Sr-O (La-O) and Mn-O monolayers. An example of RHEED oscillations for LMO and SMO calibration is reported in Figure III-1.

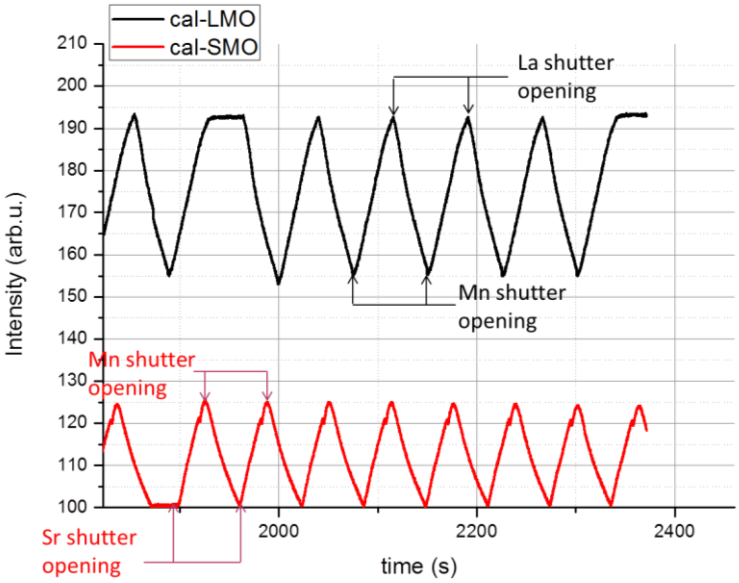

Figure III-1 *Layer-by-layer RHEED calibration of LMO and SMO single layers. Sr, La, Mn respective shutters opening is highlighted.*

After the calibration of LMO and SMO, the growth of LSMO is achieved by opening the La shutter for the 70% of the calibrated time, and simultaneously opening the Sr shutter for the 30% of the calibrated shutter time.

A typical RHEED pattern at the end of the growth of a SMO/LSMO/SMO QW sample grown on STO substrate is shown in Figure III-2.

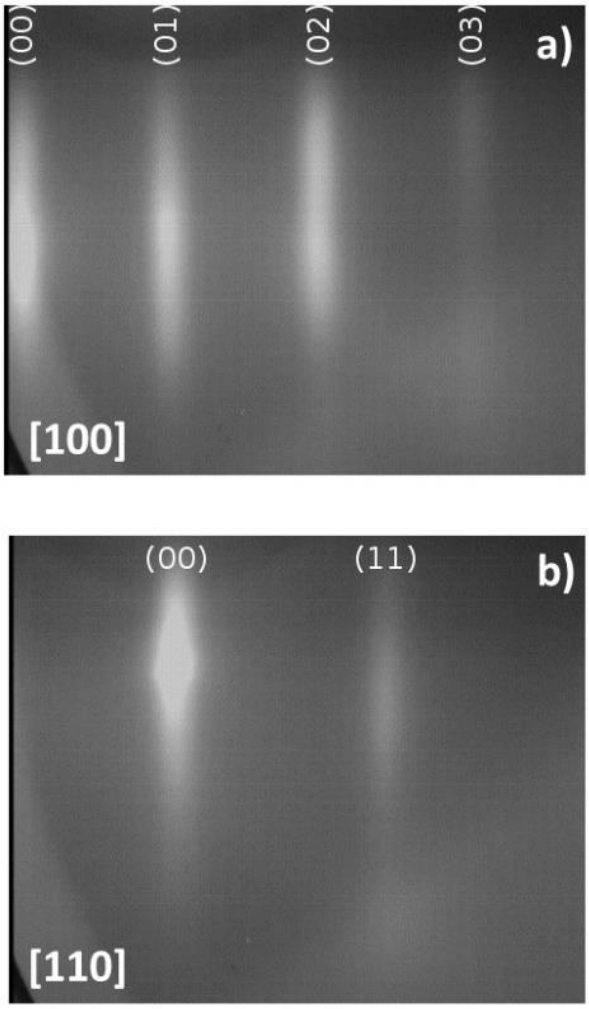

Figure III-2 *Typical RHEED pattern of an epitaxial SMO/LSMO/SMO QW viewed along the [100] azimuth a) and along the [110] azimuth b). Both images are acquired at the end of the growth*

The $(SMO)_x/(LSMO)_y/(SMO)_z$ QWs (the subscripts refers to the number of u.c. of respective layer) have been grown fixing the thicknesses of two of three layers and changing systematically the third. In particular, the top and the bottom insulating SMO layers' thicknesses were fixed, while the thickness *y* of the central "active" LSMO layer was systematically changed;

then only the thickness of the top most SMO layer (*z*) was varied to further check its influence on the electrical transport properties.

III.1.1 Structural characterization

Structural characterization has been performed in order to check the quality of the samples, so the structural properties of the samples were characterized by means of XRR and XRD, as described in Section II.2.1.

XRR and XRD measurements have been also used to obtain the actual number of grown unit cells and the lattice parameters of single SMO and LSMO calibration thin films.

In particular, XRR measurements give information about the thickness of the layers in the hetero-structure and on the interface roughness, as described in Section II.2.1.2.

The XRRs and XRDs for the QWs grown on NGO and STO are shown in Figure III-3.

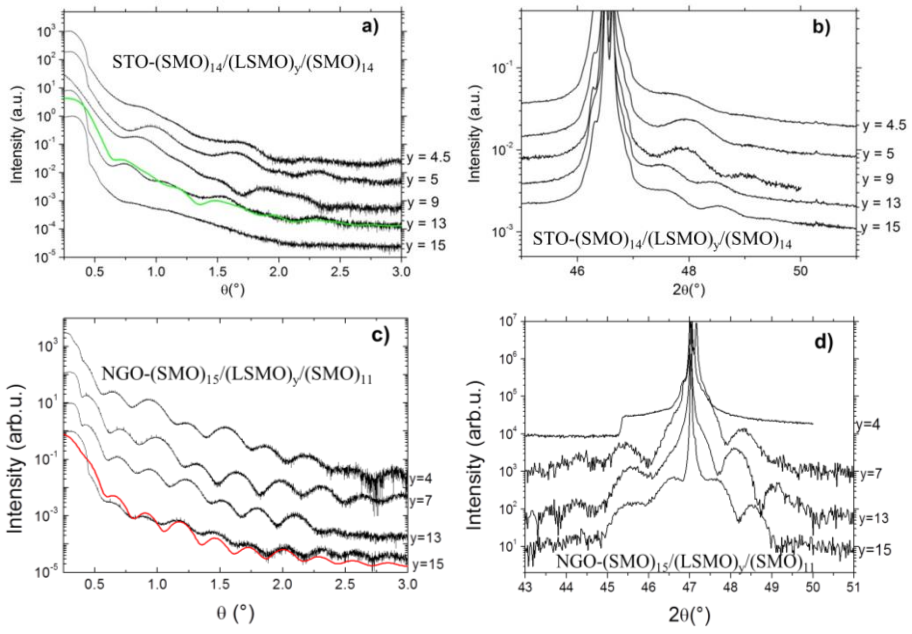

Figure III-3 *Structural characterization of SMO/LSMO/SMO QWs in function of the central layer thickness. Curves are shifted for clarity. a) XRR*

spectra of QWs grown on STO substrate where the top and the bottom SMO insulating layers' thicknesses are fixed symmetrically at 14u.c. while y=15, 13, 9, 5, 4; for one of the curves a fit of the reflectivity is shown (thick green line). b) XRD spectra of the same samples shown in a). c) XRR spectra od QWs grown on NGO substrate where the top and the bottom SMO insulating layers' thicknesses are respectively fixed at 15 and 11u.c., while y = 15, 13, 7, 4; for one of the curves a fit of the reflectivity is shown (thick red line). d) XRD spectra of the same samples shown in c)

The XRR data were fitted using as fitting parameters the layers' thickness, density and roughness. In both sample sets (grown on NGO and STO) the XRR spectra are visible up to $\theta = 3°$ demonstrating the low roughness of the surfaces and interfaces. For the interface roughness an error function profile was used; the standard deviation σ returned by the fitting routine is about 1 unit cell ($\approx$ 0.4 nm) for all the samples. The strong modulation of the thickness fringes is due to the different layers' density.

In the XRD spectra shown for both sets of samples, the peaks observed at angles higher than the substrate ones are related to the trilayered structure. The measured spectra result from the coherent addition of the contribution of each layer of the heterostructure, giving rise to interference pattern between top and bottom SMO layers and to Laue fringes. These patterns can be reproduced by fitting the XRD data (GlobalFit - Rigaku). From these fits the values obtained for the thicknesses of the SMO and LSMO layers are in very good agreement with those calculated by the XRR. In Figure III-4, the XRD fits of the samples with y= 15, 13, 7 shown in Figure III-3 d), are reported for comparison with their twin samples grown on STO substrates in the same deposition run. As a reference, the fit of a single layer SMO grown on STO and NGO is also shown.

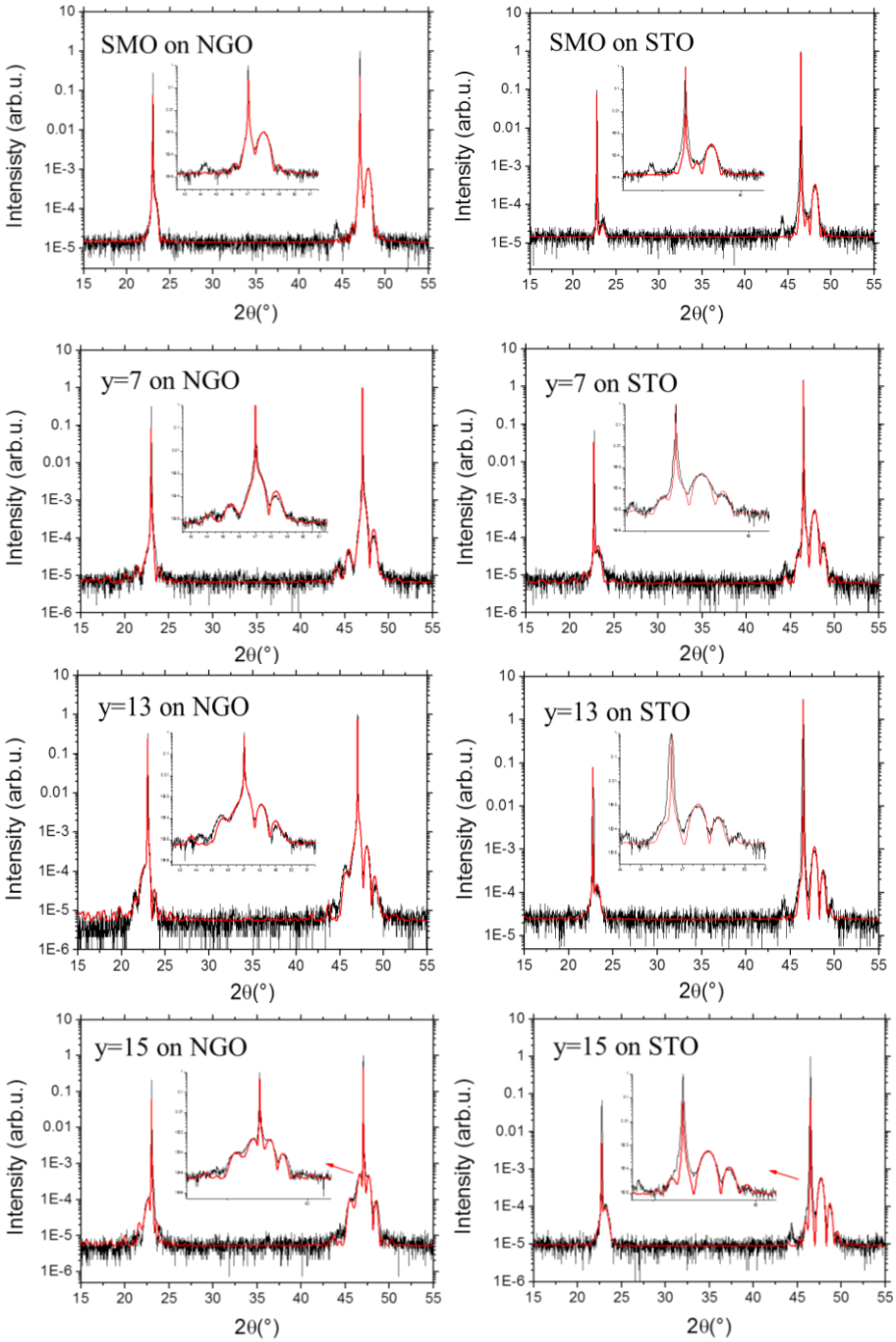

Figure III-4 *XRD fit of the samples with y= 15, 13, 7 shown in Figure III-3 d), in comparison with the their tween samples grown on STO substrates in*

the same deposition run. SMO single layers on STO and on NGO are also reported. Zooms of (002) reflection are shown in insets.

All these XRD spectra reveal ordered structures and confirm the thickness and the lattice parameters as well.

QWs as a function of the top-most SMO layer's thickness have also been analyzed. In Figure III-5 XRR and XRD spectra are shown.

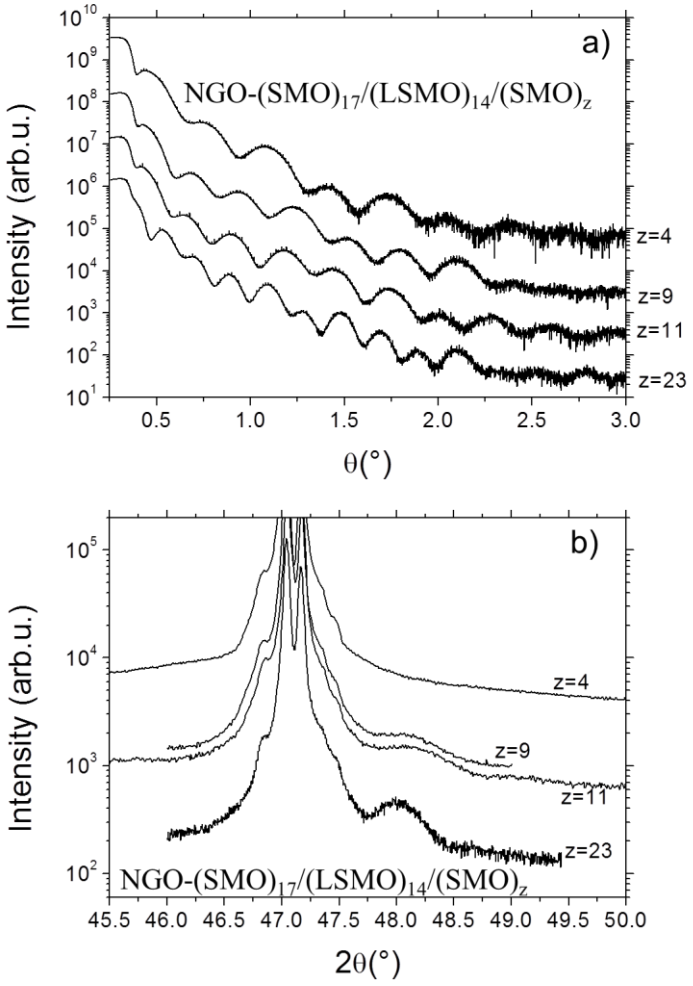

Figure III-5 *Structural characterization of SMO/LSMO/SMO QWs in function of the topmost SMO layer's thickness. Curves are shifted for clarity. a) XRR spectra of QWs grown on NGO substrate where the insulating SMO bottom layer and the central LSMO metallic layer thicknesses are fixed respectively at 17u.c. and 14u.c. while z=23, 11, 9, 4; b) XRD spectra of the same samples shown in a)*

Also for these samples, XRR spectra have been fitted using thickness, roughness and density as fitting parameters. The low roughness of the surfaces and interfaces (the standard deviation σ returned by the fitting routine is about 1 unit cell (≈ 0.4 nm) for all the samples) is also confirmed.

The strong modulation of the thickness fringes is due to the different layers' density. XRD spectra reveals ordered structures.

III.1.2 Electrical transport characterization

In order to analyze the electrical transport properties of the QWs, sheet resistance measurements have been performed as a function of the temperature using a Van der Pauw four-probe geometry (Figure II-7) with Indium soldered contacts. To reduce contamination of the samples any patterning process was avoided. To check the insulating behavior of the top most SMO layer, two-probe Silver paint contacts were added on the surface of the samples. The presence of abrupt structural transitions between the central conducting layer and the two SMO layers does not ensure by itself the confinement of the charge and, in principle, the carriers could spread well beyond the thickness of the LSMO layer. Two-probe low temperature resistance values of the SMO top most layer was always well above 200 kΩ. The sample set as a function of the SMO top most thickness ($(SMO)_{17}/(LSMO)_{14}/(SMO)_z$) have been grown with the aim of investigating its influence on the electrical transport properties. The samples with $z > 10$ showed low temperature resistivity and metal-insulator temperature (T_{MI}) values comparable to those observed in the bulk material, while the samples with $z < 10$, showed reduced T_{MI} and higher low temperature resistivity values with the presence of minima and up-turns (Figure III-6).

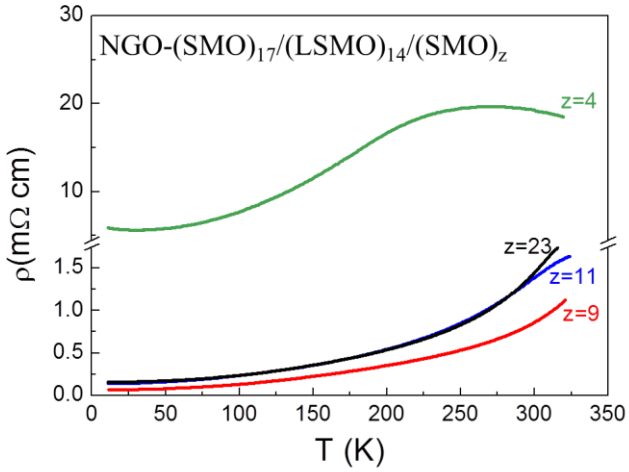

Figure III-6 *Resistivity versus temperature curves of QWs with different topmost SMO layer thickness z in unit cells*

Resistivity (or sheet resistance), the metal-to-insulator transition and the presence of resistivity upturns at low temperature can be used as a diagnostic.

If the carriers are confined in the LSMO layer, an influence from the top layer thickness is not expected.

While for $z \geq 9$ the resistivity curves have similar values and behaves as a function of temperature, for $z = 4$ there is a change in resistivity curve that may be linked to the diffusion of carriers in the SMO layer. Indeed, the transport properties behavior observed in Figure III-6 can be explained only assuming that the carriers of the LSMO, even at room temperature, penetrate into the SMO top most layer only over distances shorter than 10 unit cells; obviously, such a distance can be influenced by the SMO/LSMO interface properties (band alignment, atomic intermixing, roughness) and SMO/vacuum interface properties. Theoretical calculations on LMO/SMO interfaces, limit the charge redistribution across the interfaces to around three unit cells (Aruta et al., (2009a); Nanda and Satpathy, (2009)). The value we have observed (around 9 unit cells) is not far from the theoretical prediction.

In order to investigate the properties of the samples set in function of the central LSMO thickness, the SMO top-layers has been chosen to be always thicker than 10 u.c., so the transport properties were not limited by the SMO thickness layer.

Using eq. II-1, the resistivity ρ of the LSMO layer has been estimated, where t is the thickness of the LSMO layer obtained by XRR fits. All the samples, except the one with y = 1.5 (not shown in figure), showed a room temperature resistivity ρ_{RT} in the range 2-9 mΩcm.

In Table III-1, the main structural and transport parameters for the QWs investigated as a function of the central layer thickness (y) are summarized. In the table, T_{min} is defined as the temperature at which a local minimum is observed in some of the samples.

Table III-1 *Properties of the investigated QWs with different LSMO layer thickness y*

y (u.c.)	***T_{MI} (K)***	***T_{min} (K)***	***ρ_{RT} (mΩcm)***	***ρ(300K)/ρ(77K)***
15.5	337	-	5.9	7.46
15	327	-	4.1	8.85
13	333	22	6.5	4.72
10	324	32	6.1	3.89
9	308	25	4.6	7.43
6.5	305	21	6.4	5.53
5	290	181	6.5	0.86

In Figure III-7 the resistivity measurements (normalized at room temperature resistivity - $\rho(T)/\rho_{RT}$) as a function of the temperature and of the thickness of LSMO central layer are shown.

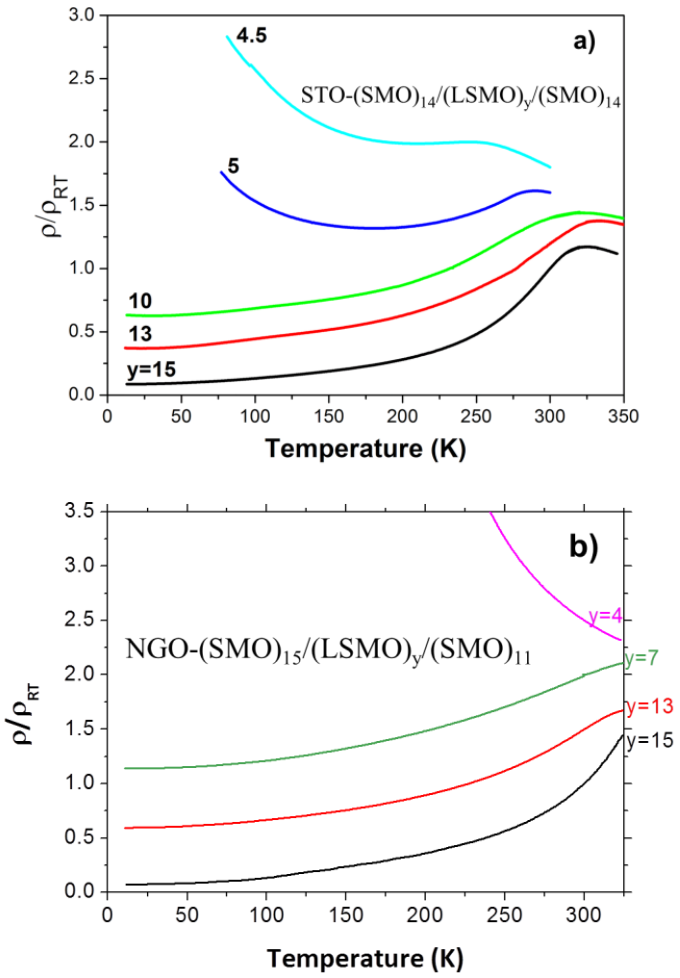

Figure III-7 *Resistivity versus temperature curves normalized to room temperature, 300K, of QWs samples grown on STO (a) and on NGO (b) with different LSMO layer thickness y in unit cells; the curves are vertically shifted by a constant offset factor for clarity.*

All the samples investigated (grown on NGO and STO) showed a T_{MI} with values dependent on *y*, except the one with *y* = 1.5 (not shown in figure). For the samples on STO with *y* = 15, 13, 10 and for the samples on NGO with *y* = 15, 13, 7 the T_{MI} values are comparable to those of bulk material. At lower *y*, the T_{MI} starts to decrease until a value around 250 K is reached for the sample with y = 4.5 on STO. The sample with *y* = 4 grown

on NGO is fully insulating. At lower temperatures, the resistivity curves present a shallow minimum at temperatures T_{min} around 20-30 K, while they have a rapid upturn at temperature below 150 K for y = 5, 4.5.

The behavior of T_{MI} vs. y observed in all the QWs grown is shown in Figure III-8 a). Even for y = 5, the sample presents a T_{MI} value above 240 K, confirming that the charge carriers are indeed spatially confined in the LSMO layer.

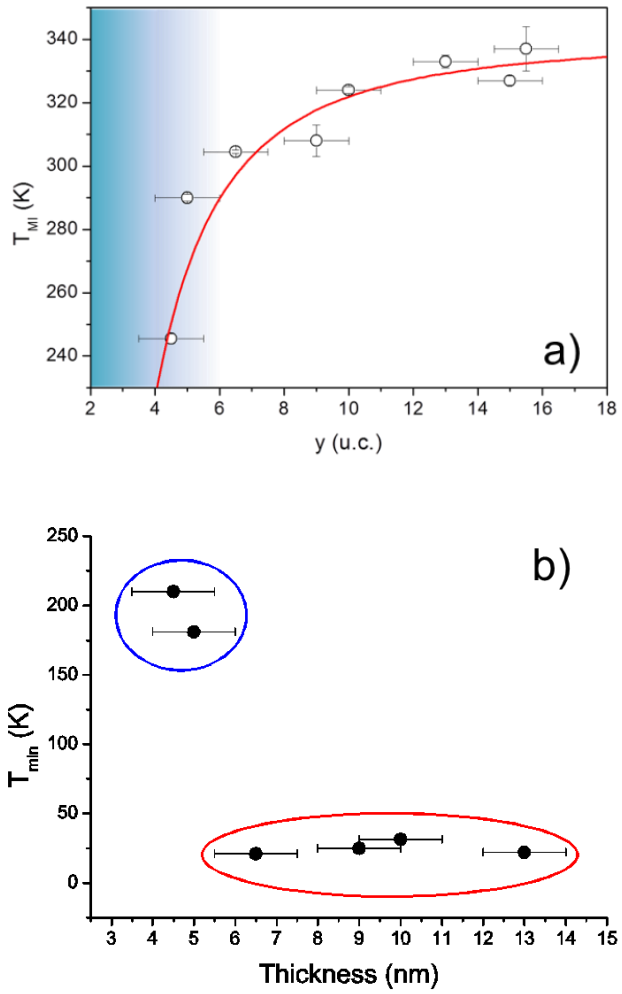

Figure III-8 *a)Metal to insulator transition temperature T_{MI} as a function of LSMO layer thickness y. The shadowed region indicates the thickness at*

which insulating behavior emerges at low temperature. b) resistivity minimum temperature as a function of LSMO layer thickness y. Two different regimes are clearly observed for samples with $y > 5$ and $y \leq 5$. The data points are grouped dependently on minimum position: red line for minima occurring below 50K and blue line for minima occurring above 150K

In fact, if the carriers were spread out all over the QW thickness, the effective doping of the system should strongly decrease with decreasing y, reaching values where the metallic behavior is no longer expected and the T_{MI} values should fall well below 150 K (Coey et al., (1999)). Moreover, the sudden drop in T_{MI} observed for $y < 8$ could be related to the reduced dimensionality of the system induced by the layering. In terms of the Ginzburg-Landau approach, valid for a second type phase transition such as the ferromagnetic one, to which the T_{MI} value is linked, we expect, in the case of a system with finite size t along one direction, a behavior given by the following equation

$$T_{MI}(t) = T_{MI_0}\left(1 - \left(\frac{L_0}{t}\right)^2\right) \qquad \textit{III-1}$$

where T_{MI0} is the bulk Metal-to-Insulator transition and L_0 is the critical thickness below which the phase transition is no longer present. The red curve in Figure III-8 a), is the best fit to the data using eq. III-1 with $T_{MI0} = (340 \pm 6)$ K and $L_0 = (2.3 \pm 0.1)$ u.c.. The T_{MI0} value is close to what observed in bulk LSMO, while the L_0 value is in good agreement with the theoretical calculation in the case of SMO/LMO interfaces (Aruta et al., (2009a); Nanda and Satpathy, (2009)). This is in agreement also with the observation that the $y = 1.5$ sample was highly insulating.

In Figure III-8 b), the temperature values at which a minimum in the trilayers low temperature resistivity appears are shown. The circles in the figure point out two different temperature range at which the minimum occurs. The red circle groups QWs with a shallow minimum appearing below 50 K, while in the blue one are the samples with a strong up-turn appearing above 150 K. The behavior observed for the points in the red circle can be associated to an increased confinement of charge carriers with decreased LSMO thickness. Such effects have been already observed in manganite thin films (Gao et al., (2012); Mukhopadhyay and Das, (2009); Wang et al., (2014)) and recently have been unambiguously related, in LSMO ultrathin films (Niu et al., (2016)), to quantum interference effects (QIE). The low temperature resistivity curves of the QWs in the red circle,

are well described in terms of both the three- and two-dimensional QIE (Maritato et al., (2006)), hindering the possibility to determine the effective dimensionality of the systems and the main scattering process at work. The temperature range at which the low temperature resistivity minima are observed is the one expected when the charge carrier properties starts to be limited by weak localization, probably induced, in the QWs case, by the layering. The data in the blue circle are associated to temperatures which are not compatible with a layer induced quantum interference effect and are more probably related to an increased role played by disorder when the thicknesses of the conducting system are reduced. We note that, the relevant length scale for the paramagnetic-ferromagnetic transition is the magnetic correlation length while those important for the QIE are the electronic mean free path and the inelastic scattering dephasing length (Lee and Ramakrishnan, (1985)).

III.1.3 Preliminary results of advanced spectroscopy measurements on p-type QWs

X-ray Absorption Spectroscopy (XAS), X-ray Linear Dichroism (XLD) and X-ray Magnetic Circular Dichroism (XMCD) advanced spectroscopy measurements have been performed in two important experiments at Elettra Synchrotron Light Source in Trieste, Italy, and at Diamond Synchrotron Light Source in Didcot, UK.

III.1.3.1 Localization and orbital order in SMO/LSMO/SMO quantum wells

This experiment was performed at Advanced Photoelectric Effect (APE) beamline at Elettra Synchrotron Light Source in Trieste, Italy. APE beamline offers the suitable flexibility in experimental geometry and light polarization. In this beamline, there is the possibility to have access to a series of surface characterization and preparation tools. The procedures adopted at APE, combined with the possibility of *in-situ* surface preparation and characterization, warrant accuracy useful for experiments (Panaccione et al., (2009)).

The aim of the experiment is to gain information on the carrier localization in SMO/LSMO/SMO QWs grown on NGO. The Mn valence as a function of the XAS probing depth in the heterostructures with different LSMO layer thickness has been studied and the probing depth in heterostructures with different SMO topmost layer thickness has been tested. Linearly polarized radiation can determine the preferential orbital occupation of the LSMO and SMO layers in order to determine the physics of carrier localization: metallic mixed manganites (e.g. in LSMO, Mn acquires mixed $Mn^{3+/}Mn^{4+}$ valence) are characterized by orbital disorder, while insulating (e.g. in SMO, Mn valence is Mn^{4+}) ones have more marked orbital polarization of the Mn 3d states. Orbital polarization can be induced by epitaxial strain, by interface effects or by electronic correlations (Stemmer and Millis, (2013)).

XAS, XLD and XMCD measurement at Mn edge on the SMO/LSMO/SMO trilayers at room and low temperature (100K) were performed. The most part of XAS measurement were performed in grazing incidence (30°) by changing the radiation polarization from vertical (V) to horizontal (H). For XMCD measurements a field of 500 Oe in pulsed mode was usually applied. In some samples this field wasn't large enough to see any magnetic effect at 100K.

Sum XAS spectra (given by the sum of vertical and horizontal signals) are shown in Figure III-9. In particular, in the top panel the sum XAS measurement of LSMO and SMO single layers are shown as a reference; in the bottom panel isotropic XAS measurements of the QWs as a function of the topmost SMO insulating layers are a combination of the two single layers. Indeed, the spectrum with the thickest SMO topmost layer (z = 23) is more similar to the SMO spectra, that is typical of Mn^{4+} (Gilbert et al., (2003)); while the sample with thinnest topmost layer (z = 4) is more similar to LSMO single layer spectra, that is typical of mixed valence $Mn^{3+/4+}$.

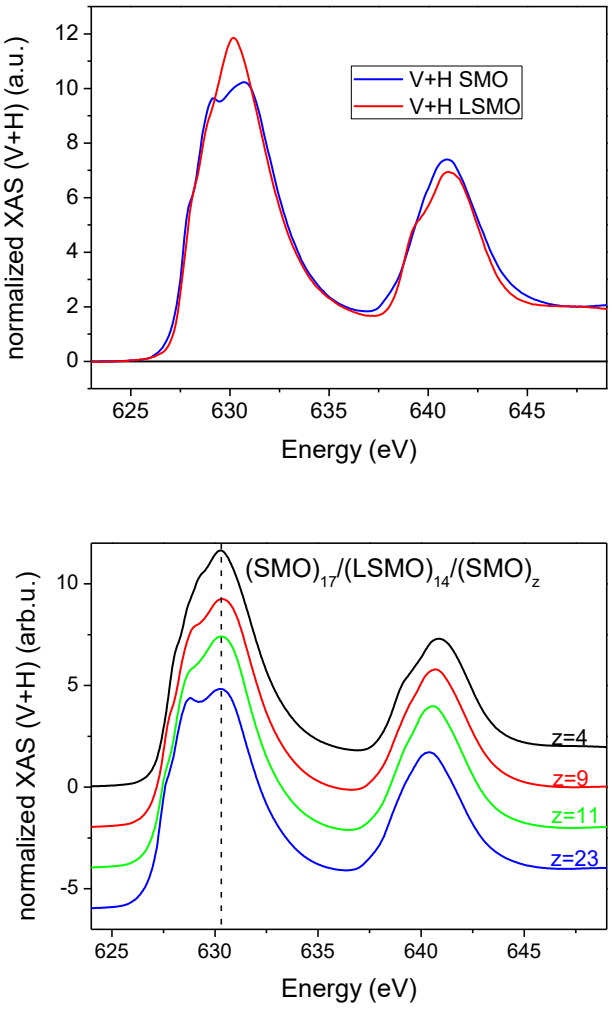

Figure III-9 *Top panel: sum XAS spectra of single layers of LSMO and SMO; bottom panel: sum XAS spectra of the QWs as a function of the topmost SMO insulating layer z*

The measurements performed are useful to obtain information on the orbital occupation of the samples as a function of the probing depth and as a function of the LSMO layer thickness, according to the aimed goal of the experiment. Some complementary information on the ferromagnetic order is also obtained by the XMCD measurements, showing that the LSMO is

ferromagnetic up to the lower investigated thickness (4 u.c.), revealing that the magnetic anisotropy can be tuned by the thickness of LSMO central layer.

III.1.3.2 Competition between ferromagnetism and antiferromagnetism in SMO/LSMO/SMO heterostructures: towards magnetic oxides quantum wells

This experiment was performed at I10 – Beamline for Advanced Dichroism Experiments (BLADE) at Diamond Synchrotron Light Source in Didcot, UK. This beamline can be used to study the magnetization and the magnetic structure of novel nanostructured systems. These magnetic properties can be probed thanks to high dichroic effects, that can be studied in absorption and scattering experiments. Indeed, I10 - BLADE beamline is composed by two branches: a scattering and an absorption branch. In particular, on the former, there is a soft X-ray diffractometer (RASOR) which consists in of a three-circle diffractometer with a polarization analyzer and the samples can be cooled down to 12 K (Beale et al., (2010)); on the latter, a high field magnet (14T along the incident beam direction) can be used for performing magnetic dichroism experiments and the samples can be cooled by variable temperature insert down to 3K.

The aim of the experiment is the study of magnetic degrees of freedom in electrostatically defined heterostructures, such as SMO/LSMO/SMO QWs grown on NGO where the ferromagnetic (F) LSMO is embedded in antiferromagnetic (AF) SMO layers. The carriers are electrostatically confined in the LSMO and metallic properties and ferromagnetism-driven metal to insulator transition is observed down to 4 unit cell thick LSMO (in the previous experiment). Our measurement of XMCD at Mn $L_{2,3}$ edge reveal that the magnetic anisotropy can be indeed tuned by the thickness of the LSMO layer. Its relationship with the antiferromagnetic moment in SMO is investigated via magnetic linear dichroism measurements. An important issue is the magnetization profile across the heterostructure's thickness. This is also investigated via resonant soft x-ray scattering (RSXS) measurements.

RSXS, which combines X-rays scattering with X-rays absorption spectroscopy, is an important element, site and valence specific probe to study spatial modulation of charge, spin and orbital degree of freedom in the investigated materials. In particular, this method is an important tool to examine electronic ordering phenomena in thin films and to zoom into

electronic properties emerging at buried interfaces in artificial heterostructures (Fink et al., (2013)).

The samples have been measured in a high field magnet end station, where XMCD, XLD and hysteresis cycles were measured up to a field of 5T at Mn $L_{2,3}$ edge (E = [630, 670] eV). The sample temperature was varied from 20 K to 250 K and finally to 360 K. The temperatures were chosen in order to be below and above the magnetic transition temperatures of SMO ($T_{Néel}$ = 230K) and LSMO (T_{Curie} = 360K). The incidence angle of the radiation was varied from normal incidence to 80° for grazing incidence measurements.

Magnetic RSXS at two temperatures (100K and 250K) were performed in the soft x-ray diffractometer (RASOR) with E=641 eV (maximum of XMCD) and off resonance (E = 636 eV) for the samples with y = 4u.c. and y = 15 u.c.. A field of 0.4 T was applied in the sample plane thanks to permanent magnets.

In Figure III-10 it is reported the ratio of the maximum of XMCD in grazing and in normal incidence at two different temperatures with an applied field of 2T. The XMCD has been normalized with the maximum of the sum of XAS in the two polarizations in order to compare the measurements.

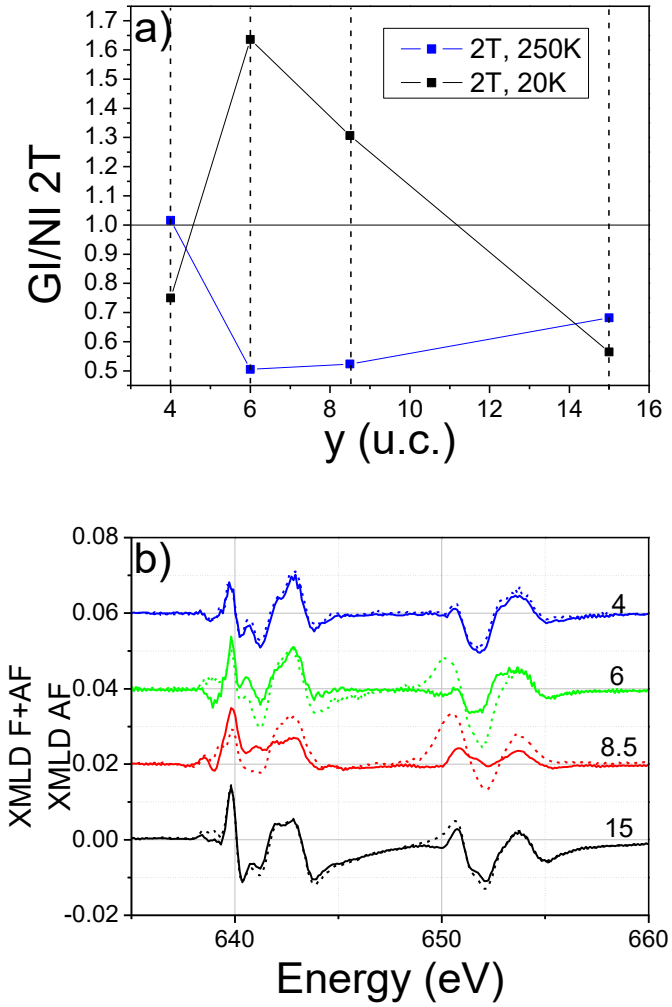

Figure III-10 *a) ratio of XMCD intensity in GI and NI at 20 K and 250 K, with an applied magnetic field of 2T; b) XMLD spectra of the samples with (full lines) and without (dashed lines) the application of magnetic field in the beam direction*

The change in the saturation of ferromagnetic moments below the Néel transition temperature of SMO, observable from these measurements, can be linked to interaction with the antiferromagnetic moments of SMO at the QWs interfaces.

The magnetic contribution to linear dichroism can reveal the orientation of AF moments. In zero field there is the contribution from both F and AF

moments (dashed lines in Figure III-10 b)), while by saturating the F moments in the beam direction, the AF only contribution can be singled out (full in lines Figure III-10 a)) (Aruta et al., (2009b)).

RSXS measurements performed on the y = 15 u.c. sample and on the y = 4 u.c. sample are reported in Figure III-11. The asymmetry between the positive and negative circular polarization measurements is very evident in the both samples.

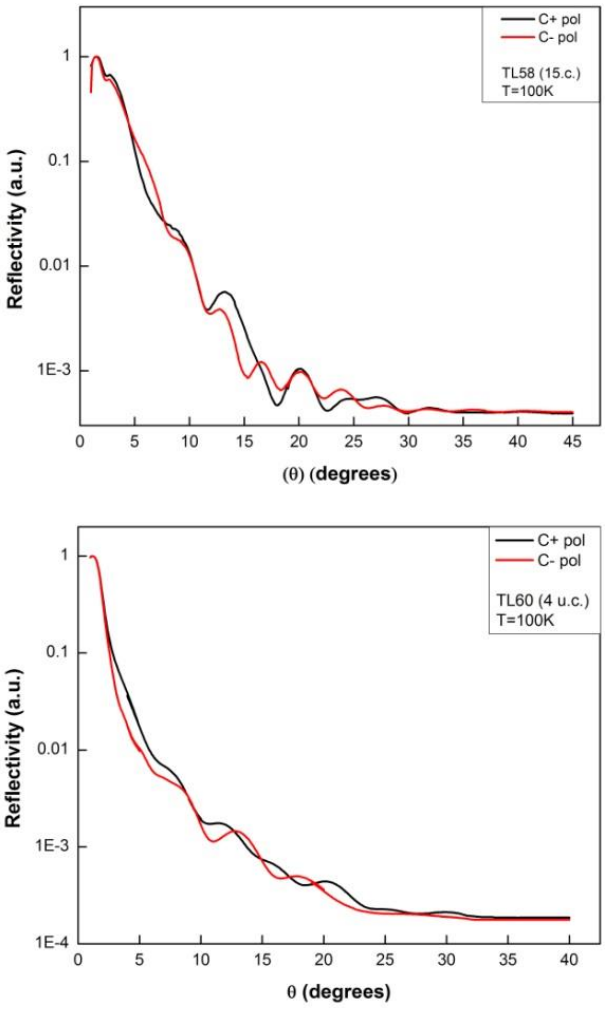

Figure III-11 *RSXS measurements performed on the y=15u.c. e and on the y=4u.c LSMO central layer thicknesses acquired at 100K.*

These measurements give preliminary results and need to be further analyzed, but the data suggest that the interaction between F and AF can lead to modifications of the magnetization properties of the QWs.

III.2 Growth and characterization of n-type QWs

Infinite-layers (IL) electron-doped cuprates based heterostuctures have been grown at Cornell University in order to investigate the properties of n-type QWs. In particular, a conclusive understanding of the normal-state transport properties of electron-doped cuprates is still missing. The study of SLCO and its tetragonal parent compound SCO that, with only one CuO_2 plane per unit cell and the absence of oxygen atoms in the Sr layers, is the simplest undoped parent structures in the cuprate family hosting high-T_C superconductivity, can help to understand the existing puzzling scenario.

In this work $SrCuO_2/Sr_{0.9}La_{0.1}CuO_2/SrCuO_2$ (SCO/SLCO/SCO) QWs have been grown, using RHEED calibrated layer-by-layer O-MBE. The partial substitution in the parent compound SCO of the La^{3+} for the Sr^{2+} gives *n*-type superconductors with critical temperatures up to about 40 K (Armitage et al., (2010); Karimoto and Naito, (2004)).

The structural and electrical transport properties of the fabricated n-type QWs have been investigated as a function of the temperature and for SLCO center layers with varying thickess. As in the case of SMO/LSMO/SMO *p*-doped trilayers described in Section III.1, where we have investigated the thickness dependence of the metal-to-insulator transition temperature as an additional check for evaluating the quality of the produced samples and interfaces, here we have done the same using the superconducting transition temperature. Our electrical transport results exhibit dimensional effects on the normal state of confined SLCO mainly induced by the presence of clean interfaces, giving new hints in the understanding of low dimensional *n*-doped cuprate systems and in the growth of *p-n* doped oxide-based proximate structures.

$(SCO)_{20}/(SLCO)_y/(SCO)_{15}$ QWs (with y = 20,15,10,5,4,3, where y is the thickness of the SLCO in unit cells, u.c.) samples have been grown by a shuttered layer-by-layer deposition process performed in purified O_3 at a background pressure of 3 x 10^{-7} Torr. The films were deposited on (110) $TbScO_3$ (TSO) substrates which have a distorted perovskite structure (pseudo-cubic lattice parameter 0.3958 nm). Both the SLCO and the SCO layers (with bulk in-plane lattice parameters 0.3951 nm and 0.3927 nm respectively) are subject to tensile strain on TSO. During the growth the substrate temperature, measured by a thermocouple, was 500°C. The samples were vacuum annealed in situ (typically around 10^{-8} Torr) at 510°C for 30 min and then they were cooled to room temperature in vacuum. The annealing step and the strong substrate induced tensile strain, avoiding or strongly reducing the presence of apical oxygen in the final samples, are crucial for obtaining superconductivity (Maritato et al., (2013)). The Sr and

Cu shutter opening times were calibrated by monitoring RHEED oscillations during the growth of undoped SCO films in order to obtain RHEED oscillations with constant intensity. The RHEED patterns were observed using a glancing electron beam incident parallel to one of the in-plane $[110]_p$ azimuths of the substrate (*p* subscript indicates pseudo-cubic indices).

After the shutter time calibration, a SCO film was grown to check the actual number of deposited unit cells measuring the total film thickness by XRR and the *c*-axis lattice spacing by XRD analysis to confirm the $Sr_{0.9}La_{0.1}CuO_2$ film composition (Maritato et al., (2013)). The equality between the number of shuttering periods and that of the actual number of unit cells grown is indicative of perfectly alternating complete Sr and CuO_2 monolayers. Finally, the growth of SLCO was achieved by opening the Sr shutter for 90% of the RHEED calibrated time simultaneously with the La shutter for 10% of the time of Sr monolayer. The La flux was determined by a QCM. In order to check the final La content in the grown SLCO film x-rays and XPS analysis have been performed.

The good quality of the deposited heterostructures and the smoothness of their interfaces was also assessed by monitoring at the RHEED pattern during growth.

An example of layer-by-layer RHEED calibration is shown in Figure III-12.

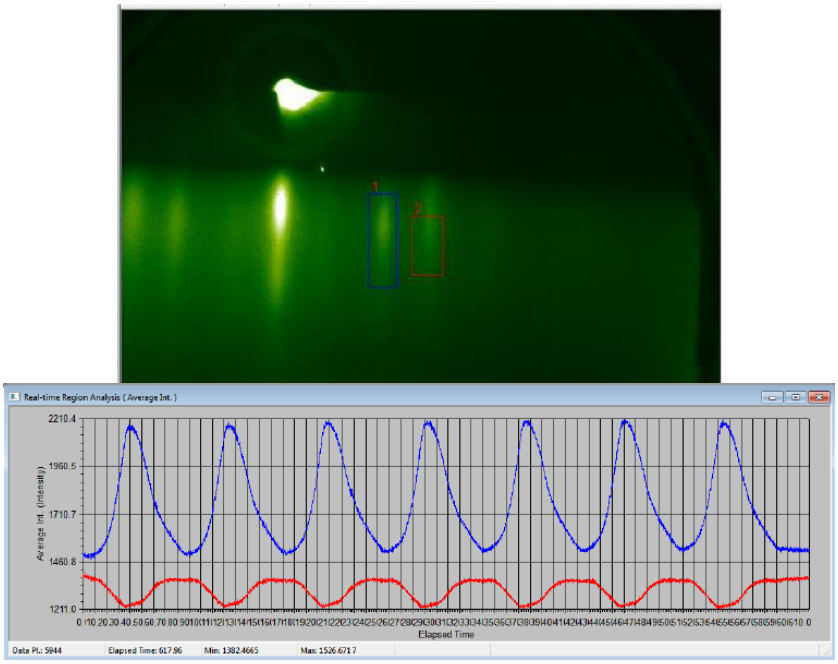

Figure III-12 *Layer-by-layer shutterd RHEED calibration on SCO. In the top panel a RHEED pattern during the calibration is shown. The intensity is acquired on the diffracted rod [10] (blue box and line) and on the incommensurate rod (red box and line).*

In Figure III-13 a) a typical RHEED pattern that was taken at the end of the growth of a SCO/SLCO/SCO QWs sample is shown. It contains extra streaks which disappear during the vacuum annealing step, Figure III-13 b). These extra streaks have been shown to be associated with a surface reconstruction related to excess oxygen (Harter et al., (2015)). They disappear as oxygen is removed during the vacuum annealing process.

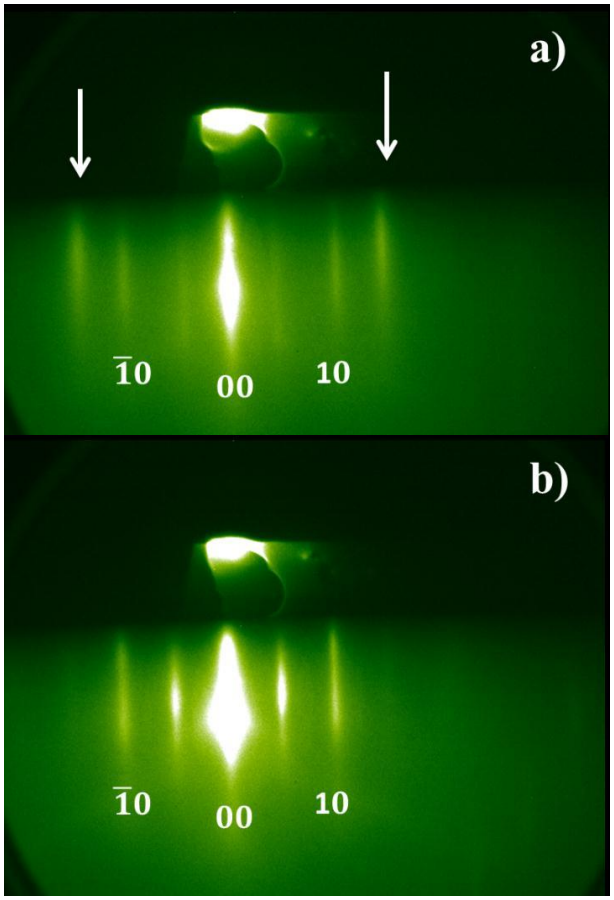

Figure III-13 *Typical RHEED pattern of a epitaxial QWs viewed along the $[110]_p$ azimuth at the end of growth (a) and after the vacuum annealing step (b). In (a) white arrows highlight extra diffraction streaks present in all as-grown films*

The $(SCO)_{20}/(SLCO)_y/(SCO)_{15}$ QWs (with y = 20,15,10,5,4,3, where y is the thickness of the SLCO in unit cells, u.c.) have been grown fixing the thicknesses of the top and the bottom insulating SCO layers and changing systematically y.

As seen in the case of SMO/LSMO/SMO QWs (as described in Section III.1), a SMO topmost layer 10 u.c. thick was shown to not limit the transport properties of the investigated systems. SMO is a Mott insulator with an energy gap of 0.35 eV, while SCO has an energy gap higher than 1.2 eV (Popovic et al., (2001)), and should ensure, for an interface roughness of

the same level, even better charge carriers confinement with similar thickness. Therefore, all SCO/SLCO/SCO QWs have been deposited with a topmost SCO layer thickness of 15 u.c.

III.2.1 Structural characterization

The samples were structurally characterized in order to check their quality. The XRRs and XRDs for the *n*-type QWs are shown in Figure III-14.

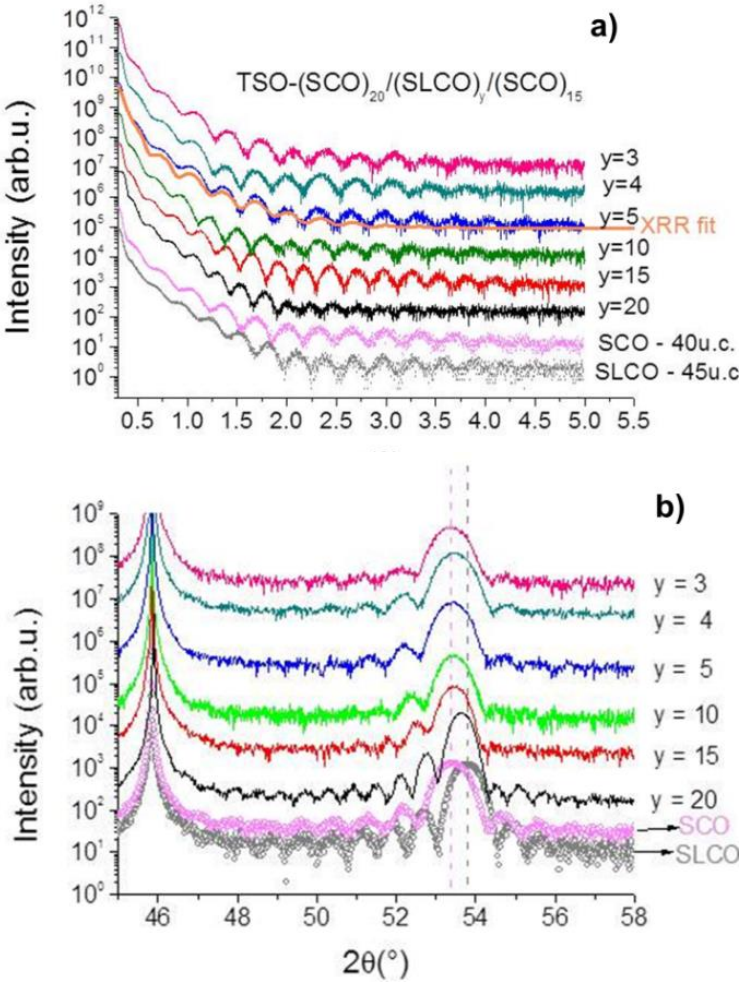

Figure III-14 *a) XRR spectra of single layers (SCO and SLCO) and of the trilayers with different SLCO thickness (y=20, 15, 10, 4 and 3), as a function of the incident angle θ. A fit of the reflectivity is shown for the sample with y=5; b) XRD spectra of the samples shown in a)*

The XRR measurements have been fitted with the layers' thickness, density and roughness as free fitting parameters. The Levenberg-Marquardt fitting routine with statistical weighting on the logarithm of the data was used. As shown in Figure III-14 a), the intensity oscillations are clearly visible for scattering angles up to θ = 4.5°, confirming the low roughness of the surfaces and interfaces. A Gaussian profile has been used for the

interface roughness; the standard deviation σ returned by the fitting routine is smaller than the unit cell (~0.34 nm) for all of the samples. In agreement with the calibration procedure and the shuttered period times used, the XRR measurements confirmed the bottom SCO thickness to be 20 u.c. and the top SCO layer to be 15 u.c., while the SLCO thickness varied from y=20 to y=3.

In Figure III-14 b) the XRD spectra of the same samples in Figure III-14 a) are shown. As outlined by the vertical dotted lines, the 200 diffraction peaks of the QWs always fall in between the 200 peaks of the SCO and SLCO single films, and progress, as expected, from the former to the latter with increasing y. In Figure III-15 XRD simulations (GlobalFit – Rigaku Corporation, Tokyo, Japan) are shown of the SLCO single layer (bottom curve) and of the $(SCO)_{20}/(SLCO)_{20}/(SCO)_{15}$ QW (top curve). The measured spectra result from the coherent addition of the contribution of each layer of the heterostructure that gives rise to the interference pattern between top and bottom SCO layers and to the Laue fringes. This addition results in a visible asymmetry of the Laue fringes, which is clearly reproduced in the simulation curve (see arrows in Figure III-15); around the sample peaks in Figure III-14 b) the fringes around the SLCO single layer are more symmetric. Again, as expected, this asymmetry decreases as the SLCO thickness in the QWs is lowered.

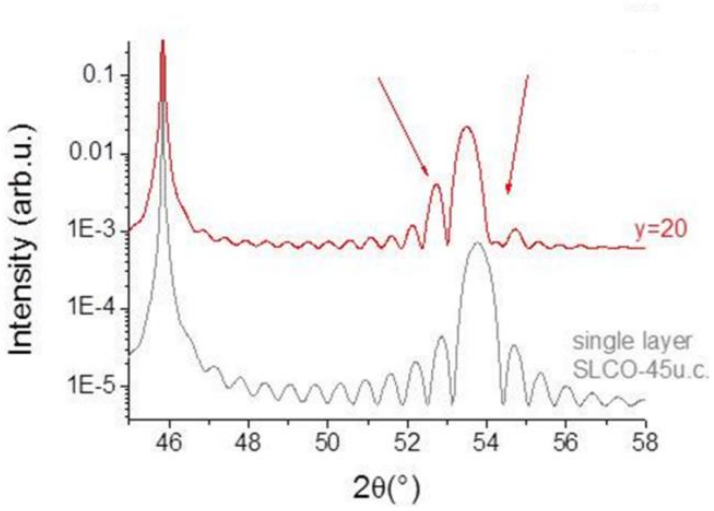

Figure III-15 *Simulation of the XRD spectra for the trilayer with SLCO y=20 (red curve) and SLCO single layer (grey curve)*

III.2.2 Electrical transport characterization

The electrical transport properties of the trilayers with different *y* values, have been analyzed performing sheet resistance measurements as a function of temperature using a van der Pauw four-probe geometry (Figure II-7) without patterning the samples, to reduce contamination and unwanted reactions.

Using eq. II-1, the resistivity ρ of the SLCO layer has been estimated, where *t* is the thickness of the SLCO layer obtained by XRR fits and the sheet resistance R_{sh} versus temperature T curves for the QWs with different SLCO thicknesses are shown in Figure III-16.

Typical errors related to R_{sh} values obtained using the van der Pauw method are around 10-15% (Van der Pauw, (1958)), and this could be the reason why samples with close *y* values (for example for *y*=4 and *y*=5) show very similar values of R_{sh}^{RT} and ρ_{RT} (see Table III-2).

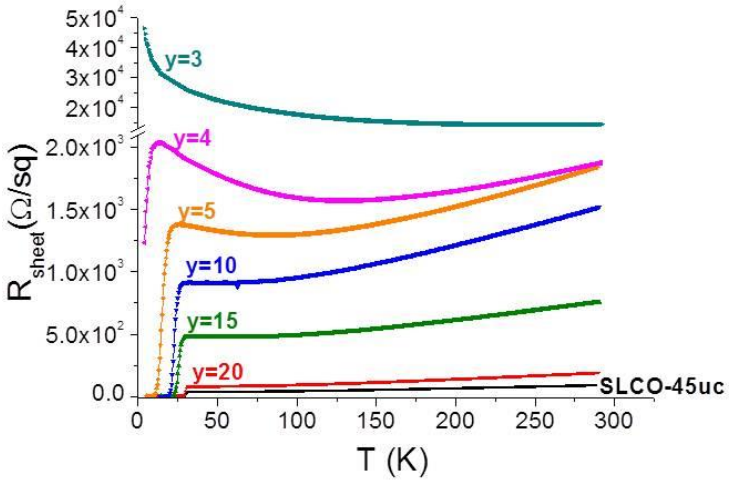

Figure III-16 *Sheet resistance R_{sheet} vs temperature T curves of trilayered samples with different SLCO layer thickness y in unit cells*

As already mentioned, the superconducting transition temperature T_C in SLCO thin films is generally dependent on many parameters (doping, disorder, strain, etc.) and can, therefore, be used as an additional check parameter for evaluating the quality of the samples. The T_C of the QWs shows a clear dependence on y. In particular, the T_C of the sample with y = 20 is the same as that of the 45 u.c. thick SLCO single layer, while for $y < 15$, T_C starts to decrease until it disappears for the sample with $y = 3$. For thicknesses $4 \leq y < 20$, an upturn in the R_{sh} values before the superconductive transition is observed, becoming more evident with decreasing SLCO thickness.

As mentioned, the growth of SCO/SLCO/SCO QWs with structurally abrupt interfaces, as confirmed by the XRR and XRD measurements, does not ensure by itself that the charge carriers are confined within the central SLCO layer. On the other hand, the observed superconducting behavior of the SLCO central layer gives the first indication of layering induced charge confinement. As shown in Figure III-17, the flat behavior of T_C vs y curve down to y = 10, with T_C values very close to that of a single 45 u.c. thick film, strongly suggests that the charge carriers are indeed spatially confined within the SLCO layer. If the carriers were spread out in a large part of the QW thickness the effective doping of the system should strongly decrease with decreasing y, reaching values where the superconducting behavior is no

longer expected. For example, the QW with y = 15 (T_C =30.5 K), should have an effective doping smaller than 3% and not exhibit superconductivity (Armitage et al., (2010)).

The sudden drop in T_C observed for y < 10 could also be related to the reduced dimensionality of the system induced by the layering. The influence of finite size on the order parameter of a second order phase transition can be proven within a Ginzburg-Landau formalism as the one proposed by (Simonin, (1986)), where a surface term is added to the free energy functional compared to the standard approach. Following (Simonin, (1986)), one obtains that critical temperature decreases with sample thickness t according to eq. III-2

$$T_C(t) = T_{C_0}\left[1 - \left(\frac{L_0}{t}\right)\right] \qquad \textit{III-2}$$

which has been shown to give good agreement with experimental data in for dirty (disordered) superconducting systems (Finkel'stein, (1994)). Although the data in Figure III-17 are reasonably described by using eq. III-2, a better χ^2value is obtained by using eq. III-3

$$T_C(t) = T_{C_0}\left[1 - \left(\frac{L_0}{t}\right)^2\right] \qquad \textit{III-3}$$

which is based on a Ginzburg-Landau approach with conventional boundary conditions, appropriate in the case of a clean electronic system. For both approaches, respectively given in eqs. III-2 and III-3, T_{C_0}represents the bulk critical temperature and L_0 is the critical thickness below which the superconductive transition is no longer present. In the insets to Figure III-17, the behavior and the linear fits (red lines) of T_C as a function of *1/y* (left) and of $1/y^2$ (right) are shown. The better agreement observed in the case of the $1/y^2$ dependence is confirmed by comparing the $\chi 2$ values obtained by eq. III-2 and III-3, respectively 2.2 and 0.9.

Eq. III-3 is equally applicable to ferromagnetic and superconductive phase transitions both described in terms of a generic order parameter depending only on the out-of-plane *z* coordinate being the system size finite along this direction. A few details about this calculus can be find in Appendix B.

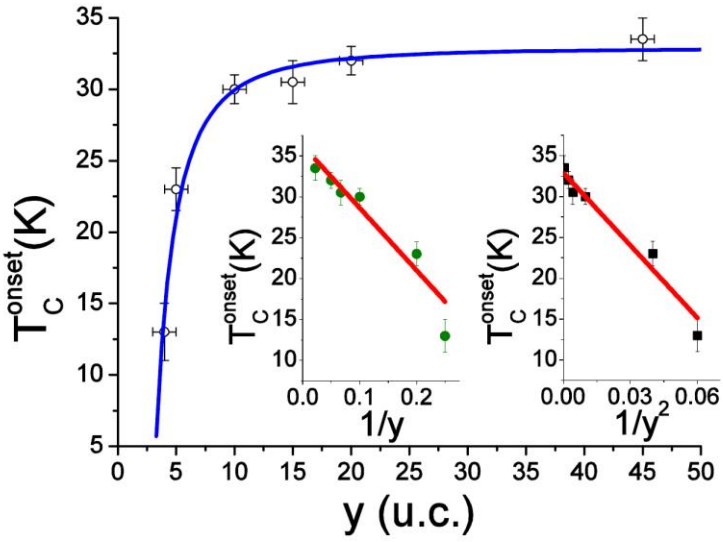

Figure III-17 *Critical onset temperature T_C^{onset} as a function of y where the blue curve is the best fit using eq. III-3. In inset, the behavior and the linear fit (red lines) of T_C^{onset} as a function of 1/y (left) and of 1/y^2 (right) are shown*

The better agreement that eq. III-3 gives to the experimental data in Figure III-17 suggests that disorder is not playing a major role in the sudden decrease of T_C with *t*. By fitting the data in Figure III-17 (blue curve), using eq. III-3, with T_{C_0} and L_0 free fitting parameters, we have obtained $T_{C_0} = (32.9 \pm 0.6)K$ and $L_0' = L_0/z' = (3.0 \pm 0.1)u.c$, where z' is the u.c. dimension along the *z* direction. The value for T_{C_0} is very close to the observed T_C for the single SLCO film 45 u.c. thick (T_C =33 K) and the critical thickness ${L_0}' = 3\ u.c.$ agrees well with our observation that the *y* =3 sample is not superconducting.

The normal state sheet resistance R_{sh} of the samples with 3 < *y* < 20 present an upturn at relatively low temperatures with a local minimum temperature T_{min}. The presence of these minima has been related in other systems to quantum interference effects (QIE) and the study of the low temperature resistivity curves has allowed, in this case, to infer about the system dimensionality (Lee and Ramakrishnan, (1985); Maritato et al., (2006); P Orgiani et al., (2015)). For all the SCO/SLCO/SCO samples showing these minima, the T_{min} values are in the range 50 – 130K (as reported in Table III-2), and it is hard to explain their presence in terms of the emergence of quantum phenomena due to electronic mean free paths of

the same order of magnitude of the inelastic dephasing length. Tentative fits of the R_{sh} curves in Figure III-16 over this temperature range, even allowing for a temperature dependence of the dephasing inelastic scattering time, confirmed the inconsistency to the experimental data. The T_{min} temperatures are close to the typical Néel temperatures measured in SLCO (Armitage et al., (2010)) and to the temperature at which a spin density-wave regime sets in for other electron-doped superconducting compounds (Jin et al., (2009)).

Table III-2 *Properties of the investigated n-type QWs with different SLCO layer thickness y*

***y* (u.c.)**	T_C^{onset} **(K)***	T_{min} **(K)**	ρ_{RT} **(mΩcm)**	R_{sh}^{RT}**(kΩ)**
(20±1)	(32±1)	--	(0.12±0.02)	(0.19±0.03)
(15±1)	(30.5±0.5)	(61.5±0.5)	(0.34±0.08)	(0.8±0.1)
(10±1)	(30±1)	(49.0±0.5)	(0.5±0.1)	(1.5±0.2)
(5±1)	(23±2)	(83.0±0.5)	(0.3±0.1)	(1.8±0.3)
(4±1)	(13±2)	(128.0±0.5)	(0.2±0.1)	(1.9±0.3)
(3±1)	Insulating	--	(1.3±0.7)	(14±2)

* T_C^{onset} is defined as the intersection of the straight lines describing the slope change before and after the superconducting transition

From the sheet temperature as a function of the temperature and of the layering, shown in Figure III-16, a sudden transition is observed in the normal state properties in going from the sample with y = 4 to that with y = 3. The sample with y = 3 does not have a T_{min}, does not show any metallic behavior ($dR_{sh}/dT<0$) and does not present any sign of a superconductive transition. In contrast, the sample with y = 4 has a T_C^{onset} around 13 K exhibits metallic behavior at high temperature and displays a T_{min} at about 120 K. Such a sudden transition from a "metallic" to an "insulating" behavior across a change of only one unit cell, is accompanied by a change in the R_{sh} low temperature values from about 2 kΩ to more than 30 kΩ. Typically, in a fermionic scenario, where the charge carriers are treated as single electrons, a crossover between superconducting and insulating behavior is expected when a threshold value of $R_{sh} = h/e^2$ = 25.8 kΩ is reached. On the other hand, if a bosonic scenario holds, with charge carriers treated as pairs, the cross-over R_{sh} threshold value is $R_{sh} = h/4e^2$ = 6.45kΩ

(Liu et al., (1991); Orgiani et al., (2007b)). The experimental data, with the superconducting $y = 4$ sample showing a $R_{sh} < 6.45$ kΩ and the insulating $y = 3$ one having $R_{sh} > 25.8$ kW, unfortunately do not allow to unambiguously discriminate between these two scenarios.

The $y = 3$ and $y = 4$ QWs' resistivity curves have been also analyzed at low temperatures (below 40K), as shown in Figure III-18.

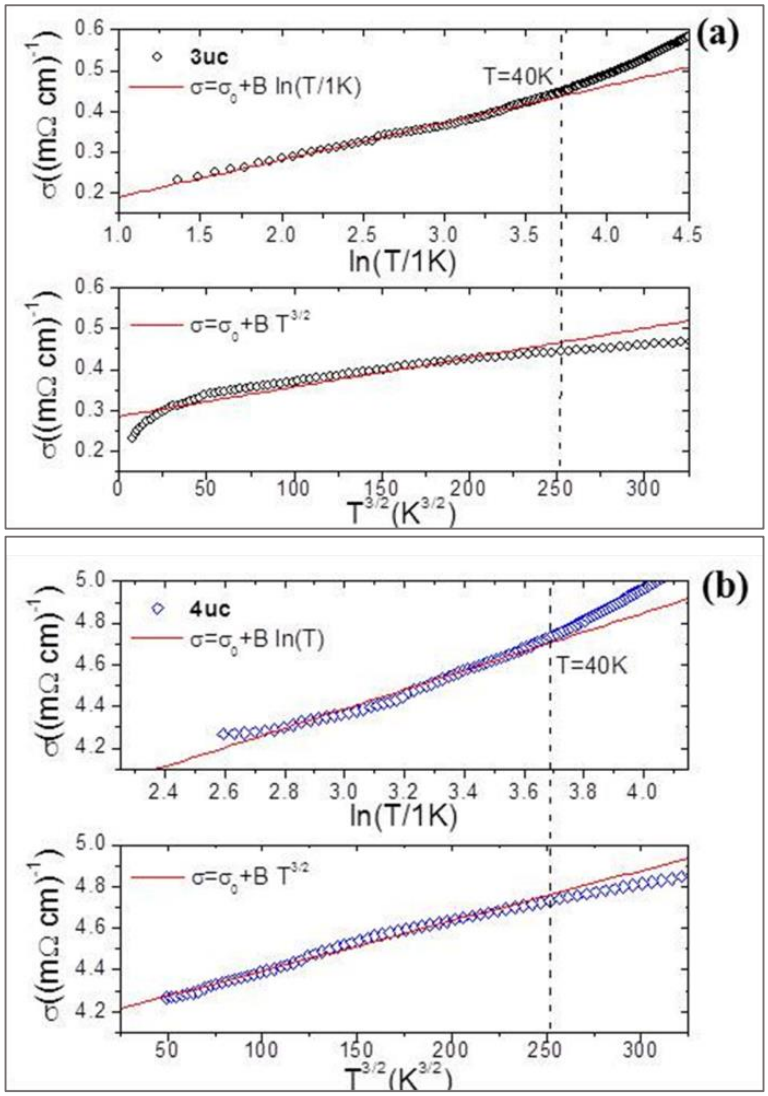

Figure III-18 *a) linear fit (red curves) of the low temperature (below 40K) conductivity for the samples with y =3 as a function of ln(T) (top) and $T^{3/2}$ (bottom); b) linear fit (red curves) of the low temperature (below 40K) conductivity for the samples with y = 4 as a function of ln(T) (top) and $T^{3/2}$ (bottom).*

In Figure III-18, the low temperature conductivity $\sigma = 1/\rho$ curves for the sample with $y = 4$ (Figure III-18 a)) and $y = 3$ (Figure III-18 b)) are plotted as a function of $ln(T)$ (bottom) and of $T^{3/2}$ (top). The red curves in the figures are obtained following the best linear behavior as a function of $ln(T)$ and $T^{3/2}$

respectively. As is clear from the figures, while the σ(T) curve for the $y = 4$ sample follows a $T^{3/2}$ dependence, that for the sample with $y = 3$ shows a *ln(T)* behavior.

QIE and weak localization (WL) effects are expected to play an important role in the conductivity of layered metallic systems (Kennett and McKenzie, (2008)) and have been unambiguously observed at low temperatures in several layered compounds by electrical noise spectroscopy (as also described in Section III.3.1) and by magnetoresistance measurements (Barone et al., (2013), (2009); Niu et al., (2016); P Orgiani et al., (2015); Rullier-Albenque et al., (2001)). If one assumes that QIEs are playing an important role in the low temperature electrical properties of our systems, the observed change in the dependence from $T^{3/2}$ to a *ln(T)* law can be traced back to a change in the dimensionality of the electronic system. In fact, the quantum correction term introduced by QIE in the electrical conductivity is dependent on the system dimensionality; specifically: a *ln(T)* QIE term is expected for two-dimensional (2D) systems, while a $T^{3/2}$ contribution is at work for three-dimensional (3D) systems, where the electron-phonon interaction is the mechanism affecting QIE (Lee and Ramakrishnan, (1985)). Therefore, the sudden change from a $T^{3/2}$ to a *ln(T)* conductivity dependence observed in these QWs going from $y = 4$ to $y = 3$, can be interpreted as a change in the dimensionality of the electronic system induced by the layering. Similar analysis performed over the same range of temperatures (T< 40K) on the samples with $4 \leq y < 20$, always yield conductivity behaviors better described by a $T^{3/2}$ dependence.

III.3 Doping effect on the normal and superconductive state of (Sr,La)CuO2

The growth and characterization of *n*-type QWs implies the preventive study of the behavior of the metallic single layers that led to further investigation of the normal state transport properties of the infinite layer (Sr,La)CuO_2. The infinite-layer (IL) structure of the parent compound SCO, with only one Cu-O_2 plane per unit cell and the absence of oxygen atoms in the Sr layers, is the simplest undoped parent structures in the cuprate family hosting high-T_C superconductivity. The IL cuprate structure offers unique

opportunities to define the proper regime of the transport properties, having removed the ambiguity regarding the truly conducting layer, thus making the investigation more general than the specific case of the electron-doped cuprates.

Angle annular dark field (HAADF) Scanning Transmission Electron Microscopy (STEM) images of a (Sr,La)CuO_2 sample, shown in Figure III-19, has been obtained by Kourkoutis Electron Microscopy Group in Cornell University, Ithaca (NY) – USA. Epitaxial growth characterized by abrupt interface with the substrate ($TbScO_3$), without any diffusion and absence of defects, can be observed. The abruptness of interfaces plays a key role in the quantum confinement. The charm of this technique is the atomic resolution of the images. Indeed, in Figure III-19, it can be seen the atoms of the thin film and of the substrate as well. A schematic sketch of their crystal structures is superimposed on the STEM image acquired.

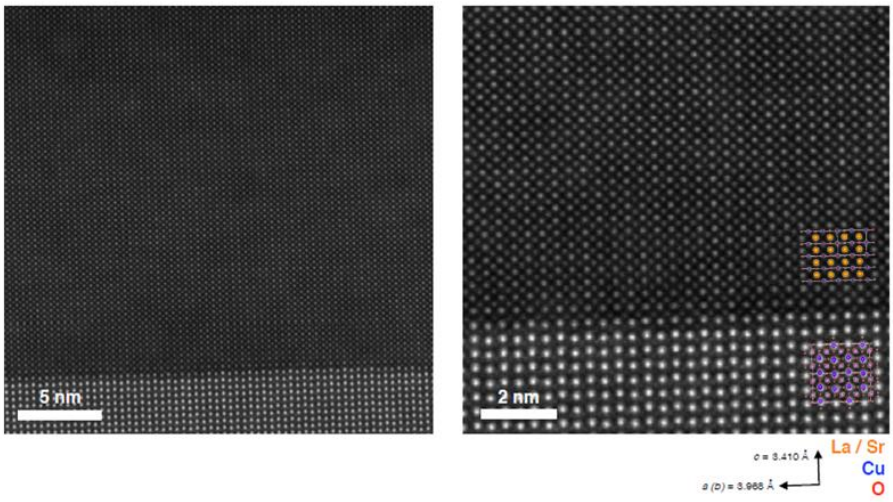

Figure III-19 *Two magnification of STEM image of SLCO thin film grown on a $TbScO_3$ substrate. Abrupt interface is observable, without diffusion and absence of defects, confirming the epitaxial growth of the samples*

(Sr,La)CuO_2 single layer thin films have been studied in function of doping in order to compare the doping effects with the layering effects on the normal and superconductive states.

III.3.1 The role of Quantum Interference Effects on the normal state

Under-doped infinite-layer electron-doped (e-doped) cuprate $Sr_{1-x}La_xCuO_{2\pm\delta}$ (SLCO) samples clearly show a metal-to-insulator transition (MIT) at low temperatures and, with the aim of revealing the true nature of the MIT in electron-doped cuprates, electrical transport properties in function of temperature and of the doping of these thin films have been investigated. This work has allowed the determination of the fundamental physical mechanism behind the upturn of the resistivity, namely the quantum interference effects (QIEs) in three dimensional (3D) systems, providing its evidence because of electronic correlations. Moreover, the metallic-like normal state is always best described by a linear non-saturating (non-Fermi liquid) behavior of resistivity (Barone et al., (2016); P Orgiani et al., (2015)).

Taking into account the QIEs contribution, a non-Fermi liquid behavior characterized by a linear-T dependence of the resistivity can be identified over the whole investigated temperature range (up to 300 K). Following reports on other e-doped cuprate systems, such a dependence has been recently attributed to critical spin fluctuations originating from an anti-ferromagnetic quantum critical point (Butch et al., (2012); Jin et al., (2011)) rather than a conventional phonon-based scattering scenario at high temperatures as predicted by the Bloch-Grueneisen law (Abrikosov, (1988)).

SLCO thin films have been grown at Cornell University with the same deposition technique describe in Section III.2 and by (Maritato et al., (2013)) and all the electrical transport properties have been carried out by standard four-point-probe DC technique in the Van der Pauw configuration (Figure II-7) without patterning the samples.

Several works have pointed out the possible presence of QIEs in the low-temperature transport properties of disordered electronic systems. In high quality thin films, in principle, it is possible to study the QIEs and to discriminate the physical mechanism sustaining them, such as Coulomb interactions, weak localization effects, dimensionality (e.g., 3D and/or 2D behavior) (Lee and Ramakrishnan, (1985)).

In SLCO under-doped thin films (i.e. $x < 0.1$) the insulating state is strong enough to produce a clear upturn of the resistivity at low temperature, but despite this upturn, all the samples show a clear transition to the superconducting state (Figure III-20).

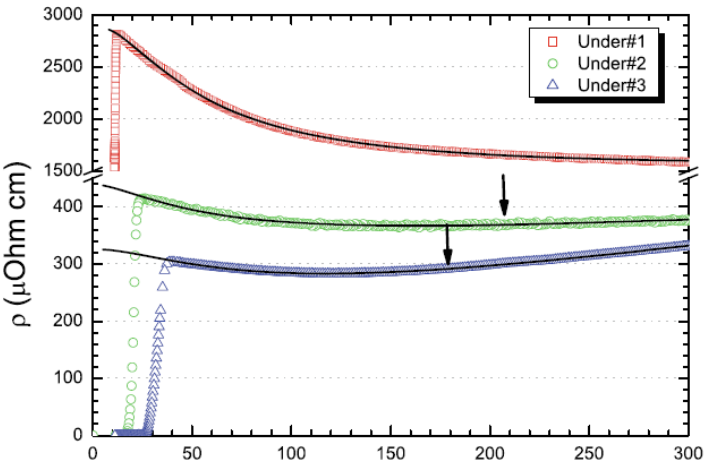

Figure III-20 *Resistivity curves for three selected under-doped SLCO samples. The best-fit curves are also reported. Arrows indicate the temperatures below which the resistivity curves are no longer purely linear, namely T**

A metallic-like behavior of the resistivity $\rho_M(T)$, the quantum correction to the residual resistivity $\rho_0(T)$ (eqs. III-4 and III-5) or a generic insulating term $\rho_I(T)$ (eq. III-6) con be included as follows:

$$\rho(T) = \rho_0^{2D}(T) + \rho_M(T) = \frac{1}{\sigma_0 + B \cdot ln(T)} + \rho_M(T) \qquad \textit{III-4}$$

$$\rho(T) = \rho_0^{3D}(T) + \rho_M(T) = \frac{1}{\sigma_0 + B \cdot T^{p/2}} + \rho_M(T) \qquad \textit{III-5}$$

$$\rho(T) = \rho_0(T) + \rho_I(T) + \rho_M(T) \qquad \textit{III-6}$$

The localization terms for the $\rho_I(T)$ in eq. III-6 considered (e.g., $\rho_I(T) \sim \exp(T_0/T)^{\beta}$ with β equal to 0.25 and 0.5 for the Mott variable-range-hopping and the Efros-Shklovskii localization (Coey et al., (1995))) gave the statistical χ^2 values[a] fairly larger (more than 2 orders of magnitude) than

[a] $\chi^2 = \frac{1}{N}\sum_{i=1}^{N} \frac{\left(\rho^i_{experimental} - \rho^i_{fit}\right)^2}{\left(\rho^i_{fit}\right)^2}$

those obtained by considering QIEs' formulas, thus clearly demonstrating that the insulating state is driven by these additional terms.

The dimensionality of the localization mechanism (i.e. 3D or 2D) was determined by routinely comparing the calculated χ^2 by using eqs. III-4 and III-5). The obtained χ^2 relative to the samples shown in Figure III-20 as reported in Table III-3 . Moreover, in the 3D localization formula (eq. III-5), *p* depends on the dominant scattering mechanism and has a value of 1 for the electron-electron interaction correction term, while for weak localization phenomena, it becomes 3/2 for electron-electron collisions in the dirty limit, 2 for electron-electron scattering in the clean limit and 3 for electron-phonon processes (Lee and Ramakrishnan, (1985)). The quadratic $A \cdot T^2$ power-law (i.e., Fermi-liquid behavior) and the linear $A \cdot T$ dependencies have been considered respectively for the metallic resistivity ρ_M. Therefore, A, σ_0 and B, are the free fitting parameters.

Table III-3 *Normalized χ2 values for SLCO samples shown in Figure III-20; data refer to the fitting procedure by using the 2D (eq. III-4) and 3D (eq. III-5 with the different exponent p) localization terms, respectively*

Sample	ρ_0^{2D}	ρ_0^{3D}			
		p = 1	*p = 3/2*	*p = 2*	*p = 3*
	(10^{-5})	(10^{-5})	(10^{-5})	(10^{-5})	(10^{-5})
Under#1	88	23	11	6.0	**1.6**
Under#2	2.5	2.1	2.0	1.8	**1.5**
Under#3	2.1	0.84	0.6	0.52	**0.34**

Remarkably, the 3D localization formula (eq. III-5 fits the experimental data better with respect to the 2D term (eq. III-4) (marked in bold in Table III-3). Such a result was quite unexpected; it is generally assumed that the IL structure is a system of weakly-coupled 2D sheets, as also sustained by the large difference between the out-of-plane and the in-plane resistivity (Armitage et al., (2010); Hagen et al., (1992); Tanda et al., (1991)). Furthermore, the $T^{p/2}$ correction to the low-temperature conductivity also excluded the occurrence of localization phenomena due to the Kondo effect (Sekitani et al., (2003)), which however predicts, similarly to 2D-QIEs

correction, a logarithmic correction to the conductivity with decreasing temperature (Kumar et al., (2002)). The best-fit value for the exponent p in 3D localization term was constantly 3, thus indicating that the electron-phonon scattering mechanism is dominating the QIEs phenomenology. Regarding the metallic term, ρ_M was always best-fitted by a linear-T dependence which persisted down to low temperatures without any transition to a different power-law dependence.

Having established that QIEs dominate the MIT transition at low temperature in under-doped cuprates, the possibility that they can also affect the transport properties of optimal-doped samples has been investigated.

As the optimally doped regime is approached (i.e., the carrier concentration increases), the upturn of the resistivity becomes more and more shallow and the minimum is pushed to lower and lower temperatures, until no upturn is observed (Figure III-21).

A possible scenario is that QIEs contribution naturally tends to be weaker and weaker with increasing metallicity and does not abruptly vanish. Therefore, the quantum correction to residual resistivity term in the fitting formulas even for the optimal-doped SLCO sample can be kept.

For comparison, the resistivity curve has been fitted also by a generic T^n power law dependence

$$\rho(T) = \rho_0 + A \cdot T^n \qquad \textit{III-7}$$

with ρ_0, A and n as fitting parameters. As successfully demonstrated for a similarly strongly correlated system (Mercone et al., (2005); Orgiani et al., (2007a)), the best-fit value of n helps to reveal the main active scattering process among several different ones, ranging from the interaction with thermal as well as acoustic phonons, spin-wave scattering phenomena, and others (Abrikosov, (1988); Kittel, (2005); Mott N.F., (1990)). It is important to emphasize that the power low exponent n of the metallic contribution ρ_M in eqs. III-4 and III-5 is fixed at 1 or 2, while in ρ_{metal} (eq. III-7) n is free to vary, so the free fitting parameters are 3 for both the equations considered, therefore the χ^2 values are comparable.

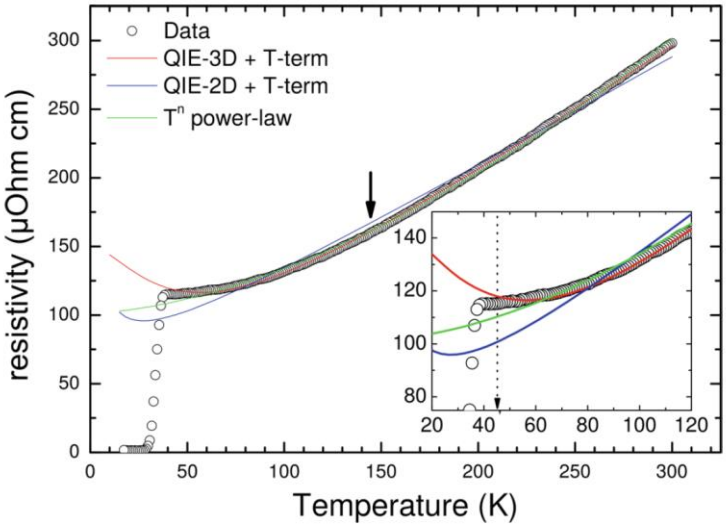

Figure III-21 *Resistivity curve for a representative SLCO sample characterized by an electronic doping close to optimal condition. The fitting curves are also reported. Arrow in the main panel indicates the temperature below which the resistivity curves are no longer purely linear; in the inset, the resistivity behavior and fitting curves are magnified in proximity of the superconducting transition (arrow indicates the lower limit of fitting range)*

The result, reported in Table III-4, is that a linear-T and a QIEs localization term better fit the experimental data of the optimally doped SLCO sample than a T^n power law dependence (Butch et al., (2012)). In addition, the best-fit value $n = 1.65$, obtained by fitting the resistivity curve in Figure III-21 using eq. III-7, cannot be trivially correlated to any known scattering process. Furthermore, the 3D localization term ρ_0^{3D} always showed the smallest χ^2 value and the best-fit value ($p = 3$) pointed again towards the dominant electron-phonon scattering mechanism driving the QIEs.

In other words, even though it is not strong enough to produce an upturn of the resistivity, the presence of the QIEs-driven insulating state might considerably affect its evolution in proximity to the superconducting transition by flattening the low-temperature regime of $\rho(T)$.

Table III-4 *Statistical $\chi 2$ values as well as best-fit parameters for the optimally doped SLCO sample shown in Figure III-21.*

Sample	***n***	***A***	σ_0	***B***	χ^2
		$\mu\Omega cmK^{-1}$	$10^{-3}(\mu\Omega cm)^{-1}$	$10^{-6}(\mu\Omega cm)^{-1}K^{-3/2}$	10^{-5}
ρ_0^{3D} (p=3)	1	0.96	6.3	21.9	1.21
ρ_0^{2D}	1	0.82	3.6E-14	4.1E3	78.4
ρ_{metal}	1.65	0.016	9.85	--	3.86

III.3.1.1 Noise spectroscopy measurements

To better clarify the presence of QIE in our samples, we have also performed noise spectroscopy measurements.

Electrical noise spectroscopy is a very sensitive and non-destructive technique, such as electric noise, has been used to analyze the samples, because it is capable to reveal a strict connection between WL effects and specific properties of the low-frequency *1/f* noise (Barone et al., (2016); P Orgiani et al., (2015)). In particular, a linear dependence of the voltage-spectral density S_V on the bias current (I) is observed in systems undergoing a WL transition (Barone et al., (2015), (2013), (2009)), while far from the weak localization region, the usual quadratic behavior of S_V vs I is found. The origin of this unusual electric noise mechanism appears to have a universal nature, whose explanation has been given in terms of non-equilibrium universal conductance fluctuations (Barone et al., (2013)). A summary of these measurements can be find in Appendix C.

The experimental results are very similar to the ones already reported for superconducting cuprates and manganite thin films in weak localization regime (Barone et al., (2013), (2009)). In particular, standard resistance fluctuations (whose contribution is proportional to I^2) are the source of the electric noise when the system behaves as a metal at high temperatures and close to the superconducting transition, where a noise peak due to fluctuation of the superconducting percolation network is observed (Kogan, (1996)). Conversely, the appearance of a linear bias dependence of the $1 / f$ noise (large a_1 parameter) is directly related to the occurrence of QIEs.

III.3.2 Low temperature hidden Fermi-liquid charge transport in (Sr,La)CuO_2

As introduced in Section I.4.2.3, most of studies on the cuprate phase diagrams have been performed on *p*-type materials. Nevertheless, with the few data available for *n*-doped materials it can be possible to point out similarities and differences between these two compounds (Armitage et al., (2010)), such as the antiferromagnetic behavior present in the lower doping part of their phase diagram or a sudden upturn of the resistivity in the lower doped samples (Armitage et al., (2010); Rybicki et al., (2016)). In addition, a linear temperature dependence of the resistivity is observed at temperatures T higher than doping-dependent T^* for both *n* and *p*-doped materials. It is recalled that the temperature T^* separates the so called strange-metal regime ($T > T^*$) from the region with the opening of a pseudo-gap (Gurvitch and Fiory, (1987); Li et al., (2008); Shekhter et al., (2013)).

The opening of the pseudo-gap below T^* has been attributed to non-FL behavior in proximity of a quantum transition to the antiferromagnetic phase (Keimer et al., (2015); Li et al., (2009); Shekhter et al., (2013)).

Moreover, the cotangent of the Hall angle ($cotg(\theta_H)$) of the *p*-doped $HgBa_2CuO_{4\pm\delta}$ compound, presenting only one CuO_2 plane per unit cell, follows a T^2 dependence independently of doping with no appreciable changes upon crossing the temperatures T^{**} and T^* (Barišić et al., (2017)). More recently, Li et al. observed similar behaviors in *n*-doped cuprates. In particular, values of the sheet resistance coefficients very close to those measured for *p*-doped compounds with the same doping level have been observed along with transport scattering rates similar to the ones obtained in the case of *p*-doped materials, suggesting a universal description of the normal state in cuprates, independently of doping, compound and carrier type (Li et al., (2016)). Probably due to scarcity of available samples, the analysis done by Li et al. have not been performed on SLCO samples. These materials, thanks to their simple crystal structure presenting only one CuO_2 plane per unit cell, remove the ambiguity about the effective thickness of the conductive layer. Indeed, analyzing the transport properties of cuprates, a critical uncertain is always related to their complex structure and to the ambiguity in the definition of the effective thickness of the conducting layer.

In this work, the same analysis done by Li et al., has been performed also on SLCO films. The obtained results asses the presence of FL universal behaviors in the low-temperature transport properties of IL *n*-doped superconducting cuprates, removing the ambiguity regarding the truly conducting layer, and allows more general investigation of the superconducting and normal-state properties in these materials, independently of doping and carrier type.

The samples were characterized by XRDs and electrical transport measurements as well, as already described in previous Sections. The resistivity has been estimated using eq. II-1, pointing out again that in case of electron-doped IL cuprates there is no ambiguity in identifying the truly conducting layering.

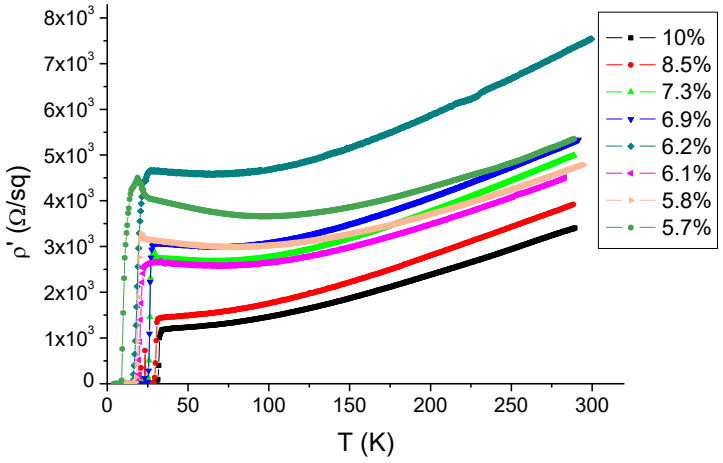

Figure III-22 Sheet resistivity as a function of temperature and doping

In Figure III-22, the sheet resistivity curves as a function of the temperature for SLCO films with different doping are shown, where $\rho' = \rho/c$ with c the measured crystal axis along the growth direction (~ 0.34 nm). At high temperature (up to T^*) the $\rho'(T)$ curves of underdoped and optimally doped samples ($n \leq 0.1$) show a linear behavior with no sign of saturation, while the curves of overdoped samples ($n > 0.1$) present a tendency to saturation becoming more clear with increasing doping (not shown here).

In Table III-5 the main structural and electrical transport values for the investigated samples are reported, where T_{min} is defined as the temperature of the upturn (the local minimum in the $\rho'(T)$ curves), the onset of the superconducting critical temperature T_C^{onset} is defined as the intersection of the straight lines describing the slope change before and after the transition, ρ'_0 (Ω/sq) is the residual sheet resistivity, T^* is the lowest temperature describing a linear behavior in temperature of the resistivity and T^{**} is the highest temperature describing a quadratic temperature dependence of the resistivity.

Table III-5 *Main structural and electrical transport values for the investigated samples*

n	$\mathbf{T_C^{onset}}$ **(K)**	$\mathbf{T_{min}}$ **(K)**	$\boldsymbol{\rho'_0}$ **(Ω/sq)**	**T* (K)**	**T** (K)**
0.057	19±1	98.0±0.5	3313.2±0.9	< 290	< 290
0.058	20±1	79.0±0.5	2731±1	268±1	248±1
0.061	22±2	69.0±0.5	2343.5±0.9	213±3	203±1
0.062	23±2	64.0±0.5	4250±1	246±4	215±5
0.069	27±2	69.0±0.5	2744.1±0.9	231±2	191±3
0.073	29±1	65.5±0.5	2400.0±0.2	221±1	170±1
0.085	33±2	No min	1394.4±0.6	194±2	160±5
0.1	35.0±0.5	No min	1147.4±0.3	222±1	163±1

The behaviors of T_c^{onset}, T^* and T^{**} as function of doping are shown in Figure III-23. The lines describe the doping dependence of T^* and T^{**}.

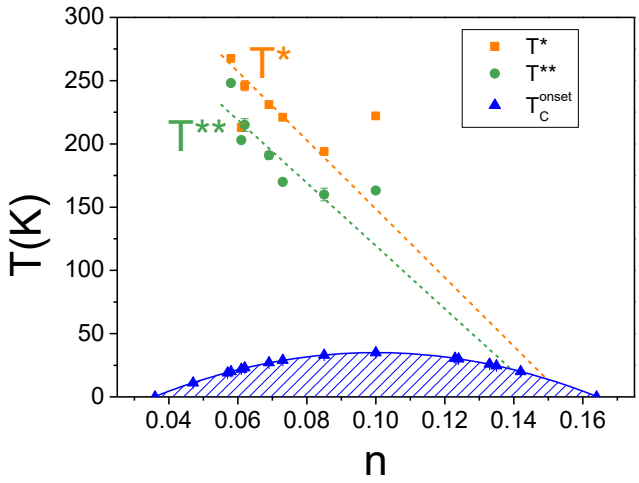

Figure III-23 *Doping dependence of T*, T** and* T_C^{onset} *of the investigated samples; the dashed lines describe the behavior of T* and T***

As already described in Section III.3.1, an upturn in the $\rho'(T)$ values before the superconductive transition is observed in underdoped samples, becoming more evident with decreasing doping values.

The low-temperature upturn in the resistivity curves of underdoped cuprates has been related to several mechanism, such as Kondo scattering (Sekitani et al., (2003)) or weak localization (WL) effects (Hagen et al., (1992)). Indeed, in SLCO films the presence of WL has been proved by low-frequency voltage spectral density measurements and it has been also proposed to influence the normal state transport properties in a larger temperature range, where the three-dimensional (3D) localization mechanism associated to the electron-phonon scattering was shown to give always a better agreement to experimental data than the two-dimensional (2D) mechanism, associated to a logarithmic correction (Barone et al., (2016); P. Orgiani et al., (2015)), as described in Section III.3.1.

A further analysis performed on SLCO films as a function of doping has been carried out following the work of Li et al. in order to compare the results (Li et al., (2016)). So the sheet resistivity has been described using three terms:

$$\rho'(T) = \rho'_0 + \Delta\rho'(T) + A_{2\square}T^2 \qquad \textit{III-8}$$

where ρ'_0 is the residual resistivity (T = 0 K), in general very close to the resistivity value in T_{min}, $\rho'(T_{min})$, and the $\Delta\rho'(T)$ term is associated to the low temperature upturn and has been expressed, in agreement with the work of Li et al., to exhibit a logarithmic temperature dependence with

$$\Delta\rho'(T) = -A_{log\square} log\left(\frac{T}{T_{log}}\right) \qquad \textit{III-9}$$

Fixing

$$A_{0\square} = \rho'_0 - A_{log\square} log\left(\frac{T_{log}}{1K}\right)$$

The eqs. III-8 and III-9 can be written again:

$$\rho'(T) = A_{0\square} - A_{log\square} log\left(\frac{T}{1K}\right) + A_{2\square}T^2 \qquad \textit{III-10}$$

Li et al have fitted their data by the eq. III-10, using $A_{0\square}$, $A_{log\square}$ and $A_{2\square}$ as free fitting parameters, that are A_0, A_{log} and A_2 normalized to the number of CuO_2 planes per unit cell.

For both *n* and *p*-doped cuprates, Li et al. observed that the $A_{2\square}$ coefficients are independent by the particular type of material and show similar values at the same level of doping and is inversely proportional to the charge carrier concentration. They also found $A_{0\square} \propto n^{-3.4\pm0.3}$ and $A_{log\square} \propto n^{-3.6\pm0.3}$ doping dependencies with an approximately linear relationship between $A_{0\square}$ and $A_{log\square}$ holding over many order of magnitude.

In Figure III-24, the $A_{2\square}$ (blue triangles) values as a function of the doping *x* obtained by fitting the low temperature resistivity curves of the samples reported in Table III-5 with eq. III-10, are shown and these values show a *1 / n* dependence which is in reasonable agreement with data points. In addition, the $A_{2\square}$ values are very close to those obtained for other electron doped superconducting cuprates at similar doping levels (Li et al., (2016)).

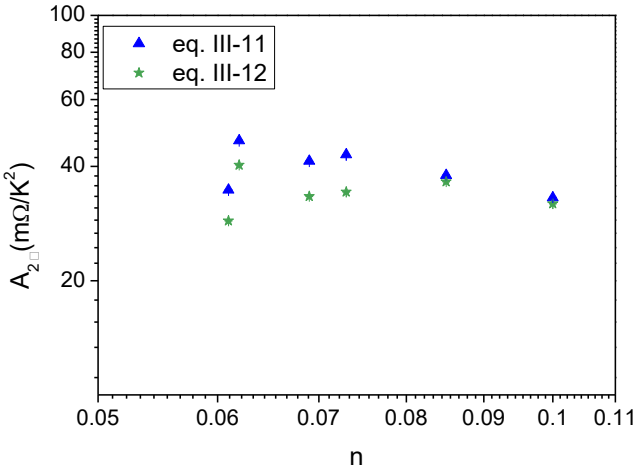

Figure III-24 *$A_{2\square}$ values obtained by fitting the resistivity curves with eq. III-11 (blue triangle) and with eq. III-12 (green stars)*

The $A_{0\square}$ values obtained by the same fitting procedure are also dependent on the doping level with $A_{0\square} \propto n^{-2.5\pm0.6}$ (Figure III-25 a)) which is close, inside the accuracy, to the exponent obtained by Li et al. for their *n*-doped materials. However, the $A_{log\square}$ values found for the samples with the minimum, i.e. with doping n < 0.085, do not show a clear dependence upon the doping (Figure III-25 b)), even though a linear relationship among the $A_{0\square}$ and $A_{log\square}$ is still valid (Figure III-25 c)) with data points falling on the same curve followed by (Li et al., (2016)).

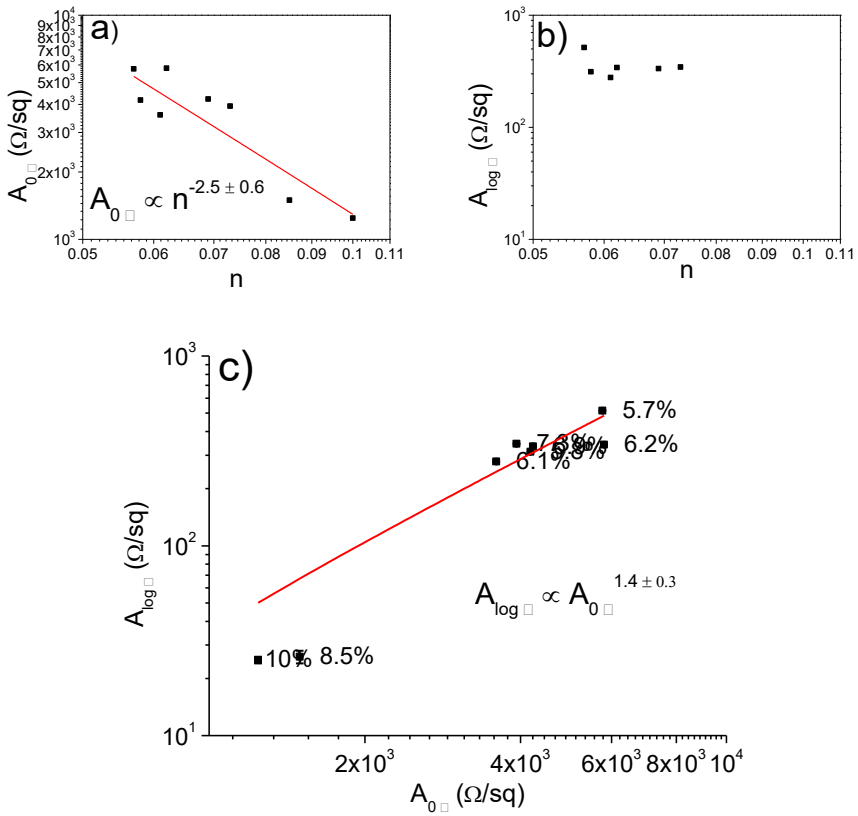

Figure III-25 *Doping dependence of a) $A_{0\square}$ and b) $A_{log\square}$ obtained by fitting the resistivity with eq. III-8; c) scaling relation between $A_{log\square}$ and $A_{0\square}$. The power-law exponents are reported as insets*

These results, with the $A_{2\square}$ coefficients showing *1 / n* dependence and values close to those observed in other *n*-doped superconducting cuprates at comparable doping levels, along with the similar *n*-scaling law of the $A_{0\square}$ coefficients, indicate the possible presence in the low temperature range of FL behaviors also in these IL *n*-doped cuprates.

As shown in Figure III-25 b), $A_{log\square}$ values doesn't show a clear doping-dependence, but it exhibits a linear dependence with the $A_{0\square}$ values (Figure III-25 c)), as for the other *n*-doped cuprates investigated by (Li et al., (2016)). This behavior can be probably traced back to the fact that in the low temperature range ($T_{min} < T < T^{**}$), the resistivity curves of underdoped samples are plausibly described in terms of the eq. III-11

$$\rho'(T) = \rho'_0 + A'_{2\square} T^2 \qquad \textit{III-11}$$

As a consequence, the difference between $A_{0\square}$ and $A_{log\square}$ appearing in eq. III-10 is related to the constant value of the residual resistivity ρ'_0, ensuring the linear dependence between $A_{0\square}$ and $A_{log\square}$ values, independently of the particular doping dependence.

The resistivity curves of the samples considered have also fitted using eq. III-11. The $A'_{2\square}$ values (green stars in Figure III-24) obtained by this procedure don't differ much from the $A_{2\square}$ values obtained with eq. III-10, as it can be observed in Figure III-24. In the underdoped region, the $A'_{2\square}$ values are slightly higher than the $A_{2\square}$ ones and, approaching the optimally doped regime, they start to coincide.

The results discussed seem to confirm, in agreement to the work of Li et al., the presence of hidden FL charge transport in the low temperature properties of IL *n*-doped cuprates.

To further analyze the normal state transport properties of these samples, Hall measurements have been performed on a typical underdoped sample ($n \approx 0.07$).

In Figure III-26 a) , it is shown the temperature behavior of 1 / R_H, where R_H is the Hall coefficient.

After the subtraction of the logarithmic contribution (Figure III-26 b)), that is a non-universal contribution, it is find that

$$cot(\theta_H) = \frac{\rho_i}{HR_H} \qquad \textit{III-12}$$

where $\rho_i = \rho - \left(A_0 - A_{log} \log\left(\frac{T}{1K}\right)\right)$.

As it is clear from Figure III-26 c), the $\cot(\theta_H)$ has a T^2 ($\cot(\theta_H) \propto C_2 T^2$) dependence up to temperature of about 120K, close to the T^{**} value and of the same order of the typical Néel temperature observed in underdoped cuprates (Armitage et al., (2010)). Moreover, the slope of the $\cot(\theta_H)$ in this temperature range has a value of C_2 = (0.0262 ± 0.0004) K^{-2}, very close to the universal value found for other *p* and *n*-doped cuprates (Barišić et al., (2015); Li et al., (2016)).

The T^2 dependence is lost at higher temperatures and this is probably due to the presence of more complex Fermi surface shape with the Hall coefficient ceasing to be a representative measure of the carrier densities (Onose et al., (2001)).

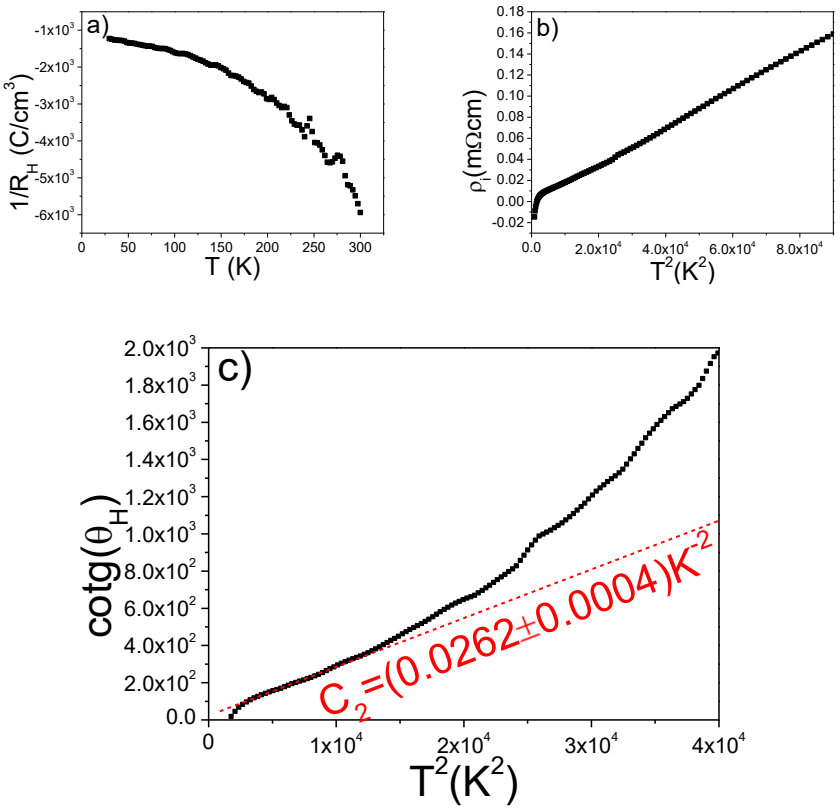

Figure III-26 *a) $1/R_H$ data obtained for an underdoped sample; b) resistivity after subtraction of fitted logarithmic contribution; c) cotangent of Hall angle (the dashed red line indicate $cot(\theta_H) \propto C_2 T^2$)*

III.3.3 X-ray absorption spectroscopy (XAS) study of annealing process on (Sr,La)CuO_2 thin films

The superconducting properties of SLCO thin films are strongly affected by sample preparation conditions. In particular, a reduction process is needed for all electron doped cuprates in order to get superconductivity, but there is often little control on this step, especially on thin film samples.

Therefore, the optimization of this step is crucial for the quality of SLCO thin films and, consequently, of the *n*-doped QWs based on this compound.

It is well known that e-doped cuprates need an oxygen reduction process in order to become superconducting (Armitage et al., (2010); Fournier, (2015); Li et al., (2009)), so for the SLCO thin films a vacuum annealing is performed in situ after growth (Maritato et al., (2013)).

The mechanism activated by the reduction process is still unclear; it is commonly accepted that it removes excess oxygen present at the Cu apical site (that is unoccupied in the *n*-doped cuprate structures, while apical oxygen is present in *p*-doped compounds) (Armitage et al., (2010); Li et al., (2009)). In contrast with this notion, a transmission microscopy study of electron-doped $Nd_{2-x}Ce_xCuO_4$ has revealed that other structural modification occur, involving the migration of Cu ions, while the amount of oxygen removed is usually very small (Adachi et al., (2013)) and close to the detection limit of many experimental methods. Moreover, experiments with higher sensitivity to oxygen removal, such as neutron diffraction, are extremely difficult to perform on thin film samples.

Signature of apical oxygen removal during the annealing process have been reveled thanks to XAS measurements. In particular, a systematic study of annealing effect (and consequently of the oxygen content) has been done on a set of SLCO samples. These samples were firstly structural characterized (XRDs measurements) as well as the electrical transport properties and then XAS measurements were performed on Cu $L_{2,3}$ and O *K* edges. Indeed, XAS measurements have revealed the modification of Cu coordination and of the density of states (DOS) at the conduction band; this is related to the signatures of apical oxygen removal during the annealing process.

Epitaxial SLCO films were grown on $DyScO_3$ (110) substrate using RHEED calibrated shuttered layer-by-layer MBE technique, as described in Section II.1 (Maritato et al., (2013)). The samples have been annealed *in-situ* in vacuum for 15, 30 and 60 min at the end of the growth, while the "as-grown" sample (0 min in Figure III-27) was cooled down in deposition atmosphere. The as-grown samples were cooled down in the same pressure of distilled ozone in which they were deposited, then it was annealed in a chamber connected to the XAS measurement chamber in 1 Torr of Ar.

The samples were monitored by RHEED pattern during the annealing process, following the evolution of the surface reconstruction (Harter et al., (2015)).

XAS spectra were measured at Elettra Synchrotron in Trieste, Italy at Cu $L_{2,3}$ and at O *K* edges. Furthermore, at Elettra the as-grown samples were annealed at 350°C in 1 Torr of Ar for timed ranging from 5 to 15 min, using

a chamber connected to the XAS measurement chamber. Consequently, XAS spectra were measured before and after each annealing step.

The measurements were performed using linearly polarized light with the electric vector $\boldsymbol{E}$ parallel (H polarization) and perpendicular (V polarization) to the synchrotron orbit and XLD and XAS spectra are measured, as described in Section II.3.3.

XLD is sensitive to the axial anisotropy of the electron DOS induced, in this case, by orbital occupation of the Cu *3d* states. Indeed, when $\boldsymbol{E} \perp c$, transition to states mainly originating from out-of-plane orbitals determine the absorption signal (such as Cu $3d_{3z^2-r^2}$ or O $2p_z$), while those originating from in-plane orbitals are probed with $\boldsymbol{E} \parallel c$ (such as $3d_{x^2-y^2}$ or O $2p_{x,y}$).

For the quantitative analysis of XAS spectra, the isotropic absorption spectrum (XAS_{ISO}) has been obtained as a combination of XAS spectra acquired with vertical (V) and horizontal (H) polarizations:

$$XAS_{ISO} = \left(1 - tan^2(30°)\right) XAS(V, 30°) + \frac{1}{cos^2(30°)} XAS(H, 30°)$$

or equivalently by using *XAS(H,90°)* in place of *XAS(V,30°)*.

XRDs and electrical transport measurements were performed on this set of samples, as shown in Figure III-27 (a) and (b).

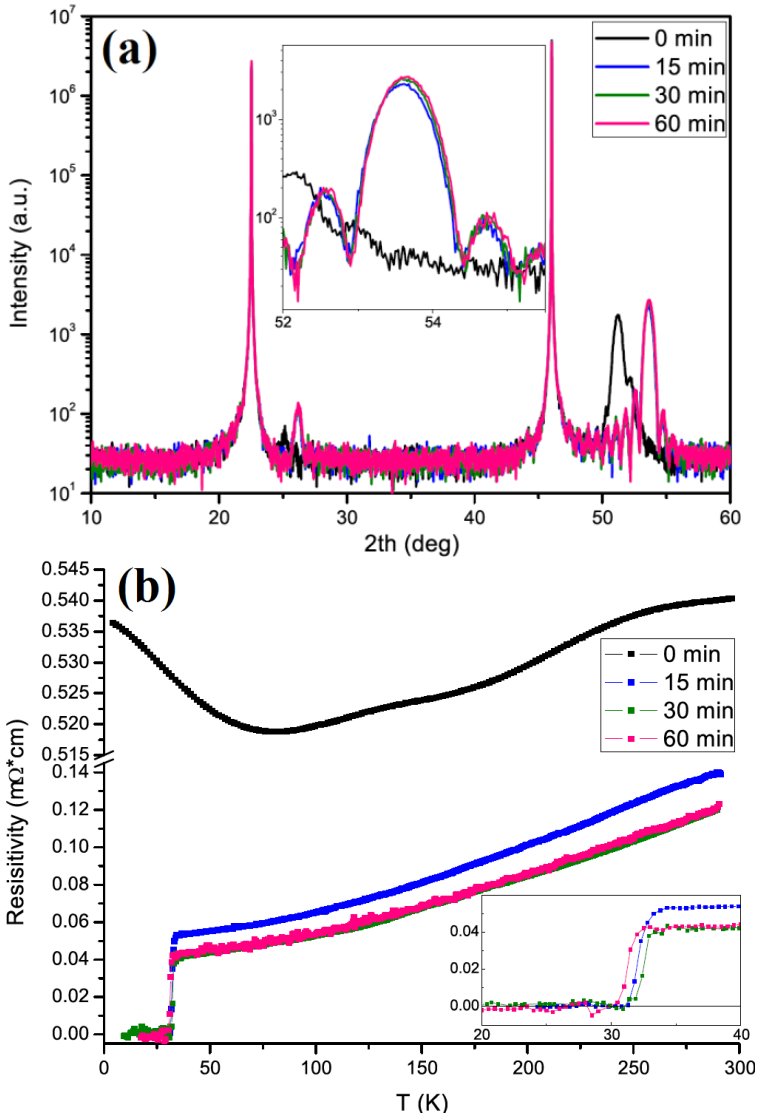

Figure III-27 *(a) XRD spectra as a function of in-situ annealing duration, a zoom of (002) diffraction peak showing a minor variation in the position of the peak for 15-60 min annealed samples is shown in inset; (b) resistivity as a function of the temperature and of annealing of the samples in (a), a zoom of superconductive transition showing that the optimized annealing duration is 30 min is shown in inset*

From XRD spectra (Figure III-27 (a)) of annealed samples an out-of-plane lattice parameter of 0.341 nm is obtained, while the as-grown sample

(0 min) has a maximum corresponding to 0.356 nm and at the same time it is boars with a tail towards higher angles. This suggests that the as-grown sample is characterized by some degree of structural disorder with a distribution of the out-of-plane axis values.

The resistivity of annealed samples are very similar as well as the superconductive critical temperature, as shown in Figure III-27 (b). This suggests that even a shorter annealing is effective in removing most of excess oxygen, even though T_C is optimized by 30 min annealing. The resistivity of the as-grown sample is higher and it is metallic from room temperature down to ≈80 K, where a metal-to-insulator transition is observed.

On this set of samples, XAS measurements have been performed.

A strong absorption is expected at photon energy E = 931.4 eV, corresponding to the $3d^9 \longrightarrow \underline{2p}3d^{10}$ transition ($\underline{2p}$ represents an hole in the *2p* core level), because the majority of Cu ions in SLCO are in the 2+ oxidation state. Together with this main peak, Cu^{2+} is characterized by a weaker peak at E ≈ 936 eV, corresponding to the $\underline{2p}3d^9 4s$ final state (Tanaka et al., (2008)). Upon electron doping, a peak at E ≈ 934 eV has been reported in SLCO that can be attributed to Cu^{1+} $3d^{10} \longrightarrow \underline{2p}3d^{10}4s$ transition (Liu et al., (2001); Tanaka et al., (2008)). States arising from hole introduction, instead, show a peak at E ≈ 932.9 eV and such hole-related states have been reported for hole doped-cuprates (Fink et al., (1994)) and apical-oxygen rich IL compounds $BaCuO_{2+x}$ (Aruta et al., (2008)). Furthermore, a low energy (LE) component 0.4-0.5 eV below the main Cu^{2+} peak (i.e. 931.4 eV) was reported in the XAS measurements of cuprate-manganites interfaces and this was interpreted as originating from a modification of Cu coordination rather than valence modification (Chakhalian et al., (2007); Yang et al., (2012)). In Figure III-28, these known transition-related peaks are highlighted.

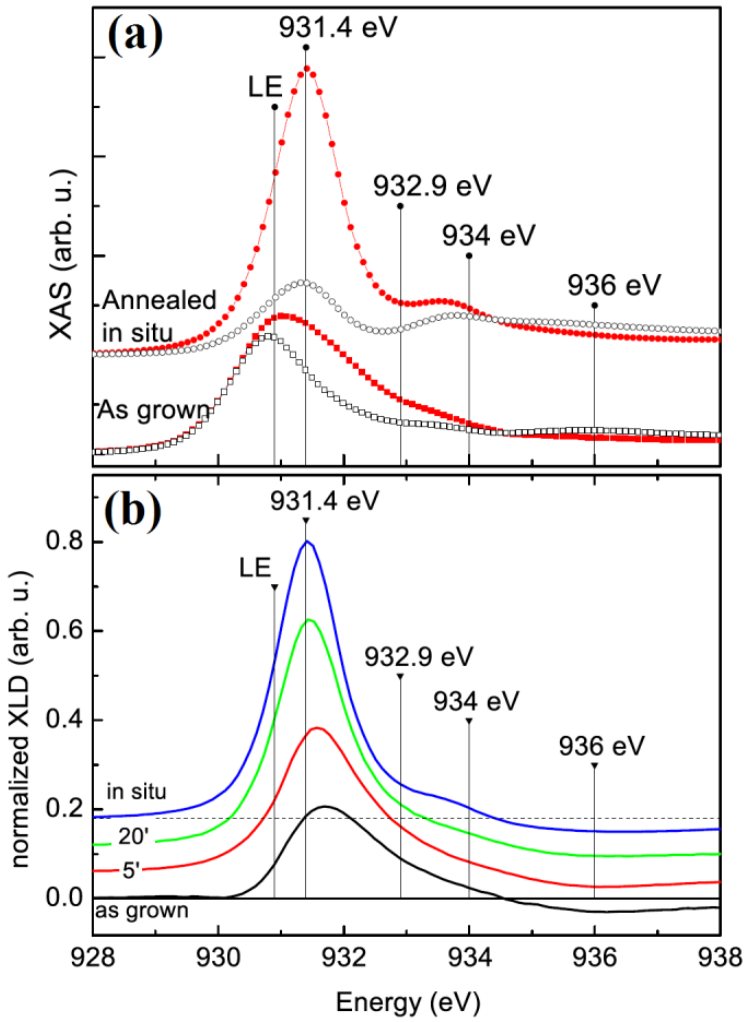

Figure III-28 *(a) XAS Cu L_3 edge spectra with H polarization and incident angle of 90° (red filled symbols) and 30° (black hollow symbols) of the as-grown and in-situ annealed samples; (b) normalized XLD at XAS_{ISO} spectrum of Cu L_3 spectra of the as-grown, 5 min and 20 min Ar annealed and in-situ annealed sample. The spectra are vertically shifted for clarity*

The *in-situ* annealed samples are characterized by a dominant peak corresponding to Cu^{2+} (i.e. 931.4 eV) and a related strong dichroism, as shown in Figure III-28 (a). The peak close to 934 eV can be attributed mainly to electron-doping, while the main peak in the as-grown sample is at 930.9 eV, corresponding to the low energy (LE) component.

The maximum XLD (shown in Figure III-28 (b), normalized to the respective maximum of isotropic XAS spectrum) for the *in-situ* annealed sample is found at the same energy of XAS (i.e. 931.4 eV), while the XLD maximum for the as-grown sample is observable at higher energy and the intensity is strongly reduced and it is broader than the *in-situ* one. As the oxygen is removed from the as-grown samples by annealing in Ar, the XLD spectra change by increasing intensity, reducing broadening and shifting the maximum to a lower energy.

This behavior is more appreciable in Figure III-29 where the energy of XLD maxima and of the isotropic XAS spectra as a function of normalized XLD intensity are shown. While the maximum of isotropic spectra in the oxygen rich samples is at lower energy than the peak of the *in-situ* annealed sample, the XLD maximum exhibits the opposite behavior. For the *in-situ* annealed sample, the maxima are coincident.

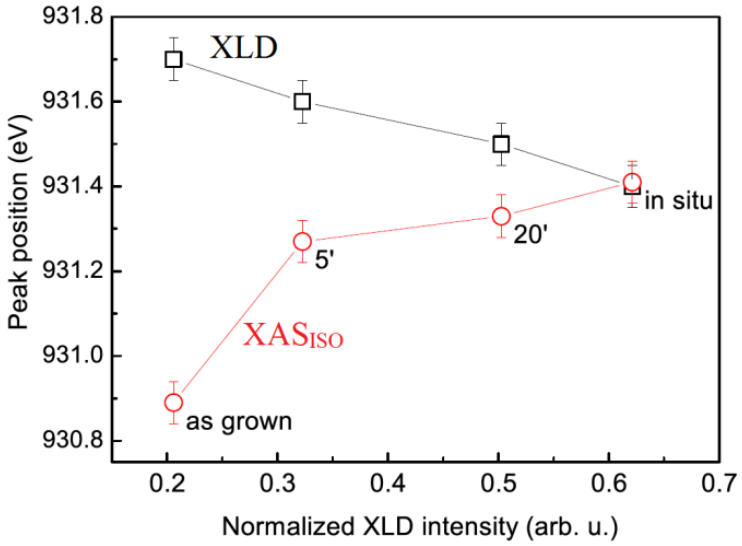

Figure III-29 *Position of the maximum of Cu L_3 XAS_{ISO} (red circles)and XLD (black squares) as a function of the normalized XLD intensity maximum*

The square planar coordination of Cu ions is strongly perturbed by excess oxygen, as can be deduced by comparing the XAS spectra of *in-situ* annealed and as-grown samples (Figure III-28). Oxygen excess also increases the Cu valence, introducing holes in order to balance charges.

The normalized XLD intensity in the as-grown sample is smaller by a factor of 3 with respect to the *in-situ* annealed one. Another signature of a perturbation of the square planar coordination is that the main L_3 peak appears at lower energy in the as-grown sample than the *in-situ* annealed one, as better appreciable in Figure III-29.

The isotropic XAS spectra have been fitted with a sum of Gaussian curves, as explained by (Galdi et al., (2018)). The fit results indicate that the hole component in the as-grown sample is broader than the one observed in the *in-situ* annealed sample, so the metallic behavior of the resistivity as a function of temperature down to ≈ 80 K has been attributed to hole carriers (Figure III-27 (b)).

These samples have also been measured at the O *K* edge that corresponds to the $1s \longrightarrow 2p$ transition (Figure III-30).

The *in-situ* annealed sample shows an increased dichroism compared to the as-grown one and it is particularly relevant in the pre-edge region associated to the hybridization of the oxygen with the Cu *3d* states.

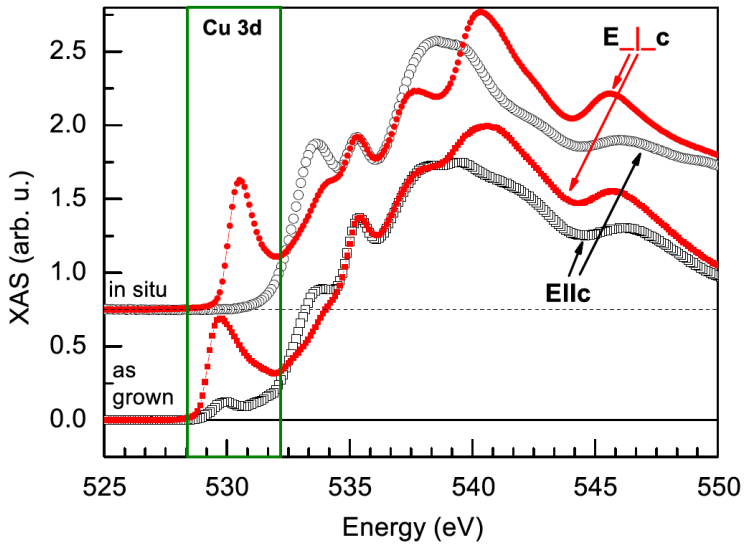

Figure III-30 *Comparison of O K edge XAS spectra of as grown and in-situ annealed samples*

A characteristic feature of electron-doped cuprates is that the pre-edge is only detected with $\boldsymbol{E} \perp c$ as a consequence of orbital occupation and of Cu-O hybridization in plane with O $2p_{x,y}$ orbitals (Fink et al., (1994)), as shown

in the green box in Figure III-30. In particular, for the as-grown sample the non-zero absorption for $\boldsymbol{E} \parallel c$ can be attributed to the presence of apical oxygen holes. Anyway, The O *K* edge XAS of as-grown samples is different from the typical hole-doped cuprates one, despite the presence of hole carriers.

Conclusions

A systematic study of the properties of confined systems, both *n* and *p*-doped, has been done in this dissertation. Evidence of quantum confinement in both the QWs analyzed has been discussed.

It has been observed that in *p*-doped SMO/LSMO/SMO QWs, around room temperature, the metal-to-insulator transition temperature (T_{MI}) is strongly influenced by LSMO thickness values, presenting a sharp drop for the central layer thickness $y < 8$ u.c. This drop is well described in terms of a Ginzburg-Landau approach for systems with a finite size along one direction. Estimation of the critical thickness below which the transition disappears, obtained by fitting the experimental data with eq. III-1, agrees well with previous theoretical evaluations. At low temperature, shallow resistivity minima related to quantum interference effects are observed for the samples whom central layer thicknesses in $5 < y < 15$, while resistivity upturn with a fast increase of resistivity values are observed for $y < 5$ at temperature higher than 150K. These results suggest the presence of spatial charge carrier confinement in the investigated *p*-doped QWs and point out the ability of small gap Mott insulator material, such as SMO, to be successfully used in QWs structures.

A parallel analysis has been done on *n*-doped SCO/SLCO/SCO QWs, in fact the superconducting transition temperature T_C were strongly influenced by the SLCO layer thickness, presenting a sharp drop for $y < 10$ u.c. (where y is the thickness of the central layer also in this case). This drop is well described, also in this case, in terms of a Ginzburg-Landau approach for a clean system with a finite size along one direction, which gives a better agreement to the experimental data than other models based on dirty (disordered) superconducting systems. The normal state sheet resistances of the samples with $3 < y < 20$ present an upturn at relatively low temperatures with a local minimum temperature in the range [50-130] K, close to the typical Néel temperature measured in SLCO. A sharp cross-over from

superconducting to insulating behavior has been observed going from the sample with $y = 4$ u.c. to the one with $y = 3$ u.c., associated to the change in the temperature dependence of the resistivity curves from a $T^{3/2}$ to a $ln(T)$ behavior. Such a change can be traced back, in a quantum interference effect scenario, to a change in the dimensionality of the electronic system. These results suggest the presence, also in these systems, of layering induced spatial charge confinement strongly influencing the electrical transport normal-state properties of the systems.

These results open the way to new developments in the growth of *n* and *p*-doped oxide-based QWs and quantum devices. Furthermore, the relevance of these systems is not only related to the study of their properties as a function of the relative thickness of each layer or to a future development of growing proximate *n-p* doped DQWs, but also the possibility to tune the density of carrier changing the doping level of the central layer.

The behavior of SLCO single layers as a function of doping has been, therefore, analyzed. In particular, the mechanism behind the low temperature resistivity upturn of underdoped samples, which clearly show a metal-to-insulator transition, has been associated to the quantum interference effects. In particular, by suitably fitting the low temperature resistivity curves, the three-dimensional (3D) localization mechanism associated to the electron-phonon scattering was shown to give a better agreement to the experimental data (in terms of χ^2 test) when compared to the two-dimensional (2D) mechanism associated to the logarithmic correction. The occurrence of weak localization effects has been unambiguously proven by low-frequency voltage spectral density measurements, which show a linear dependence of the $1 / f$ noise on the applied bias current at low temperatures, whereas the usual quadratic dependence of the $1 / f$ component occurs in the superconducting and metallic regions.

At high temperature, the analysis of the resistivity has allowed the determination of a non-Fermi liquid metallic phase, which is dominated by a linear temperature dependence of the resistivity for all the investigated samples. While a robust and universal hidden Fermi liquid charge transport in the low temperature properties of the analyzed samples is present. In particular, these last results allow more general investigation of superconducting and normal state properties independently of doping and carrier type. Indeed, values of the sheet resistance coefficients very close to those measured for *p*-doped compounds with the same doping level have been observed, suggesting a universal description of the normal state in cuprates, independently of doping, compound and carrier type.

A further support to these observations is given from the Hall measurements performed on a typical underdoped sample (~7% doped). The cotangent of Hall angle ($\cot(\theta_H)$), disentangled from the logarithmic contribution of the resistivity curve, as a function of temperature has been analyzed. It has been observed that the $\cot(\theta_H)$ has a T^2 ($\cot(\theta_H) \propto C_2 T^2$) dependence up to temperature of about 120K, close to the *T*** value and of the same order of the typical Néel temperature observed in underdoped cuprates. In particular, the slope of the $\cot(\theta_H)$ in this temperature range has a value of C_2 = (0.0262 ± 0.0004) K^{-2}, very close to the universal value found for other *p* and *n*-doped cuprates.

The superconducting properties of SLCO thin films are strongly affected by sample preparation conditions. In particular, a reduction process is needed for all electron doped cuprates in order to get superconductivity, but there is often little control on this step, especially on thin film samples.

Therefore, the optimization of this step is crucial for the quality of SLCO thin films and, consequently, of the *n*-doped QWs based on this compound.

Indeed, what occurs during the reduction process is unclear, but, thanks to X-ray absorption spectroscopy measurements at Cu $L_{2,3}$ and O *K* edges on SLCO thin films with different post-growth treatments, evidence of the modification of Cu coordination and of the density of states at the conduction band have been observed. These are signature of apical oxygen removal during annealing process. In order to obtain these results, different annealing treatments have been performed on the samples. A set of samples has been treated with vacuum annealing *in-situ* post growth of different duration (i.e. 60 min, 30 min, 15 min and 0 min, in particular the last one was cooled down in the same deposition atmosphere of the growth). The 0 min annealed samples, i.e. the "as-grown" sample, after to be measured with XAS, was annealed in Ar for times ranging from 5 to 15 min using a chamber connected to the XAS measurement chamber and measured before and after each annealing step. The results obtained from XAS measurements on SLCO thin films can be a useful reference for future studies of more complex systems, such as the QWs based on this compound.

Bibliography

Abrikosov, A.A., (1988). Fundamentals of the theory of metals. North-Holland, Amsterdam.

Adachi, T., Mori, Y., Takahashi, A., Kato, M., Nishizaki, T., Sasaki, T., Kobayashi, N., Koike, Y., (2013). Evolution of the Electronic State through the Reduction Annealing in Electron-Doped Pr1.3-xLa0.7CexCuO4+δ (x=0.10) Single Crystals: Antiferromagnetism, Kondo Effect, and Superconductivity. J. Phys. Soc. Japan 82, 63713.

Adamo, C., Ke, X., Schiffer, P., Soukiassian, A., Warusawithana, M., Maritato, L., Schlom, D.G., (2008). Electrical and magnetic properties of (SrMnO3)n/(LaMnO3)2n superlattices. Appl. Phys. Lett. 92, 1–3.

Adamo, C., Ke, X., Wang, H.Q., Xin, H.L., Heeg, T., Hawley, M.E., Zander, W., Schubert, J., Schiffer, P., Muller, D.A., Maritato, L., Schlom, D.G., (2009a). Effect of biaxial strain on the electrical and magnetic properties of (001) La0.7Sr0.3MnO3 thin films. Appl. Phys. Lett. 95, 112504.

Adamo, C., Perroni, C.A., Cataudella, V., De Filippis, G., Orgiani, P., Maritato, L., (2009b). Tuning the metal-insulator transitions of (SrMnO3)n/(LaMnO3)2n superlattices: Role of interfaces. Phys. Rev. B 79, 45125.

Ahn, C.H., Bhattacharya, A., Di Ventra, M., Eckstein, J.N., Frisbie, C.D., Gershenson, M.E., Goldman, A.M., Inoue, I.H., Mannhart, J., Millis, A.J., Morpurgo, A.F., Natelson, D., Triscone, J.-M., (2006). Electrostatic modification of novel materials. Rev. Mod. Phys. 78, 1185–1212.

Ahn, C.H., Gariglio, S., Paruch, P., Tybell, T., Antognazza, L., Triscone, J.-M., (1999). Electrostatic Modulation of Superconductivity in Ultrathin GdBa2Cu3O7-x Films. Science 284, 1152–1155.

Ahn, C.H., Triscone, J.-M., Mannhart, J., (2003). Electric field effect in correlated oxide systems. Nature 424, 1015–1018.

Andreakou, P., Poltavtsev, S. V., Leonard, J.R., Calman, E. V., Remeika, M., Kuznetsova, Y.Y., Butov, L. V., Wilkes, J., Hanson, M., Gossard, A.C., (2014). Optically controlled excitonic transistor. Appl. Phys. Lett. 104, 91101.

Armitage, N.P., Fournier, P., Greene, R.L., (2010). Progress and perspective on electron-doped cuprates. Rev. Mod. Phys. 82, 2421.

Aruta, C., Adamo, C., Galdi, A., Orgiani, P., Bisogni, V., Brookes, N.B., Cezar, J.C., Thakur, P., Perroni, C.A., De Filippis, G., Cataudella, V., Schlom, D.G., Maritato, L., Ghiringhelli, G., (2009a). Evolution of magnetic phases and orbital occupation in (SrMnO3)n/(LaMnO3)2n

superlattices. Phys. Rev. B 80, 140405.
Aruta, C., Ghiringhelli, G., Bisogni, V., Braicovich, L., Brookes, N.B., Tebano, A., Balestrino, G., (2009b). Orbital occupation, atomic moments, and magnetic ordering at interfaces of manganite thin films. Phys. Rev. B 80, 14431.
Aruta, C., Ghiringhelli, G., Dallera, C., Fracassi, F., Medaglia, P.G., Tebano, A., Brookes, N.B., Braicovich, L., Balestrino, G., (2008). Hole redistribution across interfaces in superconducting cuprate superlattices. Phys. Rev. B 78, 205120.
Awschalom, D.D., Loss, D., Samarth, N., (2002). Semiconductor Spintronics and Quantum Computation. Springer Berlin Heidelberg.
Bardeen, J., Cooper, L.N., Schrieffer, J.R., (1957). Theory of Superconductivity. Phys. Rev. 108, 1175–1204.
Barišić, N., Chan, M.K., Li, Y., Yu, G., Zhao, X., Dressel, M., Smontara, A., Greven, M., (2013). Universal sheet resistance and revised phase diagram of the cuprate high-temperature superconductors. PNAS 110, 12235–122340.
Barišić, N., Chan, M.K., Veit, M.J., Dorow, C.J., Ge, Y., Tang, Y., Tabis, W., Yu, G., Zhao, X., Greven, M., (2015). Hidden Fermi-liquid behavior throughout the phase diagram of the cuprates.
Barišić, N., Chan, M.K., Veit, M.J., Dorow, C.J., Ge, Y., Tang, Y., Tabis, W., Yu, G., Zhao, X., Greven, M., (2017). Evidence for a universal Fermi-liquid scattering rate throughout the phase diagram of the copper-oxide superconductors.
Barone, C., Adamo, C., Galdi, A., Orgiani, P., Petrov, A.Y., Quaranta, O., Maritato, L., Pagano, S., (2007a). Unusual dependence of resistance and voltage noise on current in La1-xSrxMnO3 ultrathin films. Phys. Rev. B 75, 174431.
Barone, C., Galdi, A., Pagano, S., Quaranta, O., Méchin, L., Routoure, J.-M., Perna, P., (2007b). Experimental technique for reducing contact and background noise in voltage spectral density measurements. Rev. Sci. Instrum. 78, 93905.
Barone, C., Galdi, A., Sacco, C., Orgiani, P., Schlom, D.G., Pagano, S., Maritato, L., (2016). Noise Spectroscopy Investigation of Interplay between Quantum Interference Effects and Superconductivity in Infinite Layer Cuprates. IEEE Trans. Appl. Supercond. 26, 1–4.
Barone, C., Guarino, A., Nigro, A., Romano, A., Pagano, S., (2009). Weak localization and 1/f noise in Nd1.83Ce0.17CuO4+δ thin films. Phys. Rev. B 80, 224405.
Barone, C., Romeo, F., Galdi, A., Orgiani, P., Maritato, L., Guarino, A., Nigro, A., Pagano, S., (2013). Universal origin of unconventional 1/f noise in the weak-localization regime. Phys. Rev. B 87, 245113.
Barone, C., Romeo, F., Pagano, S., Attanasio, C., Carapella, G., Cirillo, C., Galdi, A., Grimaldi, G., Guarino, A., Leo, A., Nigro, A., Sabatino, P.,

(2015). Nonequilibrium fluctuations as a distinctive feature of weak localization. Sci. Rep. 5, 10705.
Beale, T.A.W., Hase, T.P.A., Iida, T., Endo, K., Steadman, P., Marshall, A.R., Dhesi, S.S., van der Laan, G., Hatton, P.D., (2010). RASOR: An advanced instrument for soft x-ray reflectivity and diffraction. Rev. Sci. Instrum. 81, 73904.
Bibes, M., Barthelemy, A., (2007). Oxide Spintronics. IEEE Trans. Electron Devices 54, 1003–1023.
Bibes, M., Villegas, J.E., Barthélémy, A., (2011). Ultrathin oxide films and interfaces for electronics and spintronics. Adv. Phys. 60, 5–84.
Biegalski, M.D., Fong, D.D., Eastman, J.A., Fuoss, P.H., Streiffer, S.K., Heeg, T., Schubert, J., Tian, W., Nelson, C.T., Pan, X.Q., Hawley, M.E., Bernhagen, M., Reiche, P., Uecker, R., Trolier-Mckinstry, S., Schlom, D.G., (2008). Critical thickness of high structural quality SrTiO3 films grown on orthorhombic (101) DyScO3. J. Appl. Phys. 104, 114109.
Boucherit, M., Shoron, O.F., Cain, T.A., Jackson, C.A., Stemmer, S., Rajan, S., (2013). Extreme charge density SrTiO3/GdTiO3 heterostructure field effect transistors. Appl. Phys. Lett. 102, 242909.
Butch, N.P., Jin, K., Kirshenbaum, K., Greene, R.L., Paglione, J., (2012). Quantum critical scaling at the edge of Fermi liquid stability in a cuprate superconductor. Proc. Natl. Acad. Sci. U. S. A. 109, 8440–4.
Butov, L. V., Lai, C.W., Ivanov, A.L., Gossard, A.C., Chemla, D.S., (2002). Towards Bose–Einstein condensation of excitons in potential traps. Nature 417, 47–52.
Carra, P., Thole, B.T., Altarelli, M., Wang, X., (1993). X-ray circular dichroism and local magnetic fields. Phys. Rev. Lett. 70, 694–697.
Cen, C., Thiel, S., Mannhart, J., Levy, J., (2009). Oxide nanoelectronics on demand. Science 323, 1026–30.
Chakhalian, J., Freeland, J.W., Habermeier, H.-U., Cristiani, G., Khaliullin, G., van Veenendaal, M., Keimer, B., (2007). Orbital reconstruction and covalent bonding at an oxide interface. Science 318, 1114–7.
Chan, M.K., Veit, M.J., Dorow, C.J., Ge, Y., Li, Y., Tabis, W., Tang, Y., Zhao, X., Barišić, N., Greven, M., (2014). In-Plane Magnetoresistance Obeys Kohler's Rule in the Pseudogap Phase of Cuprate Superconductors. Phys. Rev. Lett. 113, 177005.
Chen, C.T., Idzerda, Y.U., Lin, H.-J., Smith, N. V., Meigs, G., Chaban, E., Ho, G.H., Pellegrin, E., Sette, F., (1995). Experimental Confirmation of the X-Ray Magnetic Circular Dichroism Sum Rules for Iron and Cobalt. Phys. Rev. Lett. 75, 152–155.
Coey, J.M.D., Viret, M., Ranno, L., Ounadjela, K., (1995). Electron Localization in Mixed-Valence Manganites. Phys. Rev. Lett. 75, 3910–3913.

Coey, J.M.D., Viret, M., von Molnár, S., (1999). Mixed-valence manganites. Adv. Phys. 48, 167–293.
Conduit, G.J., Conlon, P.H., Simons, B.D., (2008). Superfluidity at the BEC-BCS crossover in two-dimensional Fermi gases with population and mass imbalance. Phys. Rev. A 77, 53617.
Croxall, A.F., (2010). Towards the ground state of an electron-hole bilayer: a low temperature transport based approach. University of Cambridge.
Dagotto, E., Hotta, T., Moreo, A., (2001). Colossal magnetoresistant materials: the key role of phase separation. Phys. Rep. 344, 1–153.
Feenstra, R., Li, X., Kanai, M., Kawai, T., Kawai, S., Budai, J.D., Jones, E.C., Sun, Y.R., Thompson, J.R., Pennycook, S.J., Christen, D.K., (1994). Electron-doped and hole-doped infinite layer Sr1−xCuO2−δ films grown by laser molecular beam epitaxy. Phys. C Supercond. 224, 300–316.
Fink, J., Nücker, N., Pellegrin, E., Romberg, H., Alexander, M., Knupfer, M., (1994). Electron energy-loss and x-ray absorption spectroscopy of cuprate superconductors and related compounds. J. Electron Spectros. Relat. Phenomena 66, 395–452.
Fink, J., Schierle, E., Weschke, E., Geck, J., (2013). Resonant elastic soft x-ray scattering. Reports Prog. Phys. 76, 56502.
Finkel'stein, A.M., (1994). Suppression of superconductivity in homogeneously disordered systems. Phys. B Condens. Matter 197, 636–648.
Fournier, P., (2015). T′ and infinite-layer electron-doped cuprates. Phys. C Supercond. its Appl. 514, 314–338.
Galdi, A., Aruta, C., Orgiani, P., Adamo, C., Bisogni, V., Brookes, N.B., Ghiringhelli, G., Schlom, D.G., Thakur, P., Maritato, L., (2012). Electronic band redistribution probed by oxygen absorption spectra of (SrMnO 3)n(LaMnO 3) 2n superlattices. Phys. Rev. B 85, 125129.
Galdi, A., Orgiani, P., Sacco, C., Gobaut, B., Torelli, P., Aruta, C., Brookes, N.B., Minola, M., Harter, J.W., Shen, K.M., Schlom, D.G., Maritato, L., (2018). X-ray absorption spectroscopy study of annealing process on $Sr_{1-x}La_xCuO_2$ electron-doped cuprate thin films. J. Appl. Phys. 123, 123901.
Galdi, A., Sacco, C., Orgiani, P., Romeo, F., Maritato, L., (2017). Growth and characterization of charge carrier spatially confined SrMnO3/La0.7Sr0.3MnO3/SrMnO3 trilayers. J. Cryst. Growth 459, 56–60.
Gao, Y., Cao, G., Zhang, J., Habermeier, H.-U., (2012). Intrinsic and precipitate-induced quantum corrections to conductivity in La2/3Sr1/3MnO3 thin films. Phys. Rev. B 85, 195128.
Gilbert, B., Frazer, B.H., Belz, A., Conrad, P.G., Nealson, K.H., Haskel, D., Lang, J.C., Srajer, G., De Stasio, G., (2003). Multiple Scattering Calculations of Bonding and X-ray Absorption Spectroscopy of

Manganese Oxides. J. Phys. Chem. A 107, 2839–2847.
Goldschmidt, V.M., (1958). Geochemistry. Clarendon Press, Oxford.
Goodenough, J.B., (1955). Theory of the Role of Covalence in the Perovskite-Type Manganites [La,M(II)]MnO3. Phys. Rev. 100, 564–573.
Gozar, A., Logvenov, G., Kourkoutis, L.F., Bollinger, A.T., Giannuzzi, L.A., Muller, D.A., Bozovic, I., (2008). High-temperature interface superconductivity between metallic and insulating copper oxides. Nature 455, 782–785.
Grosso, G., Graves, J., Hammack, A.T., High, A.A., Butov, L. V., Hanson, M., Gossard, A.C., (2009). Excitonic switches operating at around 100 K. Nat. Photonics 3, 577–580.
Gurvitch, M., Fiory, A.T., (1987). Resistivity of La1.825Sr0.175CuO4 and YBa2Cu3O7 to 1100 K: Absence of saturation and its implications. Phys. Rev. Lett. 59, 1337–1340.
Haeni, J.H., Theis, C.D., Schlom, D.G., (2000). RHEED Intensity Oscillations for the Stoichiometric Growth of SrTiO3 Thin Films by Reactive Molecular Beam Epitaxy. J. Electroceramics 4, 385–391.
Hagen, S.J., Xu, X.Q., Jiang, W., Peng, J.L., Li, Z.Y., Greene, R.L., Xu, Q., Jiang, W., Peng, J.L., Li, Z.Y., Greene, R.L., (1992). Transport and localization in Nd2-xCexCuO4-y. Phys. Rev. B 45, 515(R).
Harter, J.W., (2013). ANGLE-RESOLVED PHOTOEMISSION SPECTROSCOPY OF Sr 1 − x La x CuO 2 THIN FILMS GROWN BY MOLECULAR-BEAM EPITAXY.
Harter, J.W., Maritato, L., Shai, D.E., Monkman, E.J., Nie, Y., Schlom, D.G., Shen, K.M., (2012). Nodeless superconducting phase arising from a strong (pi, pi) antiferromagnetic phase in the infinite-layer electron-doped Sr 1-xLaxCuO2 compound. Phys. Rev. Lett. 109, 267001.
Harter, J.W., Maritato, L., Shai, D.E., Monkman, E.J., Nie, Y., Schlom, D.G., Shen, K.M., (2015). Doping evolution and polar surface reconstruction of the infinite-layer cuprate Sr 1−x La x CuO 2. Phys. Rev. B 92, 35149.
Herman, M.A., (1982). Physical problems concerning effusion processes of semiconductors in molecular beam epitaxy. Vacuum 32, 555–565.
High, A.A., Hammack, A.T., Butov, L. V., Hanson, M., Gossard, A.C., (2007). Exciton optoelectronic transistor. Opt. Lett. 32, 2466.
High, A.A., Novitskaya, E.E., Butov, L. V, Hanson, M., Gossard, A.C., (2008). Control of exciton fluxes in an excitonic integrated circuit. Science 321, 229–31.
Hubbard, J., (1963). Electron Correlations in Narrow Energy Bands. Proc. R. Soc. A Math. Phys. Eng. Sci. 276, 238–257.
Ideguchi, T., Yoshioka, K., Mysyrowicz, A., Kuwata-Gonokami, M., (2008).

Coherent Quantum Control of Excitons at Ultracold and High Density in Cu2O with Phase Manipulated Pulses. Phys. Rev. Lett. 100, 233001.
Imada, M., Fujimori, A., Tokura, Y., (1998). Metal-insulator transitions. Rev. Mod. Phys. 70, 1039–1263.
Jackson, C.A., Zhang, J.Y., Freeze, C.R., Stemmer, S., (2014). Quantum critical behaviour in confined SrTiO3 quantum wells embedded in antiferromagnetic SmTiO3. Nat. Commun. 5, 1.
Jalan, B., Engel-Herbert, R., Wright, N.J., Stemmer, S., (2009). Growth of high-quality SrTiO3 films using a hybrid molecular beam epitaxy approach. J. Vac. Sci. Technol. A Vacuum, Surfaces, Film. 27, 461–464.
Jiang, W., Peng, J.L., Li, Z.Y., Greene, R.L., (1993). Transport properties of Nd1.85Ce0.15CuO4+δ crystals before and after reduction. Phys. Rev. B 47, 8151–8155.
Jin, K., Butch, N.P., Kirshenbaum, K., Paglione, J., Greene, R.L., (2011). Link between spin fluctuations and electron pairing in copper oxide superconductors. Nature 476, 73–75.
Jin, K., Zhang, X.H., Bach, P., Greene, R.L., (2009). Evidence for antiferromagnetic order in La2−xCexCuO4 from angular magnetoresistance measurements. Phys. Rev. B 80, 12501.
Jin, S., Tiefel, T.H., McCormack, M., Fastnacht, R.A., Ramesh, R., Chen, L.H., (1994). Thousandfold Change in Resistivity in Magnetoresistive La-Ca-Mn-O Films. Science 264, 413–415.
Jonker, G.H., Van Santen, J.H., (1950). Ferromagnetic compounds of manganese with perovskite structure. Physica 16, 337–349.
Kamada, H., Gotoh, H., (2004). Quantum computation with quantum dot excitons. Semicond. Sci. Technol. 19, S392–S396.
Kang, H.J., Dai, P., Campbell, B.J., Chupas, P.J., Rosenkranz, S., Lee, P.L., Huang, Q., Li, S., Komiya, S., Ando, Y., (2007). Microscopic annealing process and its impact on superconductivity in T′-structure electron-doped copper oxides. Nat. Mater. 6, 224–229.
Karimoto, S., Naito, M., (2004). Electron-doped infinite-layer thin films with TC over 40 K grown on DyScO3 substrates. Appl. Phys. Lett. 84, 2136–2138.
Keimer, B., Kivelson, S.A., Norman, M.R., Uchida, S., Zaanen, J., (2015). From quantum matter to high-temperature superconductivity in copper oxides. Nature 518, 179–186.
Keldysh, L. V, Kopaev, Y.E., (1965). Possible instability of the semimetallic state toward coulomb interaction. Sov. Phys. Solid State 6, 2219–2224.
Keldysh, L. V, Kozlov, A.N., (1968). Collective Properties of Excitons in Semiconductors. Sov. Physic JETP 27, 521–528.
Kennett, M.P., McKenzie, R.H., (2008). Quantum interference and weak localization effects in the interlayer magnetoresistance of layered

metals. Phys. Rev. B 78, 24506.
Kikkawa, J.M., Awschalom, D.D., (1998). Resonant Spin Amplification in n -Type GaAs. Phys. Rev. Lett. 80, 4313–4316.
Kikkawa, J.M., Smorchkova, I.P., Samarth, N., Awschalom, D.D., (1997). Room-Temperature Spin Memory in Two-Dimensional Electron Gases. Science 277, 1284–1287.
Kim, H.M., Kim, U., Park, C., Kwon, H., Char, K., (2016). Thermally stable pn-junctions based on a single transparent perovskite semiconductor BaSnO3. APL Mater. 4, 56105.
Kittel, C., (2005). Introduction to solid state physics. Wiley.
Kogan, S., (1996). Electronic noise and fluctuations in solids. Cambridge University Press.
Kumar, D., Sankar, J., Narayan, J., Singh, R.K., Majumdar, A.K., (2002). Low-temperature resistivity minima in colossal magnetoresistive La0.7Ca0.3MnO3 thin films. Phys. Rev. B 65, 94407.
Ladd, T.D., Jelezko, F., Laflamme, R., Nakamura, Y., Monroe, C., O'Brien, J.L., (2010). Quantum computers. Nature 464, 45–53.
Lee, P.A., Ramakrishnan, T. V., (1985). Disordered electronic systems. Rev. Mod. Phys. 57, 287–337.
Leggett, A.J., (2006). What DO we know about high T c? Nat. Phys. 2, 134–136.
Li, Q.-R., Major, M., Yazdi, M.B., Donner, W., Dao, V.H., Mercey, B., Lüders, U., (2015). Dimensional crossover in ultrathin buried conducting SrVO3 layers. Phys. Rev. B 91, 35420.
Li, Y., Balédent, V., Barišić, N., Cho, Y., Fauqué, B., Sidis, Y., Yu, G., Zhao, X., Bourges, P., Greven, M., (2008). Unusual magnetic order in the pseudogap region of the superconductor HgBa2CuO4+δ. Nature 455, 372–375.
Li, Y., Tabis, W., Yu, G., Barišić, N., Greven, M., (2016). Hidden Fermi-liquid Charge Transport in the Antiferromagnetic Phase of the Electron-Doped Cuprate Superconductors. Phys. Rev. Lett. 117, 197001.
Li, Z.Z., Jovanovic, V., Raffy, H., Megtert, S., (2009). Influence of oxygen reduction on the structural and electronic properties of electron-doped Sr1−xLaxCuO2 thin films. Phys. C Supercond. 469, 73–81.
Littlewood, P.B., Zhu, X., (1996). Possibilities for exciton condensation in semiconductor quantum-well structures. Phys. Scr. 1996, 56–67.
Liu, R.S., Chen, J.M., Nachimuthu, P., Gundakaram, R., Jung, C.U., Kim, J.Y., Lee, S.I., (2001). Evidence for electron-doped (n-type) superconductivity in the infinite-layer (Sr0.9La0.1)CuO2 compound by X-ray absorption near-edge spectroscopy. Solid State Commun. 118, 367–370.
Liu, Y., McGreer, K.A., Nease, B., Haviland, D.B., Martinez, G., Halley,

J.W., Goldman, A.M., (1991). Scaling of the insulator-to-superconductor transition in ultrathin amorphous Bi films. Phys. Rev. Lett. 67, 2068–2071.

Loss, D., DiVincenzo, D.P., (1998). Quantum computation with quantum dots. Phys. Rev. A 57, 120–126.

Lu, Y., Li, X.W., Gong, G.Q., Xiao, G., Gupta, A., Lecoeur, P., Sun, J.Z., Wang, Y.Y., Dravid, V.P., (1996). Large magnetotunneling effect at low magnetic fields in micrometer-scale epitaxial La0.67Sr0.33MnO3 tunnel junctions. Phys. Rev. B 54, R8357–R8360.

Mannhart, J., Schlom, D.G., (2010). Oxide Interfaces-An Opportunity for Electronics. Science 327, 1607–1611.

Maritato, L., Adamo, C., Barone, C., De Luca, G.M., Galdi, A., Orgiani, P., Petrov, A.Y., (2006). Low-temperature resistivity of La0.7Sr0.3MnO3 ultra thin films: Role of quantum interference effects. Phys. Rev. B 73, 94456.

Maritato, L., Galdi, A., Orgiani, P., Harter, J.W., Schubert, J., Shen, K.M., Schlom, D.G., (2013). Layer-by-layer shuttered molecular-beam epitaxial growth of superconducting Sr 1– x La x CuO 2 thin films. J. Appl. Phys. 113, 53911.

Maurel, L., Marcano, N., Prokscha, T., Langenberg, E., Blasco, J., Guzmán, R., Suter, A., Magén, C., Morellón, L., Ibarra, M.R., Pardo, J.A., Algarabel, P.A., (2015). Nature of antiferromagnetic order in epitaxially strained multiferroic SrMnO3 thin films. Phys. Rev. B 92, 24419.

Mercone, S., Perroni, C.A., Cataudella, V., Adamo, C., Angeloni, M., Aruta, C., De Filippis, G., Miletto, F., Oropallo, A., Perna, P., Petrov, A.Y., Scotti di Uccio, U., Maritato, L., (2005). Transport properties in manganite thin films. Phys. Rev. B 71, 64415.

Millis, A.J., Schlom, D.G., (2010). Electron-hole liquids in transition-metal oxide heterostructures. Phys. Rev. B 82, 73101.

Mirzaei, S.I., Stricker, D., Hancock, J.N., Berthod, C., Georges, A., van Heumen, E., Chan, M.K., Zhao, X., Li, Y., Greven, M., Barišić, N., van der Marel, D., (2013). Spectroscopic evidence for Fermi liquid-like energy and temperature dependence of the relaxation rate in the pseudogap phase of the cuprates. Proc. Natl. Acad. Sci. U. S. A. 110, 5774–8.

Moetakef, P., Cain, T.A., Ouellette, D.G., Zhang, J.Y., Klenov, D.O., Janotti, A., Van de Walle, C.G., Rajan, S., Allen, S.J., Stemmer, S., (2011). Electrostatic carrier doping of GdTiO3/SrTiO3 interfaces. Appl. Phys. Lett. 99, 232116.

Moetakef, P., Jackson, C.A., Hwang, J., Balents, L., Allen, S.J., Stemmer, S., (2012a). Toward an artificial Mott insulator: Correlations in confined high-density electron liquids in SrTiO 3. Phys. Rev. B 86, 201102.

Moetakef, P., Williams, J.R., Ouellette, D.G., Kajdos, A.P., Goldhaber-

Gordon, D., Allen, S.J., Stemmer, S., (2012b). Carrier-Controlled Ferromagnetism in SrTiO3. Phys. Rev. X 2, 21014.
Monkman, E.J., Adamo, C., Mundy, J. a., Shai, D.E., Harter, J.W., Shen, D., Burganov, B., Muller, D.A., Schlom, D.G., Shen, K.M., (2012). Quantum many-body interactions in digital oxide superlattices. Nat. Mater. 11, 855–859.
Mott N.F., (1990). Metal-insulator transition. Taylor&Francis, London.
Mukhopadhyay, S., Das, I., (2009). Low temperature conductivity in ferromagnetic manganite thin films: quantum corrections and inter-granular transport. J. Phys. Condens. Matter 21, 186004.
Nanda, B.R.K., Satpathy, S., (2009). Electronic and magnetic structure of the (LaMnO3)2n/(SrMnO3)n superlattices. Phys. Rev. B 79, 54428.
Niu, W., Gao, M., Wang, X., Song, F., Du, J., Wang, X., Xu, Y., Zhang, R., (2016). Evidence of weak localization in quantum interference effects observed in epitaxial La0.7Sr0.3MnO3 ultrathin films. Sci. Rep. 6, 26081.
Odoh, E.O., Njapba, A.S., (2015). A Review of Semiconductor Quantum Well Devices. Adv. Phys. Theor. Appl. 46, 26–32.
Ohtomo, A., Hwang, H.Y., (2004). A high-mobility electron gas at the LaAlO3/SrTiO3 heterointerface. Nature 427, 423–427.
Ohtomo, A., Muller, D.A., Grazul, J.L., Hwang, H.Y., (2002). Artificial charge-modulationin atomic-scale perovskite titanate superlattices. Nature 419, 378–380.
Okamoto, S., Millis, A.J., (2004). Theory of Mott insulator–band insulator heterostructures. Phys. Rev. B 70, 75101.
Onose, Y., Taguchi, Y., Ishizaka, K., Tokura, Y., (2001). Doping Dependence of Pseudogap and Related Charge Dynamics in Nd2-xCexCuO4. Phys. Rev. Lett. 87, 217001.
Orgiani, P., Adamo, C., Barone, C., Galdi, A., Petrov, A.Y., Schlom, D.G., Maritato, L., (2007a). Influence of a single disorder parameter on the conduction mechanisms in manganite thin films. Phys. Rev. B 76, 12404.
Orgiani, P., Aruta, C., Balestrino, G., Born, D., Maritato, L., Medaglia, P.G., Stornaiuolo, D., Tafuri, F., Tebano, A., (2007b). Direct measurement of sheet resistance Rsq in cuprate systems: Evidence of a fermionic scenario in a metal-insulator transition. Phys. Rev. Lett. 98, 36401.
Orgiani, P., Galdi, · A, Sacco, · C, Arpaia, · R, Charpentier, · S, Lombardi, · F, Barone, · C, Pagano, · S, Schlom, · D G, Maritato, · L, Galdi, A., Sacco, C., Arpaia, R., Charpentier, S., Lombardi, F., Barone, C., Pagano, S., Schlom, D.G., Maritato, L., (2015). The Role of Quantum Interference Effects in Normal-State Transport Properties of Electron-Doped Cuprates. J. Supercond. Nov. Magn. 28, 3481–3486.
Orgiani, P., Galdi, A., Sacco, C., Arpaia, R., Charpentier, S., Lombardi, F.,

Barone, C., Pagano, S., Schlom, D.G., Maritato, L., (2015). The Role of Quantum Interference Effects in Normal-State Transport Properties of Electron-Doped Cuprates. J. Supercond. Nov. Magn. 28, 3481–3486.

Orgiani, P., Petrov, A.Y., Adamo, C., Aruta, C., Barone, C., De Luca, G.M., Galdi, A., Polichetti, M., Zola, D., Maritato, L., (2006). In-plane anisotropy in the magnetic and transport properties of manganite ultrathin films. Phys. Rev. B 74, 134419.

Panaccione, G., Vobornik, I., Fujii, J., Krizmancic, D., Annese, E., Giovanelli, L., Maccherozzi, F., Salvador, F., De Luisa, A., Benedetti, D., Gruden, A., Bertoch, P., Polack, F., Cocco, D., Sostero, G., Diviacco, B., Hochstrasser, M., Maier, U., Pescia, D., Back, C.H., Greber, T., Osterwalder, J., Galaktionov, M., Sancrotti, M., Rossi, G., (2009). Advanced photoelectric effect experiment beamline at Elettra: A surface science laboratory coupled with Synchrotron Radiation. Rev. Sci. Instrum. 80, 43105.

Petrov, A.Y., Aruta, C., Mercone, S., Adamo, C., Alessandri, I., Maritato, L., (2004). Room temperature metal–insulator transition in as grown (La −xSrx)yMnO3 thin films deposited by molecular beam epitaxy. Eur. Phys. J. B 40, 11–17.

Pickett, W.E., Singh, D.J., (1996). Electronic structure and half-metallic transport in the La1−xCaxMnO3 system. Phys. Rev. B 53, 1146–1160.

Pieri, P., Neilson, D., Strinati, G.C., (2007). Effects of density imbalance on the BCS-BEC crossover in semiconductor electron-hole bilayers. Phys. Rev. B 75, 113301.

Popovic, Z. V., Ivanov, V.A., Konstantinovic, M.J., Cantarero, A., Martinez-Pastor, J., Olguin, D., Alonso, M.I., Garriga, M., Khuong, O.P., Vietkin, A., Moshchalkov, V. V., (2001). Optical studies of gap, hopping energies and the Anderson-Hubbard parameter in the zigzag-chain compound SrCuO2. Phys. Rev. B 63, 165105.

Ramirez, A.P., (1997). Colossal magnetoresistance. J. Phys. Condens. Matter 9, 8171–8199.

Ravindran, P., Kjekshus, A., Fjellvåg, H., Delin, A., Eriksson, O., (2002). Ground-state and excited-state properties of LaMnO3 from full-potential calculations. Phys. Rev. B 65, 64445.

Reyren, N., Bibes, M., Lesne, E., George, J.-M., Deranlot, C., Collin, S., Barthélémy, A., Jaffrès, H., (2012). Gate-Controlled Spin Injection at LaAlO3/SrTiO3 Interfaces. Phys. Rev. Lett. 108, 186802.

Richard, P., Neupane, M., Xu, Y.-M., Fournier, P., Li, S., Dai, P., Wang, Z., Ding, H., (2007). Competition between Antiferromagnetism and Superconductivity in the Electron-Doped Cuprates Triggered by Oxygen Reduction. Phys. Rev. Lett. 99, 157002.

Richard, P., Riou, G., Hetel, I., Jandl, S., Poirier, M., Fournier, P., (2004). Role of oxygen nonstoichiometry and the reduction process on the

local structure of Nf2-xCexCuO4±δ. Phys. Rev. B 70, 64513.
Rullier-Albenque, F., Alloul, H., Tourbot, R., (2001). Disorder and Transport in Cuprates: Weak Localization and Magnetic Contributions. Phys. Rev. Lett. 87, 157001.
Rybicki, D., Jurkutat, M., Reichardt, S., Kapusta, C., Haase, J., (2016). Perspective on the phase diagram of cuprate high-temperature superconductors. Nat. Commun. 7, 11413.
Salluzzo, M., (2015). Electronic Reconstruction at the Interface Between Band Insulating Oxides: The LaAlO3/SrTiO3 System. In: Oxide Thin Films, Multilayers, and Nanocomposites. Springer International Publishing, Cham, pp. 181–211.
Santos, T.S., Kirby, B.J., Kumar, S., May, S.J., Borchers, J.A., Maranville, B.B., Zarestky, J., te Velthuis, S.G.E., van den Brink, J., Bhattacharya, A., (2011). Delta Doping of Ferromagnetism in Antiferromagnetic Manganite Superlattices. Phys. Rev. Lett. 107, 167202.
Schlom, D.G., Haeni, J.H., Lettieri, J., Theis, C.D., Tian, W., Jiang, J.C., Pan, X.Q., (2001). Oxide nano-engineering using MBE. Mater. Sci. Eng. B 87, 282–291.
Sekitani, T., Naito, M., Miura, N., (2003). Kondo effect in underdoped n-type superconductors. Phys. Rev. B 67, 174503.
Shekhter, A., Ramshaw, B.J., Liang, R., Hardy, W.N., Bonn, D.A., Balakirev, F.F., McDonald, R.D., Betts, J.B., Riggs, S.C., Migliori, A., (2013). Bounding the pseudogap with a line of phase transitions in YBa2Cu3O6+δ. Nature 498, 75–77.
Simonin, J., (1986). Surface term in the superconductive Ginzburg-Landau free energy: Application to thin films. Phys. Rev. B 33, 7830–7832.
Søndenå, R., Ravindran, P., Stølen, S., Grande, T., Hanfland, M., (2006). Electronic structure and magnetic properties of cubic and hexagonal SrMnO 3. Phys. Rev. B 74, 144102.
Stemmer, S., Millis, A.J., (2013). Quantum confinement in transition metal oxide quantum wells. MRS Bull. 38, 1032–1039.
Stornaiuolo, D., Cantoni, C., De Luca, G.M., Di Capua, R., Di. Gennaro, E., Ghiringhelli, G., Jouault, B., Marrè, D., Massarotti, D., Miletto Granozio, F., Pallecchi, I., Piamonteze, C., Rusponi, S., Tafuri, F., Salluzzo, M., (2016). Tunable spin polarization and superconductivity in engineered oxide interfaces. Nat. Mater. 15, 278–283.
Stornaiuolo, D., Massarotti, D., Di Capua, R., Lucignano, P., Pepe, G.P., Salluzzo, M., Tafuri, F., (2017). Signatures of unconventional superconductivity in the LaAlO3/SrTiO3 two-dimensional system. Phys. Rev. B 95, 140502.
Tanaka, Y., Karppinen, M., Lee, J.M., Liu, R.S., Chen, J.M., Yamauchi, H., (2008). Systematic Cu L2,3-edge and O K-edge XANES spectroscopy study on the infinite-layer superconductor system, (Sr,La)CuO2. Solid

State Commun. 147, 370–373.
Tanda, S., Honma, M., Nakayama, T., (1991). Critical sheet resistance observed in high-T, oxide-superconductor Nd2-xCexCu04 thin films. Phys. Rev. B 43, 8725–8728.
Thiel, S., Hammerl, G., Schmehl, A., Schneider, C.W., Mannhart, J., (2006). Tunable Quasi-Two-Dimensional Electron Gases in Oxide Heterostructures. Science 313, 1942–1945.
Thole, B.T., Carra, P., Sette, F., van der Laan, G., (1992). X-ray circular dichroism as a probe of orbital magnetization. Phys. Rev. Lett. 68, 1943–1946.
Timofeev, V.B., Larionov, A. V., Ioselevich, A.S., Zeman, J., Martinez, G., Hvam, J., Soerensen, K., (1998). Interwell radiative recombination in the presence of random potential fluctuations in GaAs/AlGaAs biased double quantum wells. J. Exp. Theor. Phys. Lett. 67, 613–620.
Van der Pauw, I.J., (1958). A method of measuring specific resistivity and Hall effect of discs of arbitrary shape. Philips Res. Reports 13, 1–9.
Van Hove, J.M., Lent, C.S., Pukite, P.R., Cohen, P.I., (1983). Damped oscillations in reflection high energy electron diffraction during GaAs MBE. J. Vac. Sci. Technol. B Microelectron. Nanom. Struct. 1, 741.
von Helmolt, R., Wecker, J., Holzapfel, B., Schultz, L., Samwer, K., (1993). Giant negative magnetoresistance in perovskitelike La2/3Ba1/3MnOx ferromagnetic films. Phys. Rev. Lett. 71, 2331–2333.
Wang, C., Jin, K., Gu, L., Lu, H., Li, S., Zhou, W., Zhao, R., Guo, H., He, M., Yang, G., (2014). Magnetoelectric transport and quantum interference effect in ultrathin manganite films. Appl. Phys. Lett. 104, 162405.
Wang, Y.-L., Huang, Y., Shan, L., Li, S.L., Dai, P., Ren, C., Wen, H.-H., (2009). Annealing effect on the electron-doped superconductor Pr0.88LaCe0.12CuO4±δ. Phys. Rev. B 80, 94513.
Wolf, S.A., Awschalom, D.D., Buhrman, R.A., Daughton, J.M., von Molnár, S., Roukes, M.L., Chtchelkanova, A.Y., Treger, D.M., (2001). Spintronics: a spin-based electronics vision for the future. Science 294, 1488–95.
Yang, N., Di Castro, D., Aruta, C., Mazzoli, C., Minola, M., Brookes, N.B., Moretti Sala, M., Prellier, W., Lebedev, O.I., Tebano, A., Balestrino, G., (2012). Charge localization at the interface between La1−xSrxMnO3 and the “infinite layers” cuprate CaCuO2. J. Appl. Phys. 112, 123901.
Yoshimatsu, K., Horiba, K., Kumigashira, H., Yoshida, T., Fujimori, A., Oshima, M., (2011). Metallic quantum well states in artificial structures of strongly correlated oxide. Science 333, 319–22.
Yoshimatsu, K., Okabe, T., Kumigashira, H., Okamoto, S., Aizaki, S., Fujimori, A., Oshima, M., (2010). Dimensional-Crossover-Driven Metal-Insulator Transition in SrVO3 Ultrathin Films. Phys. Rev. Lett.

104, 147601.
Yoshimatsu, K., Sakai, E., Kobayashi, M., Horiba, K., Yoshida, T., Fujimori, A., Oshima, M., Kumigashira, H., (2013). Determination of the surface and interface phase shifts in metallic quantum well structures of perovskite oxides. Phys. Rev. B 88, 115308.
Zaanen, J., Sawatzky, G.A., Allen, J.W., (1985). Band gaps and electronic structure of transition-metal compounds. Phys. Rev. Lett. 55, 418–421.
Zener, C., (1951). Interaction between the d-Shells in the Transition Metals. II. Ferromagnetic Compounds of Manganese with Perovskite Structure. Phys. Rev. 82, 403–405.
Zhang, J.Y., Hwang, J., Raghavan, S., Stemmer, S., (2013). Symmetry Lowering in Extreme-Electron-Density Perovskite Quantum Wells. Phys. Rev. Lett. 110, 256401.
Zhang, J.Y., Jackson, C.A., Chen, R., Raghavan, S., Moetakef, P., Balents, L., Stemmer, S., (2014). Correlation between metal-insulator transitions and structural distortions in high-electron-density SrTiO3 quantum wells. Phys. Rev. B 89, 75140.
Zhu, X., Littlewood, P.B., Hybertsen, M.S., Rice, T.M., (1995). Exciton Condensate in Semiconductor Quantum Well Structures. Phys. Rev. Lett. 74, 1633–1636.
Žutić, I., Fabian, J., Das Sarma, S., (2004). Spintronics: Fundamentals and applications. Rev. Mod. Phys. 76, 323–410.

Appendix A.
Strong correlations and Hubbard model

The Hubbard model, that is the simplest model of interacting particles, was developed by J. Hubbard in 1963 to describe the transition between conducting and insulating systems (Hubbard, (1963)).

The Hamiltonian is composed with a kinetic term allowing for tunneling (hopping) of particles between lattice sites and a potential term consisting of an on-site interaction

$$\mathcal{H} = -t \sum_{\langle i,j \rangle \sigma} \hat{c}_{i\sigma}^{\dagger} \hat{c}_{j\sigma} + U \sum_{i} \hat{n}_{i\uparrow} \hat{n}_{i\downarrow}$$

where t is the nearest-neighbor hopping amplitude, $< i , j >$ describe the summing over all nearest-neighbors, $\hat{n}_{i\sigma} = \hat{c}_{i\sigma}^{\dagger} \hat{c}_{i\sigma}$ is the particle density operator on site I and U is the Coulomb energy required for double occupancy of a site.

The Hubbard model explains why the undoped cuprates are insulating and antiferromagnetic. When nearest-neighbor spins are antiparallel, virtual hopping to the nearest-neighbor sites can lower the kinetic energy; this is not possible with parallel spins because of the Pauli exclusion principle.

The interaction term in the Hubbard Hamiltonian for cuprates results in the antibonding conduction band being split into the lower Hubbard band (LHB) and upper Hubbard band (UHB), with U energy gap separating them.

In the following years, Zaanan et al. described the band gaps and electronic structure of transition-metal compounds, such as cuprates. In these systems, the charge transfer energy Δ, describing the transfer of holes from Cu to O ligands, is smaller than the Hubbard splitting U, describing the

transfer of holes from Cu to Cu (Zaanen et al., (1985)). Consequently, in the undoped cuprates the insulating gap exists between the UHB and the so-known Zhang-Rice singlet band.

In Figure A-1, a schematic diagram of the density of states of cuprates is shown. In particular, Figure A-1 (a) describes the non-interacting case, where the bonding (B) and non-bonding (NB) bands are full and the anti-bonding (AB) band is half-filled, resulting in a metallic system. When Hubbard correlations are considered, the AB band is split into LHB and UHB, resulting in an insulating state (Figure A-1 (b)). In transition-metal compounds (as cuprates), the Hubbard splitting U is larger than the charge-transfer gap Δ (Figure A-1 (c)). Further hybridization causes the Zhang-Rice (ZRS) and triplet (T) bands to form (Harter, (2013)).

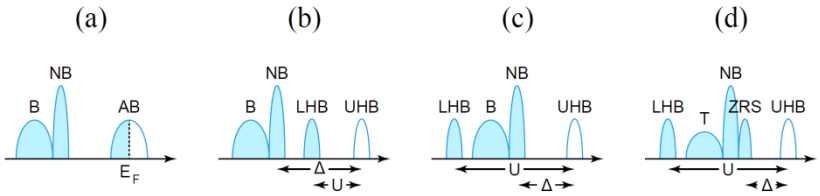

Figure A-1 *Schematic diagram of the density of states of the cuprates at increasing levels of details. (a) non-interacting case; (b) Hubbard correlations considered (insulating case); (c) in transition-metal compounds; (d) further hybridization (Harter, (2013))*

Appendix B.
Ginzburg-Landau approach for clean electronic systems

Eq. III-3 is equally applicable to ferromagnetic and superconductive phase transitions both described in terms of a generic order parameter $f(z)$, which is obtained from the slab free energy

$$F[f(z)] = S \int_{-t/2}^{t/2} dz[c(\partial_z f(z))^2 + af(z)^2 + bf(z)^4]$$

using the extremal condition $\delta F[f(z)] = 0$ of the variational calculus. Motivated by the slab geometry (defined by in-plane surface S and thickness t), we assume that the order parameter only depends on the z coordinate, being the system size finite along this direction. Translational invariance is assumed along the plane perpendicular to the z direction. The extremal condition jointly with the usual boundary conditions $\partial_z f(z)_{z=\pm t/2} = 0$ leads to the differential equation for the order parameter $\partial_z^2 f - \frac{a}{c} f = 0$, where the non-linear term proportional to f^3 has been omitted since it is negligible (compared to the linear term f) at the phase transition temperature T^*. The differential equation is solved by $f = A\, e^{i\mu z} + Be^{-i\mu z}$, with $\mu = \sqrt{\dot{a}\left(T_{C_0} - T^*\right)/c}$ a function of the temperature T^* with $T^* < T_{C_0}$. In deriving this result we assume, as usual within a Ginzburg-Landau theory, that the coefficients b>0 and c>0 are temperature independent, while $a = \dot{a}\left(T^* - T_{C_0}\right)$ is a temperature-dependent quantity. By applying the

boundary conditions to $f(z)$, we obtain a set of two homogeneous equations for the arbitrary constants A, B. A non-trivial solution is found by imposing that the determinant of the coefficients matrix is a vanishing quantity; this condition leads to the equation $sin(\mu t) = 0$, which admits solutions $\mu t = n\pi$, with $n \in N$. Since the coefficient μ is a function of temperature, the transition temperature of a system of finite thickness $T^* = T_C(t)$ is solution of the equation $\mu(T^*)t = n\pi$, where n have to be chosen to maximize the critical temperature $T^* < T_{C_0}$. Solving the equation for T^* and setting $n = 1$, we recover eq. III-3 with $L_0 = \pi\sqrt{c/(\dot{a}T_{C_0})}$. Therefore, the $T_C(t)$ vs t curves strongly depend on the boundary conditions imposed by the Ginzburg-Landau treatment to the order parameter $f(z)$ and thus the choice of adequate boundary conditions in describing a given physical system is a relevant problem.

Appendix C.
Evidence of WL in SLCO films by noise spectroscopy measurements

Electrical noise spectroscopy is a very sensitive and non-destructive technique, such as electric noise, has been used to analyze the samples, because it is capable to reveal a strict connection between WL effects and specific properties of the low-frequency *1/f* noise (Barone et al., (2016); P Orgiani et al., (2015)). In particular, a linear dependence of the voltage-spectral density S_V on the bias current (I) is observed in systems undergoing a WL transition (Barone et al., (2015), (2013), (2009)), while far from the weak localization region, the usual quadratic behavior of S_V vs I is found.

All of the AC measurements have been performed in a closed-cycle refrigerator, operating in the 8 to 325K range with a temperature stabilization better than 0.1K. A low-noise current source was used to bias the samples, while the output signal was amplified with a low-noise preamplifier and acquired with a dynamic signal analyzer in the 1 – 100'000 Hz frequency bandwidth. Spurious contributions, due to external contact noise, were removed by using a specific experimental procedure (Barone et al., (2007b)).

The frequency dependent of the voltage spectral density S_V for a representative under-doped SLCO sample, in which QIEs are expected to be strongest is shown in Figure C-1, where the whole investigated range between 10 and 300K is considered.

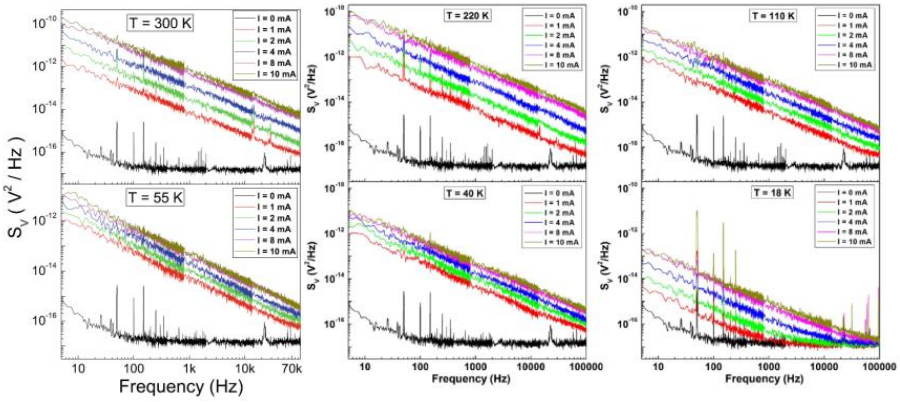

Figure C-1 *Low-frequency voltage spectral densities for an under-doped SLCO sample at two different temperatures and at different dc bias currents (i.e., up to 10 mA). The zero-bias background noise is shown as black trace.*

In Figure C-1, the chosen temperature where the noise measurements have been performed are related to the metallic region (T = 300K and T=220K), metal-insulator transition (T=110K), weak-localization (T = 55K and T = 40K) and superconducting (T = 18K).

A metal-to-insulator transition is observed at a crossover temperature T_{loc} around 110 K, while a superconducting onset occurs in the low-temperature limit at $T_C^{onset} \sim 25K$. In all of the regions, characterized by different electric transport mechanisms, the voltage noise has been measured as a function of the bias current and reproduced in terms of a simple parabolic functional of the following form:

$$S_V(90Hz) = a_2 I^2 + a_1 I + a_0 \qquad C\text{-}1$$

where *1/f* component has been evaluated at a reference frequency of 90Hz and a_2, a_1 and a_0 are temperature-dependent coefficients. The evolution of these fitting parameter is shown in Figure C-2 a), revealing that a predominant quadratic current dependence of *1/f* noise is evident in the metallic and superconducting transition regions, while the linear term a_1 arises in the intermediate region below T_{loc}, where the resistance upturn is observed.

The doubling of the dominant current power exponent η ($S_V \propto I^{\eta}$) from a value of 1 to 2 is more clearly visible in Figure C-2 b), where this change of two transition regions close to T_{loc} and T_C^{onset} also appears.

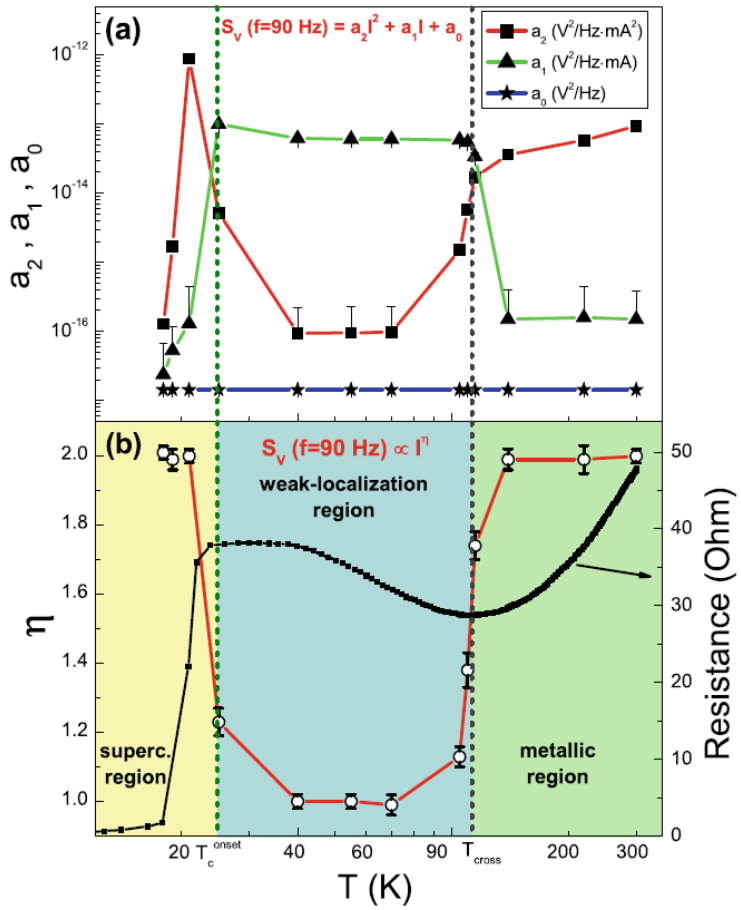

Figure C-2 *a) Temperature dependence of the three fitting parameters a_2,a_1, and a_0 appearing in eq. C-1; b) a clear sign of a crossover is evident at $T_{cross} \sim T_{loc} \sim 110$ K, where weak localization effects occur producing an upturn of the resistivity and a change of the current power exponent η of the 1 / f noise*

More details about these measurements can be find in (Barone et al., (2016)).